DETECTION OF AQUEOUS LEAD (II) AND MERCURY (II) USING MICRO-RING RESONATORS COATED WITH TETRASULFIDE FUNCTIONALIZED MESOPOROUS ORGANOSILICA THIN FILMS

by

Hao Chen

A thesis submitted to the Department of Chemistry

In conformity with the requirements for

the degree of Master of Science

Queen's University

Kingston, Ontario, Canada

March, 2017

Copyright © Hao Chen, 2017

Abstract

Silicon-on-insulator (SOI) micro-ring resonators coated with bis[3-(triethoxysilyl)propyl] tetrasulfide (TESPT) and tetraethoxysilane (TEOS) co-condensation mesoporous silica coatings are reported as chemical sensors to detect Pb(II) and Hg(II) ions in aqueous solutions. The sensors were based on the interaction of the evanescent field of the guided light with the functionalized mesoporous silica films. Upon adsorption of heavy metal ions (Pb(II) and Hg(II)), the refractive index of the film increased, leading to observable shifts in the resonant wavelengths of the micro-resonators. The tetrasulfide groups were placed into some of the silica films to increase the films' affinity to Pb(II) and Hg(II) ions.

The sensors were exposed to aqueous solutions of Pb(II) and Hg(II) ions at different concentrations and time-resolved adsorption-desorption curves were recorded and analyzed. It was found that two distinct binding sites with different affinities for metal ions were present in the S_4-TEOS silica films, corresponding to the tetrasulfide groups and the silanol groups. The rate constants for the absorption and desorption processes as well as the equilibrium constants were determined for each of the binding sites and ions. The initial adsorption rates of the Pb(II) and Hg(II) uptake processes changed linearly with Pb (II) and Hg(II) concentrations from 10 ppb to 1 ppm and could be used to quantify metal ions at the 30 ppb level.

The adsorption and desorption processes of other ions on the same tetra-sulfide film were reported to test for possible chemical interferences – specifically of Na(I), K(I), Mg(II), Ca(II), Fe(II), Zn(II), Cd(II), and Fe(III). In addition, Pb(II), Na(I), K(I), Ca(II), Fe(II), and Fe(III) solutions were tested on mesoporous silica films without the tetrasulfide groups to test their adsorption and desorption to bare silica. These test results fitted well with a single-adsorption-site model for TEOS silica film, which confirmed the double-adsorption-site model for the S_4-TEOS silica films, where the deprotonated silanol groups and the tetrasulfide groups acted as the two adsorption sites. A single-adsorption-site model was developed for the TEOS silica film, with the deprotonated silanol groups as the only adsorption sites. Tap water and seawater spiked with Pb(II) were also tested on S_4-TEOS silica films.

Acknowledgements

I want to thank my supervisor, Dr. Hans-Peter Loock, who gave me the opportunity to study and work under his supervision. You have always been an excellent supervisor and mentor to me. Your encouragement, patience, and helpful advice were essential for me to finish this research project.

I want to thank my supervisory committee members, Dr. Richard Oleschuk, Dr. Diane Beauchemin, and Dr. Gang Wu for their help and advice. You have both been very supportive in helping me on this project and my graduate studies.

I want to thank my coworkers who worked with me on this project, Dr. John Saunders, Dr. Sogol Borjian Borojeni, Dr. Xiaowei Wu, Connor Sanders, and Dr. Jack Barnes. Without your help and cooperation, this project could never have succeeded.

I want to thank my colleagues, Dr. John Saunders, Dr. Sogol Borjian Borojeni, Dr. Xiaowei Wu, Nicholas Andrews, Amy Maclean, Annica Freytag, Connor Sanders, Dr. Steve Walker, Jeff Crouse, Dr. Yoany Rodriguez for their kindness and support. You have always been up for a good time.

I want to thank all my collaborators, including Dr. Cathleen Crudden, ABB Canada Inc, and National Research Council Canada.

I want to thank all the administrative, research, and technical staff in the Department of Chemistry, who did an excellent job in supporting my study and research.

I want to thank my beloved families, my father Chen Hong, who supports me all along, and my mother Zhang Jirong, who is dearly missed and has always been blessing me from the heaven.

I want to give special thanks to my friend Miriam Bart, who has been a great friend throughout my time here.

I want to thank Queen's University, Natural Sciences and Engineering Research Council of Canada (NSERC), and ABB Canada Inc. for all the financial support for my study and research activities.

Table of Contents

Abstract ii
Acknowledgements iii
List of Figures vii
List of Tables xi
List of Abbreviations xiv
Chapter 1 Introduction 1
1.1 Waveguide Refractive Index Sensors 1
1.2 Refractive Index and Refractive Index Measurement 1
1.2.1 Refractive Index 1
1.3 Optical Waveguides, Modes, and Evanescent Wave 3
1.4 Fibre Grating Sensors 4
1.4.1 Straight and Tilted FBGs 5
1.4.2 Long-Period Gratings (LPGs) 7
1.5 Silicon-on-Insulator (SOI). 8
1.5.1 Waveguide Mach-Zehnder interferometers 10
1.5.2 SOI Ring Resonators 11
Chapter 2 Evanescent Wave Sensor Functionalization Methods 13
2.1 Bio-molecule Functionalization for Biosensors 14
2.1.1 Antibody Functionalization 14
2.1.2 Aptamers Functionalization 14
2.1.3 Other Molecules for Biosensor Functionalization 15
2.2 Polymer Functionalization 15
2.2.1 Molecularly Imprinted Polymer Functionalization 15
2.2.2 Siloxanes Functionalization for Volatile Organic Compound (VOC) Sensors 16
2.3 Porous Silica Functionalization 16
2.3.1 Functionalized Mesoporous Silica as Scrubbing Material for Phosphate and Nitrate ions. 18
2.3.2 Tetrasulfide-functionalized Mesoporous Silica Coatings on LPG Sensor 19
Chapter 3 Theory of Adsorption and Desorption, Models, and Equations 21
3.1 Adsorption Theory 21
3.1.1 The Langmuir Adsorption Theory 21
3.1.2 The Brunauer–Emmett–Teller (BET) Theory 22
3.1.3 The Temkin Theory 23

3.1.4 The Freundlich Theory 23
3.2 Models and Equations 23
3.2.1 Single Adsorption Site Model 23
3.2.2 Double Adsorption Site Model 25
3.2.3 Method of Initial Rates Calculation 27
3.3 Relationship Between Metal Loading in the Silica Film and Refractive Index 28
Chapter 4 Experimental Design, Setup, Data Collection, and Processing 33
4.1 Temperature Effects and Tandem Ring Resonators 33
4.2 Optical Experimental Setup and Methods 36
4.2.1 Coupling Laser Light into/out of the Waveguides 36
4.2.2 Optical Setup 37
4.2.3 Experimental Parameter Setting 39
4.2.4 Data Storing and Processing 40
4.3 Microfluidic Device and Liquid Sample Pumping System 41
4.4 Ring Resonators Calibration 42
4.5 Mesoporous Silica Coating 43
4.6 Water Flow Baseline Drift 44
Chapter 5 Sensing of Lead, Pb(II), and Mercury, Hg(II) 46
5.1 Pb(II) Ion Adsorption and Desorption Tests in DI Water 47
5.1.1 Adsorption and Desorption Tests on S_4-PMS Coating 47
5.1.2 Adsorption and Desorption Tests on PMS Coating 49
5.1.3 Test on Uncoated Chip 51
5.1.4 Adsorption and Desorption at Different Pb(II) Ion Concentrations 52
5.1.5 The Linear Relationship Between the Initial Adsorption Rates and the Pb(II) concentration 60
5.1.6 Determination of Rate Constants, Equilibrium Constants and Adsorption Capacities for Pb(II) ion adsorption 62
5.2 Pb(II) Ion Adsorption and Desorption in Tap Water 65
5.2.1 Adsorption Curve of Tap Water of the S_4-PMS Coating 66
5.2.2 Pb(II) Ion Adsorption and Desorption on the S_4-PMS Coating in Tap Water 67
5.3 Pb(II) Ion Adsorption in Seawater on S_4-PMS coating 69
5.4 Hg(II) Ion Adsorption and Desorption Tests in DI Water 70
5.4.1 Tests on the S_4-PMS Coating 70
5.4.2 Adsorption and Desorption at Different Hg(II) Concentrations 73
5.4.3 Initial adsorption rates have a linear relationship with the Hg(II) concentration. 80

5.4.4 Determination of Rate Constants, Equilibrium Constants and Adsorption capacities for Hg(II) ion 82
5.5 X-ray Photoelectron Spectroscopy (XPS) Measurement 85
5.5.1 XPS Measurement Conditions 85
5.5.2 XPS Measurement on S_4-PMS Film after Pb(II) Ion Absorption 85
Chapter 6 Adsorption and Desorption of Other Metal Ions 87
6.1 Na(I) Ion Adsorption and Desorption Tests 87
6.1.1 Na(I) Ion S_4-PMS Coating Tests 87
6.1.2 Na(I) Ion PMS Coating Tests 88
6.2 K(I) Ion Adsorption and Desorption Tests 89
6.2.1 K(I) Ion S_4-PMS Coating Tests 89
6.2.2 K(I) Ion PMS Coating Tests 90
6.3 Mg(II) Ion Adsorption and Desorption Tests 91
6.4 Ca(II) Ion Adsorption and Desorption Tests 92
6.4.1 Ca(II) Ion S_4-PMS Coating Tests 92
6.4.2 Ca(II) Ion PMS Coating Tests 93
6.5 Fe(II) Ion Adsorption and Desorption Tests 95
6.5.1 Fe(II) Ion S_4-PMS Coating Tests 95
6.5.2 Fe(II) Ion PMS Coating Tests 96
6.6 Zn(II) Ion Adsorption and Desorption Tests 97
6.7 Cd(II) Ion Adsorption and Desorption Tests 98
6.8 Fe(III) Ion Adsorption and Desorption Tests 100
6.8.1 Fe(III) Ion S_4-PMS Coating Tests 100
6.8.2 Fe(III) Ion PMS Coating Tests 101
6.9 Al(III) Ion Adsorption and Desorption Tests 102
6.10 Summary 104
Chapter 7 Conclusion 110
7.1 Summary 110
7.2 Future work 111
7.2.1 Coating Optimization 112
7.2.2 Data Processing Method 112
7.2.3 Optical Design 112
7.2.4 Testing Parameter Optimization 114
References 115

List of Figures

Figure 1-1 *Diagram showing refraction and reflection at a dielectric interface.* 2
Figure 1-2 *Diagram showing refraction and total internal reflection at a dielectric interface.* 2
Figure 1-3 *Diagrams showing evanescent field profile and cross-sections for typical waveguides.* 4
Figure 1-4 *The structures and modes coupling of FBGs and TFBGs.* 6
Figure 1-5 *Measured power transmission and reflection spectra for typical FBG and TFBG.* 7
Figure 1-6 *An LPG spectrum.* 8
Figure 1-7 *Optical microscope image of pair of tandem micro-ring resonators.* 9
Figure 1-9 *Optical microscope image of several SOI Mach-Zehnder Interferometers.* 11
Figure 1-10 *Optical microscope image of a 936 μm long spiral ring resonator on a SOI chip.* 12
Figure 1-11 *Resonance spectra of a 936 μm long spiral ring resonator.* 12
Figure 2-1 *Diagram showing general principle of molecular imprinting.* 16
Figure 2-2 *Scheme showing the condensation of TEOS and formation of silica network.* 17
Figure 2-3 *Schematic representation of typical micellar mesophases.* 18
Figure 2-4 *Diagram showing the formation of mesoporous silica via a lyotropic liquid crystalline pathway.* 18
Figure 2-5 *Structure of (3-Aminopropyl)triethoxysilane.* 19
Figure 2-6 *Synthesis of tetrasulfide- and Ti-containing mesoporous materials as coatings for LPG chemical sensors. [15]* 20
Figure 2-7 *Optical response for the LPG coated with the PMO film to aqueous DMSO solutions (RI = 1.402 at 1550 nm) of Pb(II) of increasing concentration as observed by the LPG attenuation spectra.* 20
Figure 3-1 *Langmuir isotherm for non-dissociative adsorption for different K values.* 22
Figure 3-2 *BET isotherm at different values of c.* 23
Figure 3-3 *Refractive index of porous silica film with water filling its pores as a function of the mole fraction of water.* 29
Figure 3-4 *Porous silica refractive index as a function of Pb(II) and Hg(II) mole fraction at different porosity (x_{water} = 0.3, 0.4, 0.5).* 31
Figure 3-5 *Pb doping response on porous silica film as a function of porosity.* 31
Figure 4-1 *Optical profilometer image and a transmission spectrum of a tandem ring resonator.* 33
Figure 4-2 *Compensation of temperature effects from the resonance shifts of the reference ring of a tandem ring resonator.* 35
Figure 4-3 *The top blue dots indicate the temperature data measured by the USB temperature probe.* 35

Figure 4-4 *Schematic of coupling methods to get light into photonic waveguides.* 37
Figure 4-5 *Photo of the alignment stages with the fibers, microfluidics, tubes, and Photodiode detector.* 37
Figure 4-6 *Schematic of the experimental setup for SOI chip testing.* 38
Figure 4-7 *Sample voltage ramp from the Ando laser in the continuous wavelength scan mode.* 39
Figure 4-8 *Comparison of the spectral resolution as a function of laser scan rate over a fixed spectral window.* 40
Figure 4-9 *A tandem ring spectrum and a Lorentzian function fit on the sensing peak.* 41
Figure 4-10 *The microfluidic device with the chip and the optical alignment.* 42
Figure 4-11 *Tandem ring resonator calibration.* 43
Figure 4-12 *Temperature-corrected sensing peak baselines at 0.9 ml/min and 0 ml/min flow rate of DI water.* 45
Figure 5-1 *Comparison between single and double exponential functions fits of 1 ppm Pb(II) ion DI water solution adsorption and desorption on the S_4-PMS coating.* 48
Figure 5-2 *Single exponential function fit to the 1 ppm Pb(II) adsorption and desorption processes of the PMS coating* 50
Figure 5-3 *Uncoated chip shows no refractive index change between water and Pb(II) solution.* 51
Figure 5-4 *Adsorption-desorption curve when the resonators were exposed to a series of Pb(II) solutions with concentrations of 1000 ppb, 500 ppb, 300 ppb, 200 ppb, 100 ppb, 50 ppb, 20 ppb, and 10 ppb.* 52
Figure 5-5 *Double exponential function fits of 1 ppm Pb(II) ion adsorption and desorption processes on the S_4-PMS coating, with fit residual shown below.* 53
Figure 5-6 *Double exponential function fits of 500 ppb Pb(II) ion adsorption and desorption processes on the S_4-PMS coating, with fit residual shown below.* 54
Figure 5-7 *Double exponential function fits of 300 ppb Pb(II) ion adsorption and desorption processes on the S_4-PMS coating, with fit residual shown below.* 55
Figure 5-8 *Double exponential function fits of 200 ppb Pb(II) ion adsorption and desorption processes on the S_4-PMS coating, with fit residual shown below.* 56
Figure 5-9 *Single exponential function fits of 100 ppb Pb(II) ion adsorption and desorption processes on the S_4-PMS coating, with fit residual shown below.* 57
Figure 5-10 *Single exponential function fits of 50 ppb Pb(II) ion adsorption and desorption processes on the S_4-PMS coating, with fit residual shown below.* 58
Figure 5-11 *Single exponential function fits of 20 ppb Pb(II) ion adsorption and desorption processes on the S_4-PMS coating, with fit residual shown below.* 59
Figure 5-12 *Single exponential function fits of 10 ppb Pb(II) ion adsorption and desorption processes on the S_4-PMS coating, with fit residual shown below.* 60

Figure 5-13 *Initial refractive index change rate at different concentrations of Pb(II) ion.* 62
Figure 5-14 *Diagram showing $1/\tau_{a,X}$ has a linear relationship with Pb(II) concentration.* 64
Figure 5-15 *$[Pb(II)]/[Pb(II)X]_{eq,a}$ showing a linear relationship with Pb(II) concentration.* 65
Figure 5-16 *Tap water adsorption curve of S_4-PMS coating.* 66
Figure 5-17 *Tap water baseline of S4-PMS coating.* 67
Figure 5-18 *Comparison between single and double exponential functions fits of 1ppm Pb(II) ion tap water solution adsorption and desorption on the S_4-PMS coating.* 68
Figure 5-19 *S_4-PMS coating refractive index change when alternating between DI water and seawater flow.* 69
Figure 5-20 *Seawater spiked with 1ppm Pb(II) adsorption and desorption test on S_4-PMS coated ring resonator.* 70
Figure 5-21 *Comparison between single and double exponential functions fits of 1 ppm Hg(II) ion DI water solution adsorption and desorption on the S_4-PMS coating.* 71
Figure 5-22 *The adsorption curve curves when the resonators were exposed to a series of Hg(II) solutions at 1000 ppb, 500 ppb, 300 ppb, 200 ppb, 100 ppb, 50 ppb, 20 ppb.* 73
Figure 5-23 *Single exponential function fit of 1ppm Hg(II) ion 40 minutes adsorption process on the S_4-PMS coating, with fit residual shown below.* 74
Figure 5-24 *Single exponential function fit of 500 ppb Hg(II) ion 40 minutes adsorption process on the S_4-PMS coating, with fit residual shown below.* 75
Figure 5-25 *Single exponential function fit of 300 ppb Hg(II) ion 40 minutes adsorption process on the S_4-PMS coating, with fit residual shown below.* 76
Figure 5-26 *Single exponential function fit of 200 ppb Hg(II) ion 40 minutes adsorption process on the S_4-PMS coating, with fit residual shown below.* 77
Figure 5-27 *Comparison between single exponential functions and linear fits of 100 ppb Hg(II) ion adsorption and desorption on the S_4-PMS coating.* 78
Figure 5-28 *Comparison between single exponential functions and linear fits of 50 ppb Hg(II) ion adsorption and desorption on the S_4-PMS coating.* 79
Figure 5-29 *Comparison between single exponential functions and linear fits of 20 ppb Hg(II) ion adsorption and desorption on the S_4-PMS coating.* 80
Figure 5-30 *Initial refractive index change rate at different concentrations of Hg(II) ion.* 81
Figure 5-31 *By fitting $1/\tau_{a,X}$ vs. Hg(II) concentration, $k_{a,X}$, $k_{d,X}$, and $K_{a,X}$ for Hg(II) ion adsorption on the S_4-PMS coating can be calculated.* 83
Figure 5-32 *By fitting $[Hg(II)]/[Hg(II)X]_{eq,a}$ vs. $[Hg(II)]$ with a linear function, $K_{a,X}$ and $[X]_0$ for Hg(II) ion adsorption on the S_4-PMS coating can be calculated.* 83

Figure 5-33 *XPS spectra of adsorbed heavy metals.* 86
Figure 6-1 *Single exponential function fit of Na(I) ion adsorption and desorption processes on the S_4-PMS coating* 88
Figure 6-2 *Single exponential function fit of Na(I) ion adsorption and desorption processes on the TOESMPS coating* 89
Figure 6-3 *Single exponential function fit of K(I) ion adsorption and desorption processes on the S_4-PMS coating* 90
Figure 6-4 *Single exponential function fit of K(I) ion adsorption and desorption processes on the TOESMPS coating* 91
Figure 6-5 *Single exponential function fit of Mg(II) ion adsorption and desorption processes on the S_4-PMS coating* 92
Figure 6-6 *Single exponential function fit of Ca(II) ion adsorption and desorption processes on the S_4-PMS coating* 93
Figure 6-7 *Single exponential function fit of Ca(II) ion adsorption and desorption processes on the PMS coating* 94
Figure 6-8 *Comparison between single and double exponential functions fits of Fe(II) ion adsorption and desorption on the S_4-PMS coating.* 95
Figure 6-9 *Single exponential function fit of Fe(II) ion adsorption and desorption processes on the TOESMPS coating* 96
Figure 6-10 *Comparison between single and double exponential functions fits of Zn(II) ion adsorption and desorption on the S_4-PMS coating.* 97
Figure 6-11 *Comparison between single and double exponential functions fits of Cd(II) ion adsorption and desorption on the S_4-PMS coating.* 99
Figure 6-12 *Comparison between single and double exponential functions fits of Fe(III) ion adsorption and desorption on the S_4-PMS coating.* 100
Figure 6-13 *Single exponential function fit of Fe(II) ion adsorption and desorption processes on the TOESMPS coating* 102
Figure 6-14 *Comparison between single and double exponential functions fits of Al(III) ion adsorption and desorption on the S_4-PMS coating.* 103
Figure 6-15 *Column graphs comparison between different ion adsorption on S_4-PMS film.* 107
Figure 6-16 *Column graphs comparison between different ion adsorptions on PMS film.* 109
Figure 7-1 *An example of Stratophase micro optical sensor packaging.* 113

List of Tables

Table 2-1 Commercial optical waveguide chemical- and bio- sensors.....13
Table 3-1 Pb(II) and Hg(II) doping response to the MPS film(wet and dry).....30
Table 5-1 Fitting parameters for single exponential functions (5.1) and (5.3), and double exponential equations (5.2) and (5.4) to describe the Pb(II) ion adsorption and desorption on the S_4-PMS coating of Figure 5-1.....49
Table 5-2 Fitting parameters for single exponential functions (5.1) and (5.3) to describe the Pb(II) ion adsorption and desorption on the PMS coating of the figure above. 50
Table 5-3 Fitting parameters for double exponential function (5.2) and (5.4) fits of the 1 ppm Pb(II) ion adsorption and desorption on the S_4-PMS coating of the figure above. 53
Table 5-4 Fitting parameters for double exponential function (5.2) and (5.4) fits of the 500 ppb Pb(II) ion adsorption and desorption on the S_4-PMS coating of the figure above. 54
Table 5-5 Fitting parameters for double exponential function (5.2) and (5.4) fits of the 300 ppb Pb(II) ion adsorption and desorption on the S_4-PMS coating of the figure above. 55
Table 5-6 Fitting parameters for double exponential function (5.2) and (5.4) fits of the 200 ppb Pb(II) ion adsorption and desorption on the S_4-PMS coating of the figure above. 56
Table 5-7 Fitting parameters for single exponential function (5.1) and (5.3) fits of the 100 ppb Pb(II) ion adsorption and desorption on the S_4-PMS coating of the figure above. 57
Table 5-8 Fitting parameters for single exponential function (5.1) and (5.3) fits of the 50 ppb Pb(II) ion adsorption and desorption on the S_4-PMS coating of the figure above. 58
Table 5-9 Fitting parameters for single exponential function (5.1) and (5.3) fits of the 20 ppb Pb(II) ion adsorption and desorption on the S_4-PMS coating of the figure above. 59
Table 5-10 Fitting parameters for single exponential function (5.1) and (5.3) fits of the 10 ppb Pb(II) ion adsorption and desorption on the S_4-PMS coating of the figure above. 60
Table 5-11 Initial Adsorption rate of Pb(II) solutions at different concentrations.....61
Table 5-12 Pb(II) Desorption data sets for $k_{d,X}$ calculation.....63
Table 5-13 Pb(II) data sets for $k_{a,X}$, $k_{d,X}$, $K_{a,X}$, *and* $[X]_0$ calculation.....64
Table 5-14 Ion concentrations in Kingston tap water. 66
Table 5-15 Fitting parameters for single and double exponential function fits of Pb(II) tap water solution adsorption and desorption of S_4-PMS coating. 68

Table 5-16 Fitting parameters for single exponential functions (5.1) and (5.3), and double exponential equations (5.2) and (5.4) to describe the Hg(II) ion adsorption and desorption on the S_4-PMS coating of Figure 5-21. 72
Table 5-17 Fitting parameters for single exponential function (5.1) and (5.3) fits of the 1 ppm Hg(II) ion adsorption and desorption on the S_4-PMS coating of the figure above. 74
Table 5-18 Fitting parameters for single exponential function (5.1) and (5.3) fits of the 500 ppb Hg(II) ion adsorption and desorption on the S_4-PMS coating of the figure above. 75
Table 5-19 Fitting parameters for single exponential function (5.1) and (5.3) fits of the 300 ppb Hg(II) ion adsorption and desorption on the S_4-PMS coating of the figure above. 76
Table 5-20 Fitting parameters for single exponential function (5.1) and (5.3) fits of the 200 ppb Hg(II) ion adsorption and desorption on the S_4-PMS coating of the figure above. 77
Table 5-21 Fitting parameters for single exponential function (5.1) and (5.3) fits and linear fit of the 100 ppb Hg(II) ion adsorption and desorption on the S_4-PMS coating of the figure above. 78
Table 5-22 Fitting parameters for single exponential function (5.1) and (5.3) fits and linear fit of the 50 ppb Hg(II) ion adsorption and desorption on the S_4-PMS coating of the figure above. 79
Table 5-23 Fitting parameters for single exponential function (5.1) and (5.3) fits and linear fit of the 20 ppb Hg(II) ion adsorption and desorption on the S_4-PMS coating of the figure above. 80
Table 5-24 Initial Adsorption rates at different concentration of Hg(II) solutions. 81
Table 5-25 Hg(II) adsorption data sets for $k_{a,X}$, $k_{d,X}$, $K_{a,X}$, *and* $[X]_0$ calculation 82
Table 5-27 Element ratio calculated from XPS data 86
Table 6-1 Fitting parameters for single exponential function fit on 43.48 μmol/L (1 ppm) $NaNO_3$ DI water adsorption and desorption processes on S_4-PMS coating. 88
Table 6-2 Fitting parameters for single exponential function fit on 4.826 μmol/L $NaNO_3$ DI water adsorption and desorption processes on PMS coating 89
Table 6-3 Fitting parameters for single exponential function fit on 25.58 μmol/L (1 ppm) KNO_3 DI water adsorption and desorption processes on S_4-PMS coating. 90
Table 6-4 Fitting parameters for single exponential function fit on 4.826 μmol/L KNO_3 DI water adsorption and desorption processes on PMS coating 91
Table 6-5 Fitting parameters for single exponential function fit on 41.15 μmol/L (1ppm) $Mg(NO_3)_2$ DI water adsorption and desorption processes on S_4-PMS coating. 92
Table 6-6 Fitting parameters for single exponential function fit on 25.00 μmol/L (1ppm)$Ca(NO_3)_2$ DI water adsorption and desorption processes on S_4-PMS coating. 93
Table 6-7 Fitting parameters for single exponential function fit on 4.826 μmol/L $Ca(NO_3)_2$ DI water adsorption and desorption processes on PMS coating 94

Table 6-8 Fitting parameters for single and double exponential functions fits of 17.86 μmol/L (1 ppm) Fe(II) ion adsorption and desorption on the S_4-PMS coating. 95
Table 6-9 Fitting parameters for single exponential function fit on 4.826 μmol/L $Fe(NO_3)_2$ DI water adsorption and desorption processes on PMS coating 96
Table 6-10 Fitting parameters for single and double exponential functions fits of 15.29 μmol/L (1ppm) Zn(II) ion adsorption and desorption on the S_4-PMS coating. 98
Table 6-11 Fitting parameters for single and double exponential functions fits of 8.900 μmol/L (1ppm) Cd(II) ion adsorption and desorption on the S_4-PMS coating. 99
Table 6-12 Fitting parameters for single and double exponential functions fits of 17.90 μmol/L (1ppm) Fe(III) ion adsorption and desorption on the S_4-PMS coating. 101
Table 6-13 Fitting parameters for single exponential function fit on 4.826 μmol/L $Fe(NO_3)_3$ DI water adsorption and desorption processes on PMS coating 102
Table 6-14 Fitting parameters for single and double exponential functions fits of 37.04 μmol/L (1ppm) Al(III) ion adsorption and desorption on the S_4-PMS coating. 104
Table 6-15 Different ion binding patterns with PMS coating and S_4-PMS coating.[54] 105
Table 6-16 Cation and oxide polarizability for some ions [44, 47] 105
Table 6-17 Data sets for column graphs comparison between different ion adsorption on S_4-PMS film(above). 108
Table 6-18 Data sets for column graphs comparison between different ion adsorption on PMS film(Figure 6-16). 109

List of Abbreviations

FBG - fibre Bragg grating

TFBG - tilted fibre Bragg grating

LPG - long-period grating

FM - forward mode

HOCM - higher-order cladding mode

SRI - surrounding refractive index

SOI - silicon on insulator

FSR - free spectral range

MZI - Mach-Zehnder Interferometer

TM - transverse magnetic

TE - transverse electric

SELEX - systematic evolution of ligands by exponential enrichment

DNA - deoxyribonucleic acid

RNA - ribonucleic acid

MIP - molecularly imprinted polymer

SPR - surface plasmon resonance

TNT - 2,4,6-trinitrotoluene

PDMS - poly(dimethylsiloxane)

VOC - volatile organic compound

TMOS - tetramethoxysilane ($Si(OMe)_4$)

TEOS - tetraethoxysilane ($Si(OEt)_4$)

BTESPTS - bis[3-(triethoxysilyl)propyl]tetrasulfide

PMO - periodic mesoporous organosilica

PMS – periodic mesoporous silica

S_4-PMS - tetrasulfide mesoporous silica

EPA - environmental protection agency

ppb - part per billion

ppm - part per million

DI Water - deionized water

EDTA - ethylenediaminetetraacetic acid

FWHM - full width at half maximum

Chapter 1

Introduction

This chapter provides an overview of several different designs of refractive index sensors and their operating principles.

1.1 Waveguide Refractive Index Sensors

Optical waveguide refractive index sensors have attracted research interests for decades. Several different chemical and bio-sensors were developed for applications in manufacturing, agriculture, environmental protection, health service, homeland security, etc. Many of these sensors enjoy advantages over conventional (e.g. electrical or colorimetric) sensors, such as higher sensitivity, large detection range, small size, environmental robustness, and immunity against electromagnetic interference. A large class of these sensors measures the refractive index change when interacting with chemical and biological analytes in the attempt to identify and quantify these analytes.

The rest of the chapter briefly explains some of the most popular waveguide-based index sensors, including Fibre Bragg gratings (FBG), long-period gratings (LPG), and micro-resonators.

1.2 Refractive Index and Refractive Index Measurement

1.2.1 Refractive Index

In vacuum, the speed of light is $c_0 = 1/\sqrt{\varepsilon_0 \times \mu_0}$, where ε_0 is vacuum permittivity, and μ_0 is vacuum permeability. The refractive index of a certain medium is defined as the ratio between the speed of light in the medium and the speed of light in vacuum.

$$n = \frac{c_0}{c} \tag{1.1}$$

As the speed of light cannot be faster than that in vacuum, the refractive index is always larger than 1 in any medium other than vacuum.

In a homogeneous, isotropic material, light propagates in a straight line. When light travels from one medium into another medium with different refractive indices, diffraction and reflection occur at the interface. This behaviour is governed by Maxwell equations.

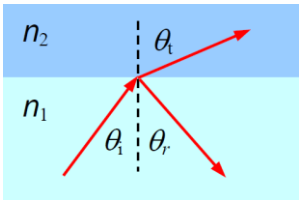

Figure 1-1 *Diagram showing refraction and reflection at a dielectric interface. When light travels from one medium into another medium with different refractive indices (in this case, $n_1 > n_2$, diffraction and reflection occur at the interface.) [1]*

As shown in Figure 1-1, Θ_i is the incident angle, Θ_r is the reflection angle, and Θ_t is the transmission angle. The incident angle and reflection angle share the same value. The transmission angle can be calculated by Snell's law, as shown in equation (1.2).

$$\begin{aligned} \theta_i &= \theta_r \\ n_1 \sin\theta_i &= n_2 \sin\theta_t \end{aligned} \tag{1.2}$$

When light travels from a high refractive index medium into a low refractive index medium, all light is reflected when the incident angle is equal or larger than the critical angle Θ_c. This phenomenon is called total internal reflection (TIR), as shown in Figure 1-2.

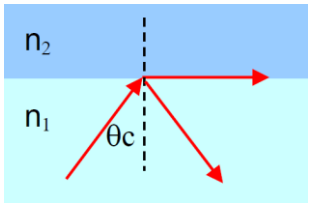

Figure 1-2 *Diagram showing refraction and total internal reflection at a dielectric interface. When the incident angle is equal or larger than the critical angle Θ_c, all light is reflected, and no transmission occurs. [1]*

1.3 Optical Waveguides, Modes, and Evanescent Wave

Optical waveguides are dielectric media that can confine and guide electromagnetic waves. A waveguide such as an optical fibre has a high refractive index core surrounded by low refractive index cladding. Because of total internal reflection at the core-cladding interface, light traveling along the core remains confined in the core. The two most common basic waveguide setups are planar waveguides and optical fibres, with their structures shown in Figure 1-3.[2]

Waveguides can be divided into single mode and multi-mode waveguides, based on the number of modes guided by the waveguides. A mode, or eigenmode, is a light wave that reproduces itself after two reflections in a waveguide. A single-mode waveguide has a thin core that can only guide one light mode. A multi-mode waveguide has a thick core that can guide more than one light mode.[2]

The part of the mode fields that extends out of the waveguide cores is called the evanescent wave. Figure 1-3 shows a field distribution of the lowest transverse-electric (TE) mode (mode number, $m = 0$) which has a Gaussian shape. The distribution tail with a penetration depth Δz is an evanescent wave. Evanescent waves are strongest at the core-cladding interfaces and decay fast as they penetrate the claddings. Because the evanescent fields are outside of the cores, they can interact with the surrounding mediums, and therefore have drawn interest from scientists to develop evanescent field sensing techniques.[2]

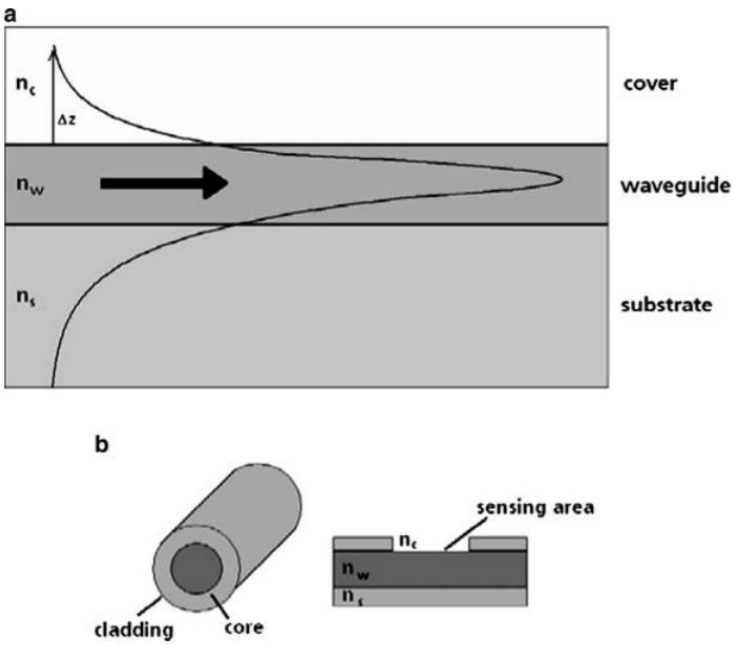

Figure 1-3 *Diagrams showing evanescent field profile and cross-sections for typical waveguides. (a) A planar waveguide with a core (refractive index n_w) sandwiched between a substrate (refractive index n_s) and a cover (refractive index n_c). The evanescent field (penetration depth Δz) of a guided light mode extends into the cover. (b-left) The cross-section of an optical fibre. (b-right) Sensing area can be made by removing part of the cover (cladding). The same conditions apply as to optical fibre and planar waveguides. [2]*

1.4 Fibre Grating Sensors

In a fibre grating sensor, the core of a germanium-doped single-mode optical fibre is prepared to have high and low index alternations along the direction of its fibre core axis. Based on the length of the period Λ, these fibre gratings can be subdivided into two distinct categories: short-period gratings, known as fibre Bragg gratings (FBGs) and long-period gratings (LPGs).[2]

While most of the fibre-grating-sensor research and applications have been in the field of strain- and temperature-sensing, the development of etched regular FBGs, tilted FBGs, and LPGs, and their sensitivities to the changes in the surrounding refractive indices (SRIs) have opened unprecedented opportunities for the development of fibre-optic refractometers.[2]

1.4.1 Straight and Tilted FBGs

In an FBG, the periodicity is uniform along the axis, and the period is usually on the order of half a micron [2]. For a given grating structure with a period Λ and a refractive index modulation Δn, waves reflected at each interface interfere with one another and are observed only for a particular resonance wavelength λ_B, which is called the Bragg wavelength. In addition, forward propagating core modes may couple with backward propagating higher-order cladding modes (HOCMs), generating cladding mode resonances. The structures and modes coupling within straight and tilted FBGs are shown in Figure 1-4. In a normal FBG, the Bragg peak is strong while the cladding mode resonances are weak. In a tilted FBG, the Bragg peak is weak while the cladding mode resonances are strong, as shown in Figure 1-5.[2]

For an FBG, the central Bragg wavelength λ_B is given as:

$$\lambda_B = 2n_e\Lambda \tag{1.3}$$

where n_e is the effective refractive index of the core, and Λ is the grating period. Numerous studies have demonstrated the use of FBGs as chemical sensors. Since light guided in the cores of the fibres does not interact with chemicals in the environment of the fibres, all these sensors require special coatings on the fibre waveguide. The coatings expand or shrink upon exposure with respective chemicals, thereby exerting strain on the FBG fibre, hence changing Bragg peak positions. In 1999, Spirin *et al.* reported a petroleum hydrocarbon leak sensor with a polymer coating.[3] In 2002, Cong *et al.* reported a salinity sensor with a hydrogel coating.[4] In 2005, Yeo *et al.* reported a humidity sensor with a moisture sensitive polymer coating. [5] In 1999, Sutapun *et al.* reported an FBG hydrogen sensor with a palladium coating, which expanded when the coating absorbed hydrogen. [6]

For a TFBG, the central Bragg wavelength λ_B is also governed by the equation (1.3), except Λ is replaced by the effective grating period Λ_g:

$$\lambda_B = 2n_e\Lambda_g \tag{1.4}$$

where $\Lambda_g = \Lambda / \cos\theta$ and θ is the tilt angle. The resonance wavelength λ_i of the *i*-th cladding mode is governed by

$$\lambda_i = (n_{e,i} + n_i)\Lambda \tag{1.5}$$

where $n_{e,i}$ is the effective refractive index of the core mode at λ_i, and n_i is the effective refractive index of the cladding.[2]

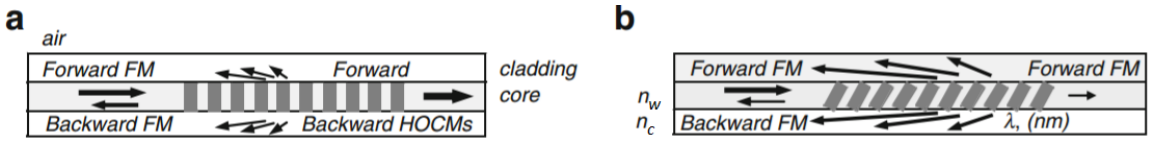

Figure 1-4 *The structures and modes coupling of FBGs and TFBGs. In an FBG, the forward FM is coupled to backward FM and HOCMs (a) a regular BFG with strong coupling to a backward FM and weak coupling to a multitude of HOCMs; (b) a tilted FBG with weak coupling to a backward FM and a strong coupling to a multitude of HOCMs.[2]*

TFBG cladding resonances peaks shift when surrounding refractive indices change. The changes can be enhanced by etching or by coating the TFBGs with gold or silver layers. TFBG chemical sensors have also been reported. In 2005, Chen *et al* reported a TFBG sugar sensor. [7] In 2009, Miao *et al* reported a relative humidity sensor based on tilted fibre Bragg grating with polyvinyl alcohol coating. [8] In 2014, L épinay *et al* reported a molecularly imprinted polymer (MIP) coated TFBG sensor for maltol. [9]

Both FBGs and TFBGs resonance spectra are sensitive to strain and temperature. As a result, internal or external references are needed to eliminate those unwanted effects for chemical- or bio-sensing.

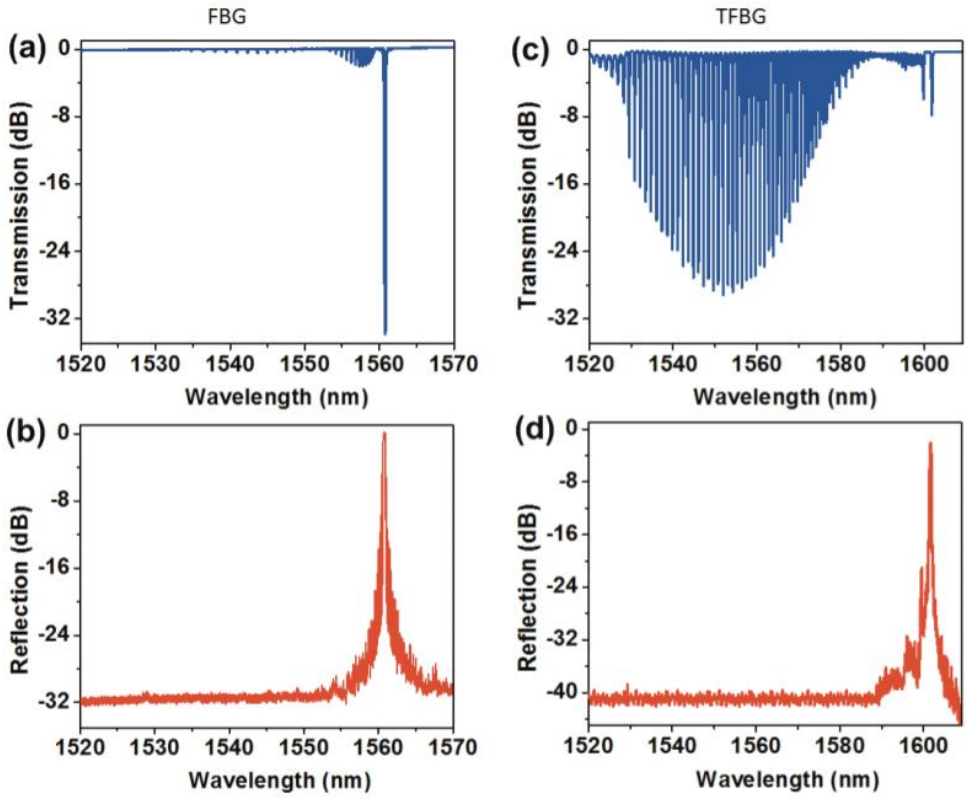

Figure 1-5 *Measured power transmission and reflection spectra for typical FBG and TFBG. (a) an FBG transmission spectrum. (b) an FBG reflection spectrum. (c) a TFBG transmission spectrum. (d) a TFBG reflection spectrum. [10]*

1.4.2 Long-Period Gratings (LPGs)

An LPG has a similar design as an FBG but with a period that is longer by about two orders of magnitude, usually several hundred micrometers. For an LPG, $\lambda_{m,LPG}$ is a separate resonance wavelength corresponding to each HOCM. The higher the mode order *m*, the greater the resonance wavelength $\lambda_{m,LPG}$, as shown in Figure 1-6. [2]

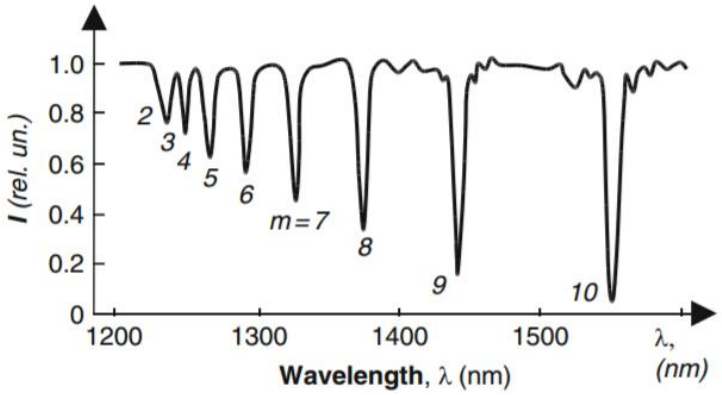

Figure 1-6 *An LPG spectrum. Notice that the higher the mode order, the greater the resonance wavelength. [2]*

Researchers have developed a variety of LPG sensors by replacing the cladding with chemically or biologically sensitive coatings and measuring the refractive index changes of the coatings upon contacting with analytes. DeLisa *et al* (2000) reported an immunosensor by immobilizing a layer of antibody (anti-human IgG) on an LPG fibre surface. [11] Falciai *et al* (2001) used LPGs as concentration sensors for sodium chloride and calcium chloride aqueous solutions by measuring the solution refractive indices. [12] Zhang *et al.* (2009) reported a trace chemical sensor by coating LPG fibres with zeolite thin films. [13] Tripathi *et al.* (2012) reported an E-coli bacteria sensor by immobilizing bacteriophage T4 on LPG fibre surface. [14] Du *et al.* (2010) reported a heavy-metal sensor by coating LPG fibre surface with a tetrasulfide-functionalized mesoporous organosilica film. [15]

However, as the LPGs resonance spectrums are also sensitive to strain and temperature, internal or external references are needed to eliminate those unwanted effects. In addition, the sensitivity of the LPG response depends strongly on the refractive index of the coating and is highly nonlinear. This makes the production of a robust and reliable sensor complicated. [15]

1.5 Silicon-on-Insulator (SOI).

As opposed to all waveguide sensors described above, the Silicon-on-insulator (SOI) waveguides are not based on optical waveguide fibre but based on planar waveguide. The SOI waveguides consist of silicon cores with either silica or polymer claddings. At the wavelength of 1550 nm, silicon refractive index

is 3.47, while the silica cladding refractive index is around 1.44. As the core and the core-cladding refractive index contrast is this high, the waveguide cross section can be as small as 0.2 μm. Also, the bend radius can be as small as a few microns, whereas optical fibre bend radii are typically at least 10-20 mm. As a result, the SOI waveguides can be made into nanowires on micro silicon chips to construct ultra-compact, complex optical circuits with high device density.[16] A pair of tandem micro-ring resonators is shown in Figure 1-7 as an example.

The small SOI waveguides have stronger evanescent fields than normal waveguides, as shown in Figure 1-8. In regular waveguides, the evanescent fields only consist of a small fraction of the total propagation fields – even for cladding modes the evanescent field is typically around 1-5%. In SOI waveguides, however, the waveguide cores are so small that they cannot effectively confine the modes. The modes field extend outside the core, and the evanescent fields can interact with the environment. In the case of a silicon nanowire that is less than 300 nm high and 400 nm wide, most of the guided transverse magnetic (TM) mode volume is outside the waveguide core. The evanescent wave of this mode can interact with the medium in the evanescent field, be it gas, liquid, polymer or any other material that covers the waveguide. It has been shown that the interaction is stronger than a free space beam interaction through the gas, liquid, or cladding material directly. This strong interaction is the reason for the very high sensitivity of evanescent field SOI waveguide sensors. [16]

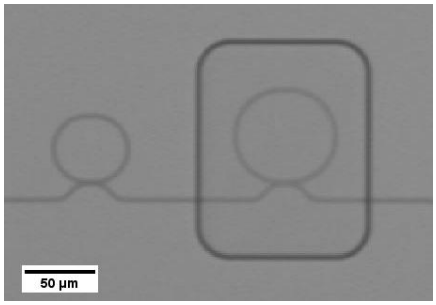

Figure 1-7 *Optical microscope image of pair of tandem micro-ring resonators.*

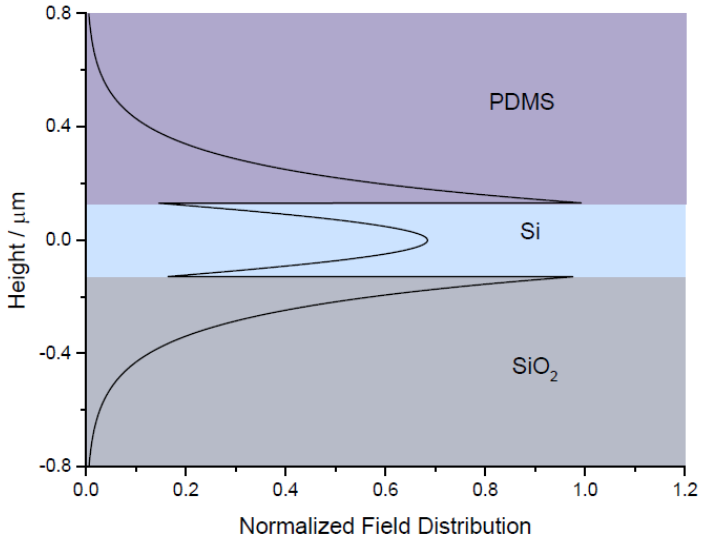

Figure 1-8 *Evanescent field profile for a typical silicon-on-insulator waveguide. [17]*

Many researchers have functionalized SOI waveguides to fabricate chemical sensors, by using micro-extraction films, polymers, antibodies, and porous silica film as the cladding materials.[18] In these applications, analytes are adsorbed into the cladding or attach to the antibodies on the waveguide surfaces. As a consequence, the cladding's refractive index changes influence the propagated modes through their interaction with the evanescent fields and cause optical phase shifts. These phase shifts can be measured by using either Mach-Zehnder interferometers or micro-ring resonators.

1.5.1 Waveguide Mach-Zehnder interferometers

In a Mach-Zehnder Interferometers (MZI), light from a bus waveguide is split into two optical paths and then recombined, producing a two-beam interference pattern. One optical path serves as a reference arm, and the other one acts as a sensing arm. The intensity of the interference patterns I is governed by

$$I = \frac{I_0}{2}\left[1+\cos\left(\frac{2\pi}{\lambda}(n_{e,sen}L_{sen} - n_{e,ref}L_{ref})\right)\right] \tag{1.6}$$

Here, I_0 is the original light intensity, $n_{e,sen}$ and $n_{e,ref}$ are the effective refractive indices of the sensing and reference arm and L_{sen} and L_{ref} are the length of the respective interferometer arms.

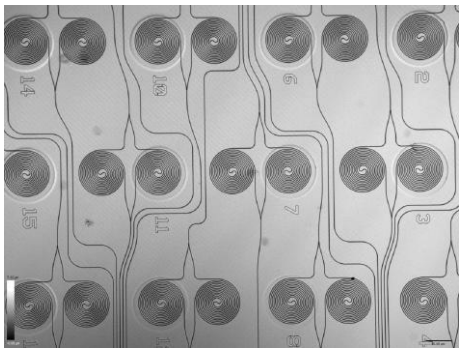

Figure 1-9 *Optical microscope image of several SOI Mach-Zehnder Interferometers. One waveguide arm is open and the other is covered with a layer of silica. [17]*

Mach-Zehnder interferometers constructed with silicon nanowires on silicon-on-insulator (SOI) chips are shown in Figure 1-9.[17] In our case of such a "balanced MZI", the reference arm is buried under a protective layer of SiO_2, while the sensing arm is open to sense surrounding refractive index change. The sensing arm can be coated with a thin film, which can adsorb analytes and thereby changes its refractive index. This index change affects the index contrast Δn and therefore changes the interference pattern. As a result, the MZI have great potential to make chemical sensors. [17]

1.5.2 SOI Ring Resonators

In a SOI ring resonator, a closed-loop waveguide ring is placed closely adjacent to an optical bus waveguide. [18] An optical profiler image of a 936 μm long spiral ring resonator on a SOI chip is shown in Figure 1-10. The light that travels through the bus waveguide couples strongly into the ring at certain wavelengths. These wavelengths, called resonance wavelengths, correspond to integer fractions of the circumference of the ring. The relationship between resonance mode order (m), resonance wavelength, effective refractive index (n_e), and ring circumference (L) is shown in the equation(1.7). [17]

$$m\lambda_r = n_e L \tag{1.7}$$

At the resonance wavelengths, light is coupled into the ring, and its energy is eventually dissipated, causing dips (resonance peaks) in the transmission spectra of the bus waveguide. The wavelengths between

the resonance peaks are called “free spectral range (FSR)”, as illustrated in Figure 1-11. [17] Note in the transmission spectra the distances between two neighboring peaks are almost identical for a set of resonance peaks generated by one resonance ring. That is because although n_{eff} is different at different wavelengths, in a narrow wavelength range, the variations between those free spectral ranges are quite small. In our experiments, the resonance wavelength can be determined by fitting the resonance peaks with Lorentzian functions. As the resonance peaks are sensitive to the surrounding medium’s refractive index within the evanescent wave range (0-400 nm), we can develop chemical- and bio-sensors by functionalizing the ring with special coatings to adsorb the chemicals and bio-analytes of interest. Details on these coatings will be discussed in chapter 2.

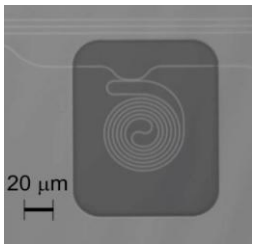

Figure 1-10 *Optical microscope image of a 936 μm long spiral ring resonator on a SOI chip. [17]*

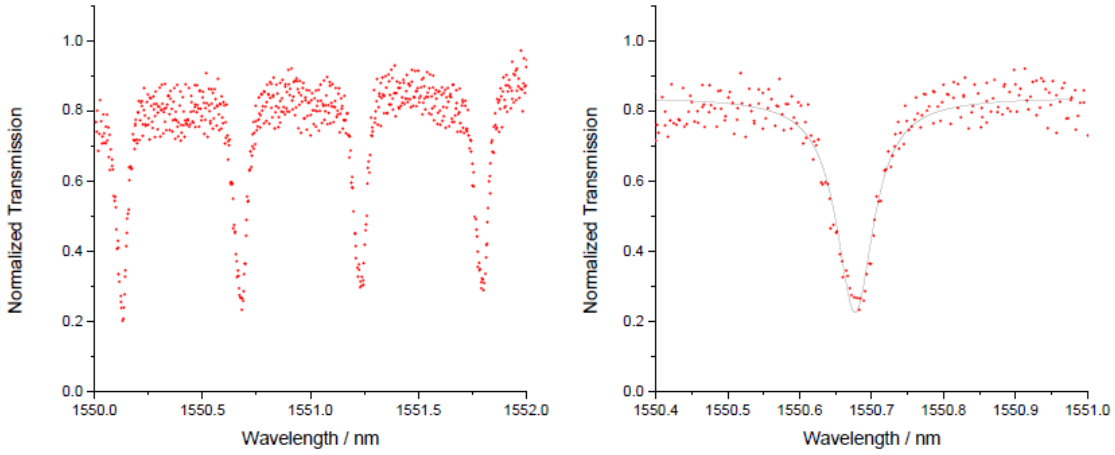

Figure 1-11 *Resonance spectra of a 936 μm long spiral ring resonator. A signal peak can be fitted with a Lorentzian function, as shown on the right. [17]*

Chapter 2

Evanescent Wave Sensor Functionalization Methods

Evanescent wave sensors measure surrounding medium refractive index changes within the evanescent field ranges. One challenge for refractive index sensing is that the medium's refractive index can be influenced by many factors, including selective binding, unselective binding, density (pressure) change, and temperature change, etc. [19] As a result of these interferences, numerous surface functionalization methods have been developed to make the chemical or biological sensors more selective. Coating the sensor surface with a layer of molecules or a layer of a micro-extraction phase that can selectively bind with or extract the analytes of interest brings another benefit: the coatings can adsorb analytes from the air or bulk solutions, thereby increasing the effective concentrations interacting with the evanescent fields, and thus lowering the detection limits. A few commercial evanescent wave-based chemical or biological sensors are summarized in Table 2-1.

Table 2-1 Commercial optical waveguide chemical- and bio- sensors.

Functionalization group	Analytes or goals	Detection Method	Manufacturer
fluorescent probe molecule	Toxins, pathogens, explosives, environmental contaminants	Evanescent wave-based fluorescence (RAPTOR and BioHawk)	Research International [20]
fluorescent probe molecule	Disease diagnosis and toxin quantitation	Planar waveguide fluorescence immunoassay array system	MBio Diagnostics [21]
carboxymethyl-dextran and polycarboxylate	Drug discovery	Waveguide interferometer integrated microfluidics	Creoptix [22]
Antibody	Bacteria, viruses, yeast, biomarkers	Waveguide interferometry	Ostendum [23]
Bio-molecule	Antibodies	Micro-ring resonator	Genalyte [24]
Proteins	Drug discovery	Surface plasmon resonance	Biacore [25]

Three common functionalization methods are discussed in this chapter: bio-molecule functionalization, polymer functionalization, and porous silica functionalization. The porous silica functionalization, as the chosen method for this research, is discussed in some detail.

2.1 Bio-molecule Functionalization for Biosensors

2.1.1 Antibody Functionalization

Antibodies are proteins generated by animal immune systems to bind pathogens. They are widely used in biosensor functionalization for several reasons. First, they greatly increase the sensor sensitivities and selectivities due to their specific binding abilities with target molecules. This reduces the necessity for sample purification and preconcentration. Second, different pathogens have different corresponding antibodies. An antibody biosensor platform can easily be expanded by exchanging the antibodies, which are readily available. As a result, this method is quite versatile. Third, this method is flexible: antibodies can be modified to have high affinities to particular analytes or to be responsive to related analytes. Also, methods to attach antibodies on sensor surfaces are available in the literature from many years of intensive studies. [19]

However, antibody functionalization has several disadvantages. First, antibodies are proteins, which are only stable in a narrow range of environmental conditions, including pH, temperature, and ionic strength. As a result, many bio-sensors can only be operated inside laboratories in a well-conditioned system. Reversibility and reproducibility are poor for some antibodies. Some antibodies are not selective enough, giving false positive, while false negative results ("failure to detect") arise when antibodies have degraded, become detached, or blocked by small molecule interferences. [19] Antibodies do not generally exhibit strong responses to small molecules or metal ions.

2.1.2 Aptamers Functionalization

Aptamers have been developed as an alternative to antibodies to overcome some of the disadvantages with antibodies. They are custom-synthesized nucleic acid sequences that can selectively bind target molecules. As a result, they are also known as "synthetic antibodies". Aptamers can be designed and synthesized by a method called "systematic evolution of ligands by exponential enrichment (SELEX)" to have a specific binding ability to target analytes. As nucleic acids can tolerate harsher environmental conditions than proteins, an aptamer biosensor can work in a wider range of environmental conditions,

making them better candidates than antibodies for field-deployable environmental sensors. Different aptamers have been developed for pathogen sensing [26], mercury ion sensing [27], and algae toxin sensing [28].

2.1.3 Other Molecules for Biosensor Functionalization

Other less commonly used bio-functionalization methods include those with bacteriophages and carbohydrates. Phages are viruses that can bind to the surface of bacteria before injecting their DNA or RNA into the bacteria and consuming the hosts. The specific binding abilities between phages and bacteria have been used to design selective sensors for target bacteria. [29]

Carbohydrates have also been used as binding groups for pathogenic analytes. [30] Compared to antibodies, they are stable over a larger range of pH and temperature, but their selectivity and affinities (related to sensitivities) are much lower.

2.2 Polymer Functionalization

2.2.1 Molecularly Imprinted Polymer Functionalization

Molecularly Imprinted Polymers (MIPs) are polymers generated via polymerization of monomers and cross-linking agent in the presence of target molecules (template). After the polymerization, the target molecules are removed, leaving cavities that were previously occupied by the templates. The polymer shows a high affinity for the target molecules, because of the cavities' specific shapes and binding site positions.[31] A scheme of this process is shown in Figure 2-1. Researchers have developed a TNT-imprinted polymer as functionalization coating on a surface plasmon resonance (SPR) sensor surface. When the polymer adsorbed TNT, its refractive index increased and thereby shifted the SPR angle. The detection limit was shown to be as low as 1×10^{-8} mol/L. The sensor had no response to TNT analogs, such as 2,4,5-trinitrotoluene and 1,3,5-trinitrohexahydro-1,3,5-triazine, at a concentration of 1×10^{-4} mol/L. [32]

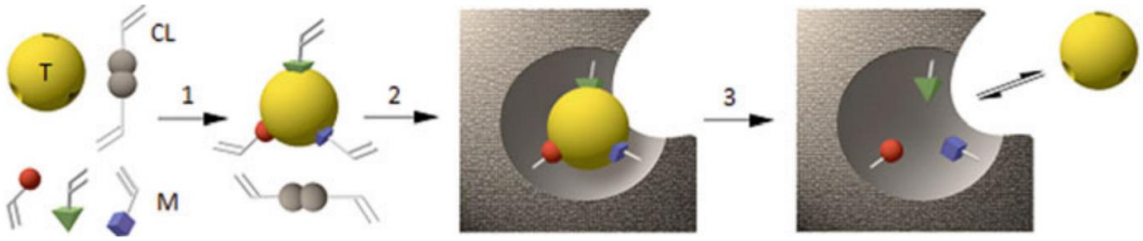

Figure 2-1 *Diagram showing general principle of molecular imprinting. A molecular template (T) is mixed with functional monomers (M) and a cross-linker (CL) resulting in the formation of a self-assembled complex (1). The polymerization of the resulting system produces a rigid structure bearing imprinted sites (2). Final removal of the template liberates cavities that can specifically recognize and bind the target molecule (3). (From [33])*

2.2.2 Siloxanes Functionalization for Volatile Organic Compound (VOC) Sensors

Siloxanes, such as poly(dimethylsiloxane) (PDMS), have been used to functionalize chemical sensors for VOCs. [19] These polymers are hydrophobic. Therefore they can adsorb and concentrate organic, non-polar VOCs from aqueous solutions and the gas phase and change their refractive index during the adsorption processes. Hydrophobic polymers can remove VOCs from water and air, so the processes are also micro-extraction processes. Since the adsorption process lacks selectivity, such extraction matrices are best suited if entire classes of compounds need to be quantified. Some studies have been performed to test modifications on siloxanes in an attempt to improve their selectivity. [19]

2.3 Porous Silica Functionalization

Micro/mesoporous silica materials – in essence, very porous forms of glass – have been widely studied in adsorbing, scrubbing, and extracting analytes from liquids. These processes are enabled because of the large surface area of these materials. [34] Their silica glass nature suggests good chemical resistance, high stiffness, good optical properties, and that they are compatible with silica-based optical waveguide sensors, such as long-period fibre gratings (LPG) and silicon-on-insulator waveguide sensors. The materials can be coated on waveguide surfaces using the sol-gel method. [34]

The sol-gel method is a “wet chemistry” process that can be carried out at moderate temperatures. To make homogeneous mesoporous silica, monomers, surfactants (templates), and catalysts are all

dissolved in a solvent and stirred for several hours ("aging") so that condensation and gel formation happen. After aging, the mixture is dried, and the surfactant is removed by either calcination or solvent refluxing. Two of the common monomers are tetramethoxysilane ($Si(OMe)_4$, TMOS) and tetraethoxysilane ($Si(OEt)_4$, TEOS), and the most common catalysts are acids, such as HCl. The condensation reaction is shown in Figure 2-2.

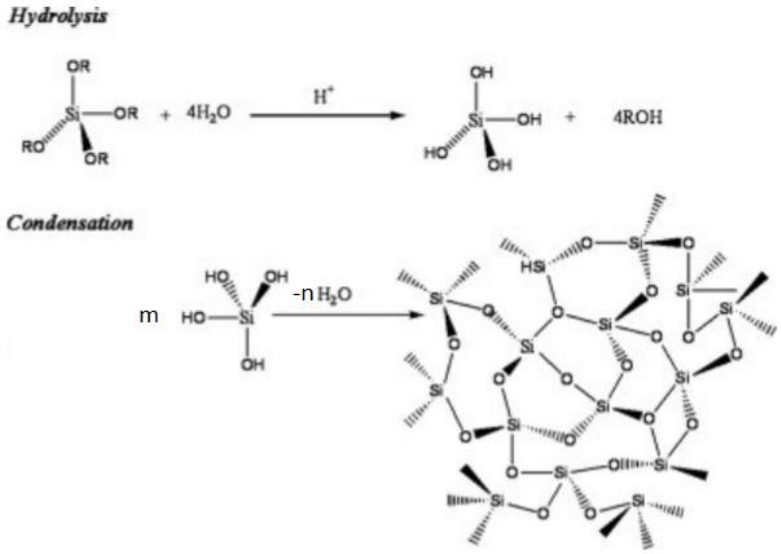

Figure 2-2 *Scheme showing the condensation of TEOS and formation of silica network. (from [35])*

This siloxane bond formation reaction starts during the aging process and does not stop until the drying process is complete. The reaction is not complete during the gel formation process, in which the surfactants come into play. The surfactants self-assemble into micelles, which may take different shapes such as spheres, rods, cylinders, etc. (see Figure 2-3). These ordered structures act as templates while the silica gel forms around them. Eventually, in the drying stage, the siloxane bond formation is complete, and the silica network becomes stiff. After the surfactant templates are removed, the cavities they occupied become channels and pores. The whole process is shown in Figure 2-4. The choices of templates, concentrations, solvents can be used to control the shape and size of the channels and pores. [34] The sol-gel mixture can be coated on the surface of an optical waveguide after the aging stage and before the drying stage, using various coating methods, such as spin coating and dip coating.[36]

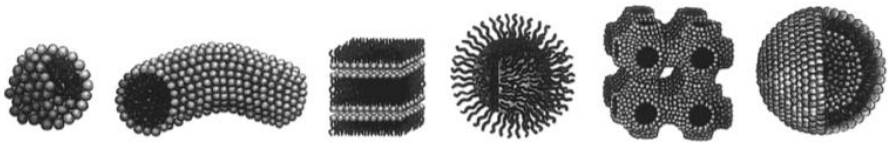

Figure 2-3 *Schematic representation of typical micellar mesophases. (from left to right): spherical, rod-like / cylindrical, lamellar / bilayer, inverse spherical, bicontinuous, vesicular. (from [36])*

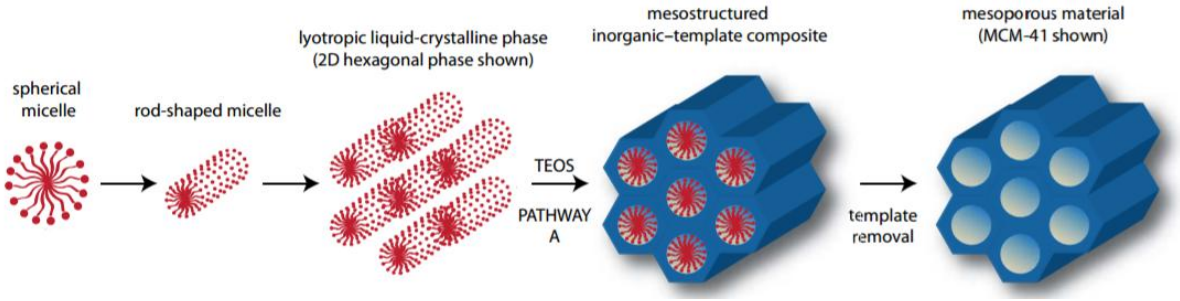

Figure 2-4 *Diagram showing the formation of mesoporous silica via a lyotropic liquid crystalline pathway. [37]*

Mesoporous silica materials are versatile, as different functional groups can be added to the silica networks. The precursors carrying the functional groups usually contain triethoxysilyl groups to form siloxane bonds with the monomers like TEOS. The following sections will discuss mesoporous silica materials with different functional groups. These groups are selected to bind specifically to non-metal ions (phosphate, nitrate, and ammonium ions) as well as heavy metal ions.

2.3.1 Functionalized Mesoporous Silica as Scrubbing Material for Phosphate and Nitrate ions.

Phosphate and nitrate ions are pollutants in water if their concentrations are above the regulated standards in the particular water systems. Mesoporous silica and alumina are promising materials to scrub these ions from water. [38, 39] Their high affinity for silica makes mesoporous silica coatings also good candidates for sensor materials. To increase its affinity for those ions, functionalization of silica is necessary. Previous research has shown that functionalizing mesoporous silica with amine groups can increase its affinity for phosphate and nitrate ions. [38, 39] (3-Aminopropyl)triethoxysilane (Figure 2-5) is one of the amines that are used to introduce amine groups into mesoporous silica.

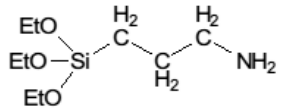

Figure 2-5 *Structure of (3-Aminopropyl)triethoxysilane.*

2.3.2 Tetrasulfide-functionalized Mesoporous Silica Coatings on LPG Sensor

Tetrasulfide groups have been introduced to mesoporous silica to adsorb heavy metal ions. Previous research has shown that mesoporous silica made by condensation between tetraethoxysilane (TEOS) and bis[3-(triethoxysilyl)propyl]tetrasulfide (TESPT) adsorbs heavy metal ions. [15] One study reported that the tetrasulfide mesoporous silica that was made by condensation between TEOS and TESPT using CTAB as surfactant (ratio CTAB : TEOS : TESPT : NaOH : H_2O = 0.125 : 1.00 : 0.125 : 0.32 : 615) could adsorb Ag(I) and Cd(II) ions up to 6.11%(w/w) and 1.7%(w/w), respectively. [15] The corresponding values of mesoporous silica powder without tetrasulfide groups were 0.34%(w/w) and 0.01%(w/w). This proved that the tetrasulfide-functionalized mesoporous silica did have high affinity for Ag(I) and Cd(II) ions.

In 2006, Hanumegowda *et al.* reported a thiol monolayer functionalized microsphere optical ring resonator as an optical sensor for Hg(II) ion detection. The detection limit was approximately 50 ppb (ppb defined as ng/mL), and Hg(II) ions bound to thiol group in a 1:3 ratio. They developed a Langmuir model to describe the adsorption process. [40]

A refractive index sensor based on a long-period grating was coated with a tetrasulfide-functionalized mesoporous silica film at Queen's University. Du *et al.* (2010) coated a tetrasulfide-functionalized mesoporous silica film on the LPGs to make sensors for Pb(II) and Hg(II) ions. [15] Figure 2-6 shows the scheme and reactions used in the study. In addition to all the reagents mentioned earlier, titanium tetraisopropoxide ($Ti(^{i}OPr)_4$) was used to tune the refractive index of the film to match the refractive index of the cladding. The films were coated on LPGs, whose resonance peak shifted when the films were immersed in Pb(II) solutions at different concentrations (Figure 2-7). The coatings could be recovered by immersing the film in 1 M HCl solution for 20 minutes. The film eventually degraded after repeated testing.

Based on this research, the plan was made to coat tetrasulfide-functionalized mesoporous silica film on silicon-on-insulator (SOI) chips. In comparison to coating film on the optical fibre surface, the coating on the upper surface of flat SOI chips is more stable, less strained and therefore is much less likely to crack. Instead of the dip coating method as was done in the research of Du *et al.*, the spin coating method will be used to control the film thickness and to improve reproducibility. Moreover, SOI chips are easier to interface with microfluidics, making them capable of measuring the heavy metal ion adsorption and desorption kinetics in small flowing samples of aqueous solutions.

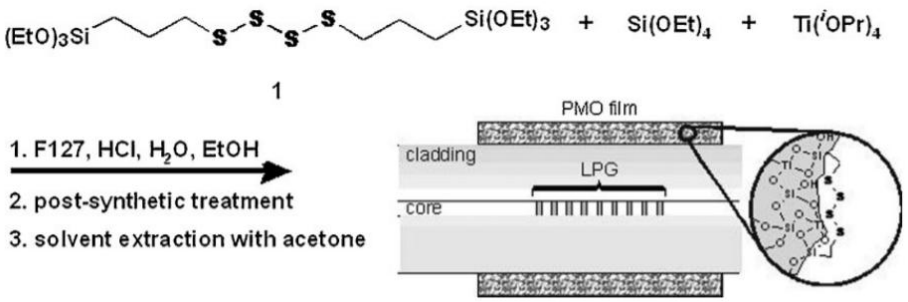

Figure 2-6 *Synthesis of tetrasulfide- and Ti-containing mesoporous materials as coatings for LPG chemical sensors. [15]*

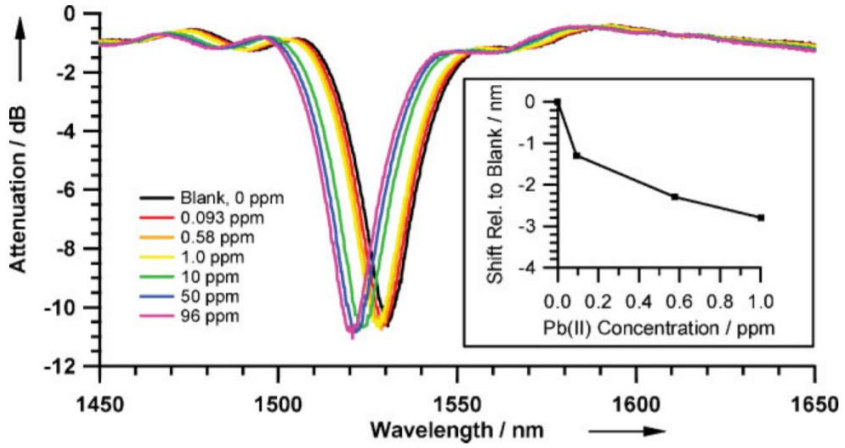

Figure 2-7 *Optical response for the LPG coated with the PMO film to aqueous DMSO solutions (RI = 1.402 at 1550 nm) of Pb(II) of increasing concentration as observed by the LPG attenuation spectra. (inset) Resonant peak positions shift as a function of analyte concentration. [15]*

Chapter 3

Theory of Adsorption and Desorption, Models, and Equations

This chapter discusses the theories of adsorption and desorption, which set the theoretical foundation for the discussion of metal ion adsorption and desorption processes on thin mesoporous silica films. Kinetic models are built, and equations are derived that serve to fit the experimental data in subsequent chapters.

3.1 Adsorption Theory

The attachment of particles to a surface is called adsorption, and the reverse process is called desorption. The extent of surface coverage is defined as fractional coverage, θ .

$$\theta = \frac{number\ of\ \ adsorption\ sites\ occupied}{Total\ number\ of\ \ adsorption\ sites} \tag{3.1}$$

For gas-solid adsorption, the variation of θ with pressure at a chosen temperature is called the adsorption isotherm. [41] Many theories have been proposed to describe and understand surface adsorption and desorption. Four of the most important ones are discussed in this chapter, including the Langmuir adsorption theory, Brunauer–Emmett–Teller (BET) theory, the Temkin theory, and the Freundlich theory. The second part of this chapter discusses models based on the Langmuir Theory.

3.1.1 The Langmuir Adsorption Theory

The basic assumptions for Langmuir adsorption is (1) monolayer adsorption, (2) only one kind of adsorption sites exists and all sites are equivalent, and (3) the ability of a molecule to adsorb at a given site is independent of the occupation of neighboring site, which implies no interactions between adsorbed molecules. [41] Under these three assumptions, the Langmuir isotherm is:

$$\theta = \frac{Kp}{1 - Kp} \tag{3.2}$$

where K is the equilibrium constant, and p is pressure. Figure 3-1 shows isotherms for different values of K. Since K is a function of temperature, these could, for example, be isotherms for a process at three different temperatures. [41] From the figure, it is clear that the fractional coverage approaches one at high pressure. For a given pressure, the fractional coverage is high when K is high.

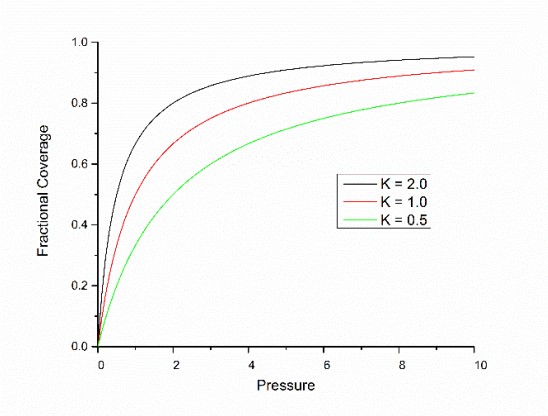

Figure 3-1 *Langmuir isotherm for non-dissociative adsorption for different K values.*

3.1.2 The Brunauer–Emmett–Teller (BET) Theory

The Brunauer–Emmett–Teller (BET) theory is based on the assumption that the initially adsorbed layers can act as a substrate for further adsorption. The BET isotherm is:

$$\frac{V}{V_{monolayer}} = \frac{cz}{(1-z)\{1-(1-c)z\}} \tag{3.3}$$

Where $z = p/p^*$, p is pressure and p^* is the vapor pressure above a layer of adsorbate that is more than one molecule thick and which resembles a pure bulk liquid. V is the volume of the adsorbed material; $V_{monolayer}$ is the volume of a single layer of adsorbate; and c is a constant. [41] Figure 3-2 shows the BET isotherm.

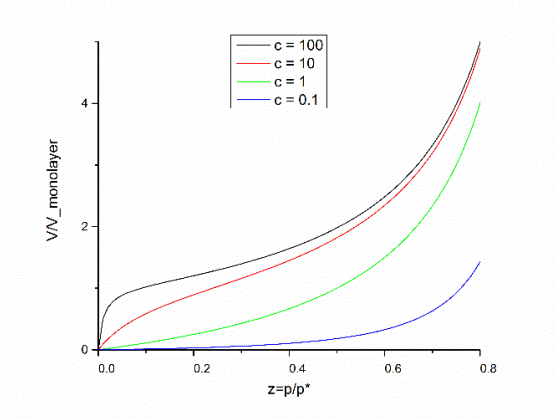

Figure 3-2 *BET isotherm at different values of c.*

3.1.3 The Temkin Theory

The Temkin Theory is a modification of Langmuir theory. The changed assumption is that some sites are more favorable for adsorption than other sites and are occupied first. The Temkin isotherm is:

$$\theta = c_1 \ln(c_2 p) \tag{3.4}$$

where c_1 and c_2 are constants. [41]

3.1.4 The Freundlich Theory

The Freundlich Theory considers the substrate - substrate interactions. The Freundlich isotherm is:

$$\theta = c_1 p^{1/c_2} \tag{3.5}$$

where c_1 and c_2 are constants. [41]

3.2 Models and Equations

This section discusses the models used in this thesis to analyze the experimental data.

3.2.1 Single Adsorption Site Model

In a typical experiment, a metal ion solution sample with a known concentration flows above the coating to which the metal ion is adsorbed. This binding process involving metal ion M binding to single binding site Y can be described by the equilibrium reactions

$$M + Y \underset{k_d}{\overset{k_a}{\rightleftarrows}} [MY] \tag{3.6}$$

where k_a and k_d are the forward reaction constant and backward reaction constant, respectively.

In 1898, Lagergren reported a first order rate equation to describe liquid to solid surface adsorption processes for the above reaction.[42] Under the assumption that (a) all the binding sites are equivalent, (b) the adsorbed ions do not interact with unoccupied binding sites (Langmuir assumption), and (c) the supply of metal ions *M* is infinite, the kinetic equation to describe the adsorption process can be represented as

$$\frac{d[MY]}{dt} = k_a [M][Y] - k_d [MY] \tag{3.7}$$

where [*MY*] (mol/g) is the loading of the adsorbed metal, [*Y*] (mol/g) is the density of the empty binding sites, [*M*] is the constant concentration (mol/L) of the metal ions in solution, and k_a (L mol^{-1} s^{-1}) is the second order rate constant. The equation can be simplified by writing the absorption as a first order process with $k_a' = k_a$ [M] as the pseudo-first order rate constant of adsorption ($second^{-1}$).

$$\begin{aligned} \frac{d[MY]}{dt} &= k_a'\left([Y]_0 - [MY]\right) - k_d [MY] \\ &= k_a'[Y]_0 - \left(k_a' + k_d\right)[MY] \end{aligned} \tag{3.8}$$

By integrating Equation (3.8) one obtains

$$[MY](t) = A\exp\left(-\left(k_a' + k_d\right)t\right) + \frac{k_a'[Y]_0}{\left(k_a' + k_d\right)} \tag{3.9}$$

where the total binding site concentration is the sum of empty and occupied binding sites

$$[Y]_0 = [Y] + [MY] \tag{3.10}$$

The factor *A* can be obtained from the boundary condition [*MY*](*t*=0) = 0 to give

$$[MY](t) = \frac{k_a'[Y]_0}{\left(k_a' + k_d\right)}\left[1 - \exp\left(-\left(k_a' + k_d\right)t\right)\right] \tag{3.11}$$

At equilibrium ($t \rightarrow \infty$), the equation simplifies to

$$[MY]_{\max} = \frac{k_a'[Y]_0}{k_a' + k_d} = \frac{k_a[M][Y]_0}{k_a[M] + k_d} \tag{3.12}$$

Therefore, the equilibrium capacity for the metal ions in the film depends not only on the rate constants but also on the total number of available binding sites $[Y]_0$ as well as the metal ion concentration in solution. This dependence on the dissolved ion concentration can be exploited to linearize equation (3.12) and to obtain

$$\frac{1}{[MY]_{\max}} = \frac{1}{[Y]_0} + \frac{k_d}{k_a[Y]_0}\frac{1}{[M]} \tag{3.13}$$

Once values for $[MY]_{\max}$ are obtained using fits of experimental adsorption curves to equation (3.13) at different concentrations $[M]$, one can obtain the number of available sites $[Y]_0$ from the intercept in a linear plot of $[MY]_{\max}^{-1}$ versus $[MY]^{-1}$. The ratio of the rate constants is found from the corresponding slope.

The concentration of the bound metal ions $[MY](t)$ is related to refractive index through the Lorentz-Lorenz equation – see Chapter 3 section 3.3.

The rate equation describing the desorption processes can be derived from equation (3.7)

$$\frac{d[MY]}{dt} = k_a[M][Y] - k_d[MY] \tag{3.14}$$

When rinsing with deionized water (DI Water) $[M] = 0$ and the remaining expression is readily integrated to yield

$$[MY](t) = [MY]_0\left[\exp(-k_d t)\right] \tag{3.15}$$

Here, $[MY]_0$ is the quantity of the ions in the coating at the start of the desorption process $t = 0$. If the film had been completely equilibrated before desorption, $[MY]_0 = [MY]_{\max}$, but in the experiments described in this thesis, this is typically not the case.

3.2.2 Double Adsorption Site Model

For adsorption of ions from the liquid into a coating having two distinct binding sites *X* and *Y*, I assume that the two binding sites are independent, i.e. that ions do not migrate between binding sites and,

also, that there are no interactions between adsorbed ions. The adsorption and desorption equations are then reduced to two parallel and independent equilibria

$$\begin{aligned} M + X &\underset{k_{d,X}}{\overset{k_{a,X}}{\rightleftharpoons}} [MX] \\ M + Y &\underset{k_{d,Y}}{\overset{k_{a,Y}}{\rightleftharpoons}} [MY] \end{aligned} \tag{3.16}$$

and therefore

$$\frac{d\left([MX]+[MY]\right)}{dt} = k_{a,X}[M][X] - k_{d,X}[MX] + k_{a,Y}[M][Y] - k_{d,Y}[MY] \tag{3.17}$$

where, as before, each of the two pseudo-first-order rate constants for adsorption depends on the constant concentration of metal ions, $k_{a,X}' = k_{a,X}[M]$ and $k_{a,Y}' = k_{a,Y}[M]$.

Integration of the respective rate laws gives

$$\begin{aligned} \left([MX]+[MY]\right)(t) &= \frac{k_{a,X}'[X]_0}{\left(k_{a,X}'+k_{d,X}\right)}\left[1-\exp\left(-\left(k_{a,X}'+k_{d,X}\right)t\right)\right] \\ &\quad + \frac{k_{a,Y}'[Y]_0}{\left(k_{a,Y}'+k_{d,Y}\right)}\left[1-\exp\left(-\left(k_{a,Y}'+k_{d,Y}\right)t\right)\right] \\ q(t) &= q_{e,X}\left[1-\exp\left(-\left(k_{a,X}'+k_{d,X}\right)t\right)\right] \\ &\quad + q_{e,Y}\left[1-\exp\left(-\left(k_{a,Y}'+k_{d,Y}\right)t\right)\right] \end{aligned} \tag{3.18}$$

where $q(t) = ([MX]+[MY])(t)$ describes the total concentration of adsorbed ions in the coating at time t. The quantities, $q_{e,X}$ and $q_{e,Y}$, are the adsorption capacities at equilibrium for each of the two binding sites, respectively.

Similar to equation (3.18) the desorption rate under flowing DI water can be described as a sum of two independent processes

$$\left([MX]+[MY]\right)(t) = [MX]_0 \exp\left(-k_{d,X}t\right) + [MY]_0 \exp\left(-k_{d,Y}t\right) \tag{3.19}$$

where $[MX]_0$ and $[MY]_0$ are the metal loadings in the coating at time $t = 0$, while $k_{d,X}$ and $k_{d,Y}$ are the first order rate constants associated with the desorption processes for each of the two binding sites, respectively.

In the experiments, the values for the desorption rate constants are valuable as they allow one to obtain the adsorption rate constants, k_a', and the number of respective available binding sites $[X]_0$ and $[Y]_0$ using the fitting parameters for the adsorption process with equation (3.18). These fitting parameters can be obtained by fitting the measured refractive index change to equation (3.19).

While the desorption processes are first order reactions and the rate constants are obtained directly from either a fit to Equation (3.15) or (3.19), the adsorption process is a second order reaction with a rate constant $k_a' = k_a[M]$ that depends on the concentration of the metal ion in solution and the measured pseudo-first order rate constant, k_a. Therefore, the second order rate constant is obtained as the slope of a linear fit of k_a as a function of $[M]$. See Chapter 5 for the application of this method.

3.2.3 Method of Initial Rates Calculation

The rate constants for single binding sites can be obtained from the slope of the response curve by taking the derivatives of equation (3.11) and (3.15)

$$\begin{aligned} &\text{adsorption:} \quad \left.\frac{d[MY](t)}{dt}\right]_{t=0} = k_a[M][Y]_0 \\ &\text{desorption:} \quad \left.\frac{d[MY](t)}{dt}\right]_{t=0} = -k_d[MY]_0 \end{aligned} \tag{3.20}$$

When two binding sites are present, the derivatives of equations (3.18) and (3.19) are taken.

$$\begin{aligned} &\text{adsorption:} \quad \left.\frac{d\left([MX]+[MY]\right)(t)}{dt}\right]_{t=0} = \left(k_{a,X}[X]_0 + k_{a,Y}[Y]_0\right)[M] \\ &\text{desorption:} \quad \left.\frac{d\left([MX]+[MY]\right)(t)}{dt}\right]_{t=0} = -k_{d,X}[MX]_0 - k_{d,Y}[MY]_0 \end{aligned} \tag{3.21}$$

From both equations, one would expect a linear dependence of the initial adsorption rate on the concentration of metal ions $[M]$. This is important, because the initial rate can be used to quantify $[M]$ after calibration and regardless of the uptake mechanism.

3.3 Relationship Between Metal Loading in the Silica Film and Refractive Index

Next, the concentration of the metal ions $q(t) = ([MX]+[MY])(t)$ in the coating must be related to the measured refractive index n(t) of the coating. It will be shown below that the correlation between the metal ion concentration in the film and its refractive index is linear to a good approximation.

It was demonstrated previously that the refractive index of mixtures of solvents could be readily calculated using the indices of the components and the additivity of the polarizabilities.[43] The polarizabilities of the different solutions are expected to be a weighted sum of the polarizabilities of the constituents.

$$\alpha_{LL}(x) = \sum_i x_i \alpha_i \tag{3.22}$$

This equation has been validated several times - most recently by Saunders *et al.* [17]. Only slight deviations (<1%) have been observed. In all systems described in this thesis, the material consists of a water-filled mesoporous silica film that contains metal ions in variable but comparably low concentrations. To determine the polarizabilities, α_1 and α_2, of the neat components, their respective known densities, ρ_i, and the measured refractive indices, n_i, are used with the Lorentz-Lorenz equation

$$\frac{n_i^2 - 1}{n_i^2 + 2} = \frac{\rho_i N_A}{3\varepsilon_0} \frac{\alpha_i}{M_i} \tag{3.23}$$

where N_A is Avogadro's number, M_i is the respective molar mass, and ε_0 is the vacuum permittivity. The refractive index of mixtures can accordingly be calculated from mole fractions x_1 and $x_2 = (1 - x_1)$, the density of the mixture, and the electronic polarizabilities and densities of the neat compounds.

In this thesis the water filled mesoporous silica film can be treated as a binary mixture of glass (M_{glass} = 60g/mol) and water (M_{water} = 18 g/mol) with approximate indices of n_{SiO2} = 1.45 and n_{H2O} = 1.31 at 1550 nm and densities of ρ_{SiO2} = 2400 kg/m^3 and ρ_{H2O} = 1000 kg/m^3, respectively. By combining equation (3.22) with (3.23), the refractive index of the mesoporous silica film is obtained:

$$
\begin{aligned}
&\frac{{n_{film}}^2-1}{{n_{film}}^2+2} \\
&=\frac{N_A}{3\varepsilon_0}\frac{\rho_{film}}{M_{film}}\left(x_{water}\alpha_{water}+x_{glass}\alpha_{glass}\right) \\
&=\frac{\rho_{film}}{M_{film}}\left(x_{water}\frac{M_{water}}{\rho_{water}}\frac{{n_{water}}^2-1}{{n_{water}}^2+2}+x_{glass}\frac{M_{glass}}{\rho_{glass}}\frac{{n_{glass}}^2-1}{{n_{glass}}^2+2}\right) \\
&=\left(\frac{x_{water}\rho_{water}+\left(1-x_{water}\right)\rho_{glass}}{x_{water}M_{water}+\left(1-x_{water}\right)M_{glass}}\right) \\
&\quad\left(x_{water}\frac{M_{water}}{\rho_{water}}\frac{{n_{water}}^2-1}{{n_{water}}^2+2}+\left(1-x_{water}\right)\frac{M_{glass}}{\rho_{glass}}\frac{{n_{glass}}^2-1}{{n_{glass}}^2+2}\right)
\end{aligned}
\tag{3.24}
$$

In this calculation, the volume of the films is assumed to remain constant as the fraction of water is changed, i.e. the density of the film can be obtained by a weighted sum of the density of its components. The refractive index of the film is then obtained as a function of the mole fractions of water and glass in the system, as shown in Figure 3-3. This function is not linear as has sometimes been assumed in the literature.

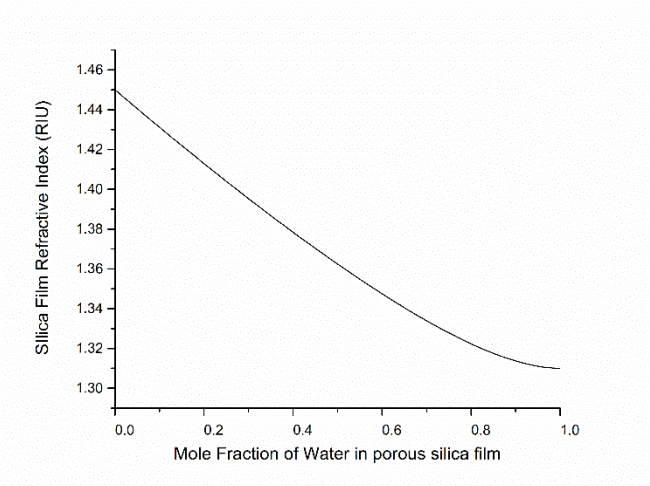

Figure 3-3 *Refractive index of porous silica film with water filling its pores as a function of the mole fraction of water. The refractive index decreases as the water mole fraction increases.*

Similarly one can determine the dependence of the system's refractive index on the loading of the film with metal ions. The above calculation is repeated but using the polarizability, α_{Pb} and mole fraction, x_{Pb} of lead.

$$
\begin{aligned}
&\frac{n_{system}{}^2-1}{n_{system}{}^2+2} \\
&=\frac{N_A}{3\varepsilon_0}\frac{\rho_{system}}{M_{system}}\left(x_{Pb}\alpha_{Pb}+(1-x_{Pb})\alpha_{film}\right) \\
&=\frac{\rho_{system}}{M_{system}}\left(x_{Pb}\frac{N_A\alpha_{Pb}}{3\varepsilon_0}+(1-x_{Pb})\frac{M_{film}}{\rho_{film}}\frac{n_{film}{}^2-1}{n_{film}{}^2+2}\right) \\
&=\left(\frac{x_{Pb}\rho_{Pb}+(1-x_{Pb})\rho_{film}}{x_{Pb}M_{Pb}+(1-x_{Pb})M_{film}}\right)\left(x_{Pb}\frac{N_A\alpha_{Pb}}{3\varepsilon_0}+(1-x_{Pb})\frac{M_{film}}{\rho_{film}}\frac{n_{film}{}^2-1}{n_{film}{}^2+2}\right)
\end{aligned}
\tag{3.25}
$$

Several different values of α_{Pb2+} were found in different published papers. Dimitrov and Sakka (1995) reported 4.031×10^{-40} F•m^2 for Pb^{2+} cation and 3.838×10^{-40} F•m^2 for PbO oxide.[44] Thierfelder *et al.* (2008) reported 7.79×10^{-40} F•m^2 for Pb atom[45]. M. E. Hanni *et al.* (2010) reported 2.24×10^{-40} F•m^2 for gas phase Pb^{2+} cation by resonant excitation Stark ionization spectroscopy. [46] The exact polarizability value in this work should be in this range, but it is hard to calculate or measure. For the following calculation, 4.031×10^{-40} F•m^2 was used. However, it should be remembered that this value is subject to change from future research. Mon et. al. (1979) reported 3.094×10^{-40} Fm^2 as the polarizability for Hg^{2+}, and this value was used in the following calculation. [47] Other constants used for the data analysis in the following chapters are listed in Table 3-1. The number in the brackets are the uncertainty of the least decimal places.

Table 3-1 Pb(II) and Hg(II) doping response to the MPS film(wet and dry)

	Pb(II)	***Hg(II)***
α(F•m²)	4.03×10^{40} [44]	3.09×10^{-40} [47]
Density(g/cm³)	11.34×10^{3} [48]	14.184×10^{3} [48]
Slope (RIU/x_i)	0.780(4)	1.209(5)
Atomic weight(g/mol)	207.2 [41]	200.59 [41]
RIURefractive index/Mass fraction(wet) (RIU•g(film)/g(metal))	0.148(2)	0.236(3)
Mass fraction(dry) (RIU•g(film)/g(metal))	0.113(1)	0.181(2)

To estimate Pb(II) and Hg(II) doping response of the film, we assume x_{water} = (1- x_{glass}) = 0.3 to 0.5 and calculate M_{film} = 39.2 g/mol, ρ_{film} = 1700 kg/m^3, and n_{film} = 1.3624. Figure 3-4 shows the index as a function of the mole fraction of Pb in the film, for films with different porosities (x_{water} = 0.3, 0.4, 0.5)

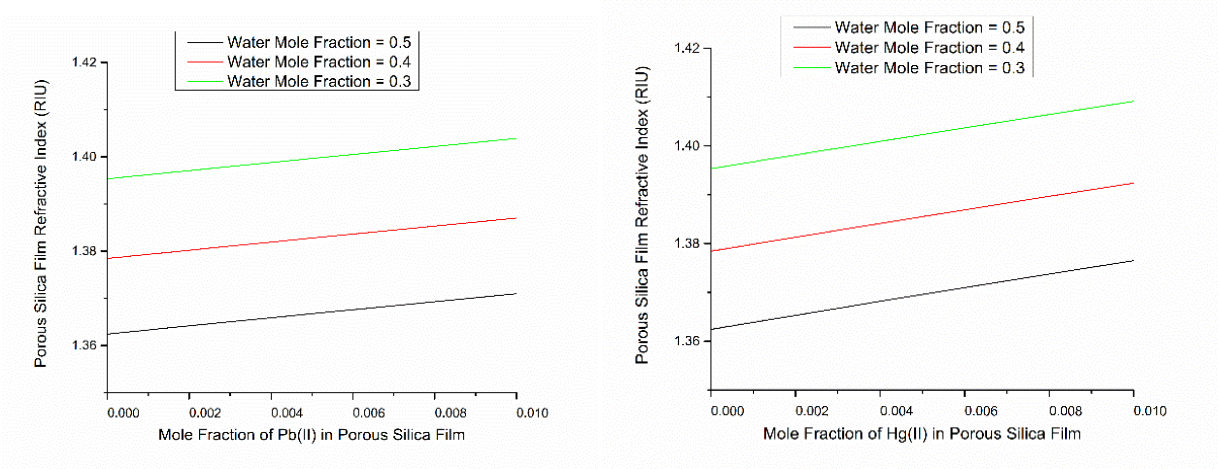

Figure 3-4 *Porous silica refractive index as a function of Pb(II) and Hg(II) mole fraction at different porosity (x_{water} = 0.3, 0.4, 0.5). (Left) The refractive index changes linearly with Pb(II) loading at low Pb loadings (0-0.01). (Right) The refractive index changes linearly with Hg(II) loading at low Hg loadings (0-0.01). The maximum loading for both ions in this thesis is well below 0.01, which is in the linear range.*

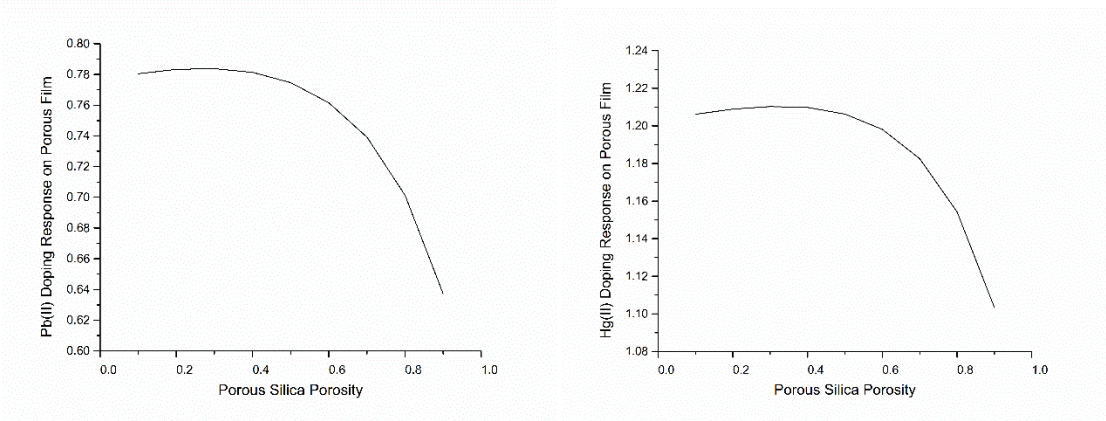

Figure 3-5 *Pb doping response on porous silica film as a function of porosity. In the range of x_{water} = 0.3-0.5, the doping responses are varying by a small amount, centered at 0.78 RIU/mole fraction for Pb, and 1.21 RIU/mole fraction for Hg.*

It is apparent that up to a loading of 1 mol% of Pb(II) and Hg(II) the film refractive index changes linearly. The effect of doping the water-filled film with Pb(II) and Hg(II) depends somewhat on the porosity. In the porosity range of x_{water} = 0.3-0.5 the doping responses (the slopes in Figure 3-4) are 0.780 RIU/mole fraction and 1.209 RIU/mole fraction for Pb(II) and Hg(II), respectively.

It is practical to convert the unit "mole fraction" to mol(Pb)/mol(SiO_2,H_2O) and mol(Hg)/mol(SiO_2,H_2O) to weight fraction using $M_{film(wet)}$ = 39.2 g/mol and $M_{film(dry)}$ = 30.0 g/mol. The results are also shown in Table 3-1.

The refractive index changes observed in these experiments are in the range of $\Delta n = 10^{-5}$ to 10^{-3} RIU, i.e. they are entirely in the linear portion of Figure 3-4. Assuming the porosity of this film to be near x_{water} = 40%, it can be concluded that the mole fraction of Pb or Hg in the films is in the linear range of $x_{Pb} = 10^{-5}$ to 10^{-3} (10^{-3} to 0.1 mol %).

Most importantly, these estimates show also that the rate constants obtained from the kinetic response curves can be directly related to the concentration of the lead ions in the film. The curves are obtained by measuring the resonance peak shifts of the ring resonators, which are then converted into refractive index changes using an experimentally obtained calibration curve. Using the linear relation of Δq(Pb) = 0.780 RIU/mole fraction(Pb) or Δq(Hg) = 1.209 RIU/mole fraction(Hg), all response curves can be readily rescaled to reflect Pb or Hg concentration changes in the film.

Chapter 4

Experimental Design, Setup, Data Collection, and Processing

This chapter discusses the temperature correction on tandem ring resonator, coupling laser light into and out of the waveguide, data collection and data processing, microfluidic device development, liquid sample pumping system, ring resonator calibration, as well as chip coating and post-treatment procedure. The SOI chips used in this research are provided by the National Research Council of Canada (Ottawa, ON).

4.1 Temperature Effects and Tandem Ring Resonators

A pair of tandem ring resonators with a large ring and a small ring sharing the same bus waveguide was used in this research. Figure 4-1(left) shows a microscope image of the ring resonators that are a part of the SOI chip.

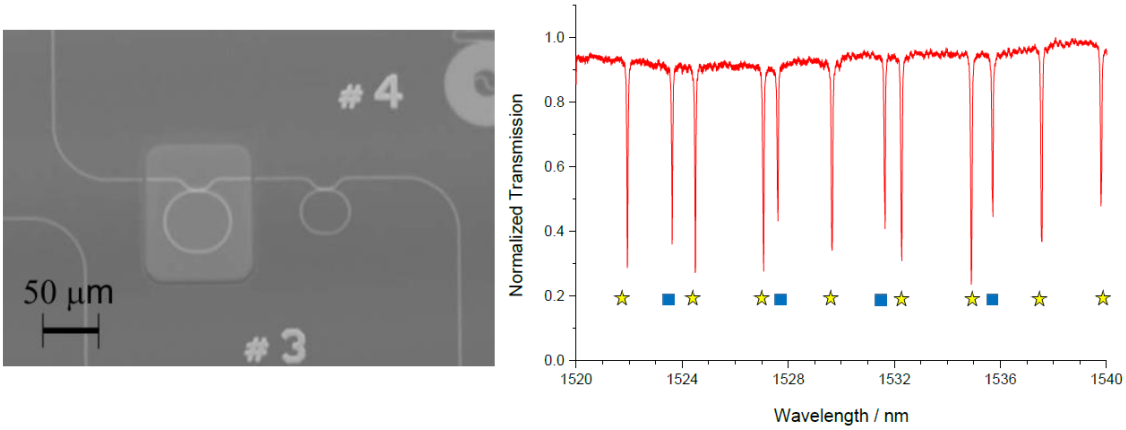

Figure 4-1 *Optical profilometer image and a transmission spectrum of a tandem ring resonator. (Left) the sensing ring and reference ring had circumferences of 185 µm and 134 µm, respectively. (Right) The resonances of the two rings could be separated as they have different free spectral ranges ($\Delta\lambda_{FSR}$). Here the free spectral range of the sensing and reference rings were $\Delta\lambda_{FSR}$ = 2.5 nm, 4.0 nm respectively. The sensing resonances were denoted by the yellow stars and the reference resonances with blue squares. From [17]*

The tandem ring resonators were designed to correct wavelength shifts caused by thermal expansion of the ring-resonators. This was important during the test as temperature fluctuations could be a

major source of error, especially during short- to long-term testing (more than one hour). The reference ring (the smaller one of the two) was covered in a layer of silica so that its evanescent field did not interact with analytes. The sensing ring (the larger one of the two) was not covered. The temperature effects on the reference ring and sensing ring were determined to be 49.9 pm/K and 62.5 pm/K, respectively.[49] The corrected peak shifts were readily calculated using

$$\lambda_{sens,corr}(t) = \lambda_{sens}(t) - \left[\left(\lambda_{ref}(t) - \lambda_{ref}(t=0)\right)\times(49.9/62.5)\right] \quad (4.1)$$

where λ_{sens} and λ_{ref} represent sensing peak positions and reference peak positions, $\lambda_{sens,corr}$ represent temperature corrected sensing peak position.

The effect of the temperature correction using simultaneous measurements of the resonance wavelength of the reference ring is shown in Figure 4-2. The sensing signal was much more obvious after the signal was corrected for the periodic temperature fluctuations caused by the air conditioning system.

A simple experiment was conducted to confirm that the fluctuations were indeed caused by the varying temperature in the lab. The resonance wavelength of the reference ring was related to the room temperature, which was measured by using a USB temperature probe (OM-EL-USB Omega, Laval, QC), as shown in Figure 4-3. All the data reported in this thesis were temperature corrected unless specifically noted otherwise.

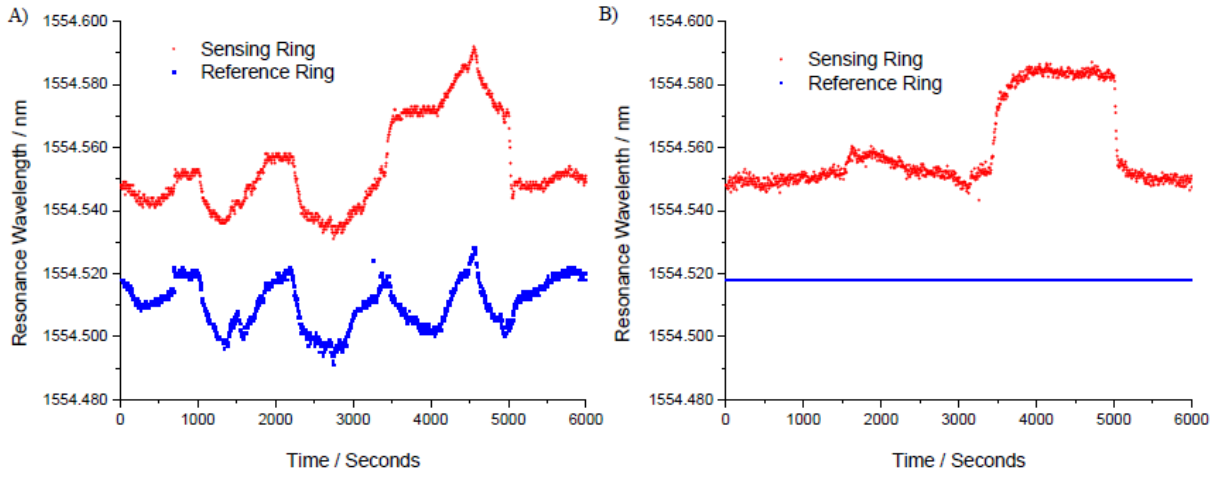

Figure 4-2 *Compensation of temperature effects from the resonance shifts of the reference ring of a tandem ring resonator. A) The resonance wavelength of the sensing and reference peaks shown over a 6000 s period. B) The temperature-related resonance shifts have been subtracted from the sensing and reference rings using temperature sensitivities of 49.9 pm/℃ and 62.5 pm/℃ for the two rings respectively. From [17]*

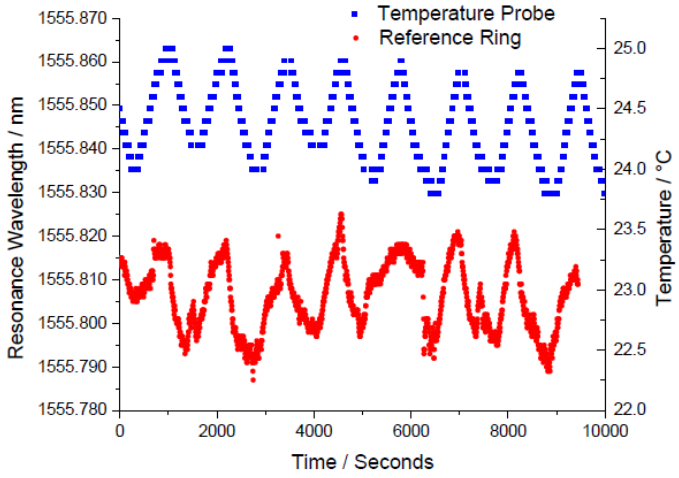

Figure 4-3 *The top blue dots indicate the temperature data measured by the USB temperature probe. The bottom red dots show the reference signal over the same period. Their agreement shows that the room temperature fluctuation was the main reason for reference ring signal fluctuation. From [17]*

4.2 Optical Experimental Setup and Methods

The experimental setup details are discussed in this section. The details include the light coupling method, data acquisition and processing, liquid sample pumping system, ring resonator calibration, and chip coating.

4.2.1 Coupling Laser Light into/out of the Waveguides

In this research, the laser light was coupled into and out of the chip using the "edge-on coupling" method. Other research groups used devices that were equipped with surface relief gratings which permit facile coupling of the light into the bus waveguide. In these experiments, this method was not easily used because the surface coatings would cover the relief gratings. Coated gratings were not necessarily able to fulfill their function. In the present experiments, the light was coupled into the chip from a conically tapered single-mode optical fibre and was coupled out of the chip using a multi-mode fibre (Figure 4-4). The focusing from the tapered fibre significantly reduced the mode mismatch in the coupling process. The disadvantage, however, was that the fibre and the waveguide end must be aligned perfectly. Even the slightest mismatch caused a large loss in signal intensity. As a result, high precision alignment stages (Newport ULTRAlign Model 561D, Newport PCR-3, Newport 561-VH) were used to adjust and maintain fibre and chip alignment, as shown in Figure 4-5. The alignment stage was built by Dr. John Saunders and Dr. Jack Barnes. *[17]*

Even equipped with high precision alignment stages, the signals were still sensitive to alignment stage instability and mechanical vibration. Manual adjustments were required every 5 – 20 minutes to maintain a decent alignment. The fibres and waveguide would have to be fused permanently through V-groove assemblies to eliminate the alignment issues.

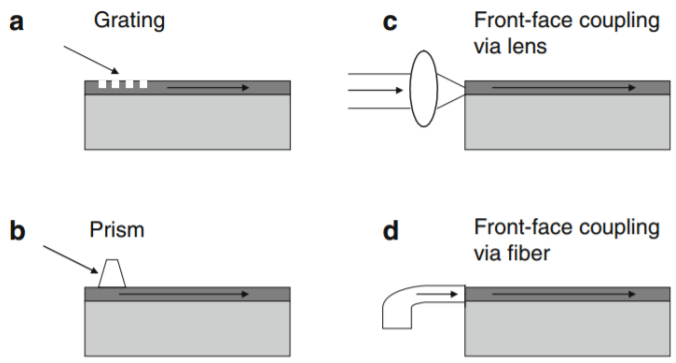

Figure 4-4 *Schematic of coupling methods to get light into photonic waveguides. (a) Grating coupling, (b) prism coupling, (c) front-face coupling via optical lens (d) front-face coupling via optical fibre. (From [50])*

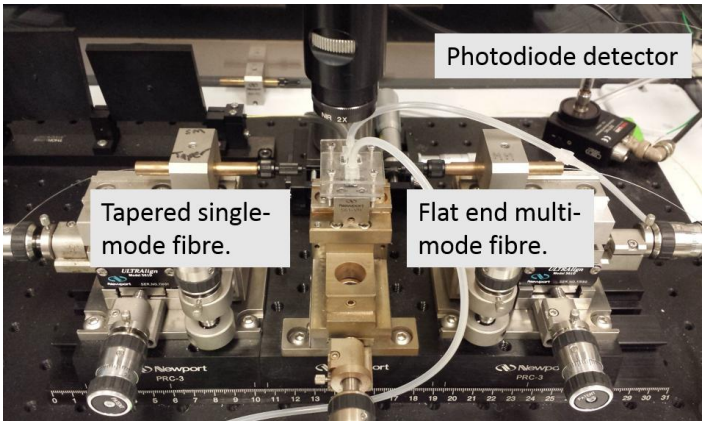

Figure 4-5 *Photo of the alignment stages with the fibers, microfluidics, tubes, and Photodiode detector. The SOI chip was packed in the microfluidics***.**

4.2.2 Optical Setup

Figure 4-6 shows the schematic of the experimental setup. Briefly, the instrument was constructed by using a tunable external cavity distributed feedback laser source (ANDO AQ4320D), with the power set to 0.5 to 1 mW and wavelength scan range of 1530 – 1570 nm. A fibre polarization controller constructed with three paddles was used to change laser polarization so that exclusively TM modes were coupled into the waveguide. While the polarization was not measured, it was apparent that the signal-to-noise ratio of the resonance peak increased when the polarization was well-controlled. A single-mode fibre (OZ Optics Ltd. Carp, ON, Canada) with convex tip was used to couple the light into chips. A multi-mode fibre (core

diameter = 100 µm, cladding diameter = 140 µm) with a flat facet end was used to couple the light out of the chips. Both the single mode fiber and the multi-mode fiber were mounted on 3-axis precision positioning stages (Newport, Franklin, MA, USA). A digital camera connected to a microscope (Optem Zoom 70XL 7:1 Micro-Inspection Lens System) was placed above the chip's alignment stage and was used to align the fibers and the waveguide ends. The multi-mode fibre was connected to a photodiode detector (Thor Lab DET10C InGaAs Biased Detector, 700 – 1800 nm), which was used to detect the light signals. The photodiode's output was sent to a lock-in amplifier (Stanford Research Systems, SR844). The lock-in amplifier also received reference signals at the modulation frequency and the laser ramp voltage from the tunable laser source. The signal intensity from the photodiode detector, the corresponding laser modulation frequency, and the laser ramp voltage signals were collected by an analog to digital converter (A/D) (PMD-1608FS, Measurement Computing, Norton, MA, USA), which sent the data to a computer. A LabVIEW program developed by Saunders et al. was used for data acquisition. [17] A setup scheme was shown in Figure 4-6.

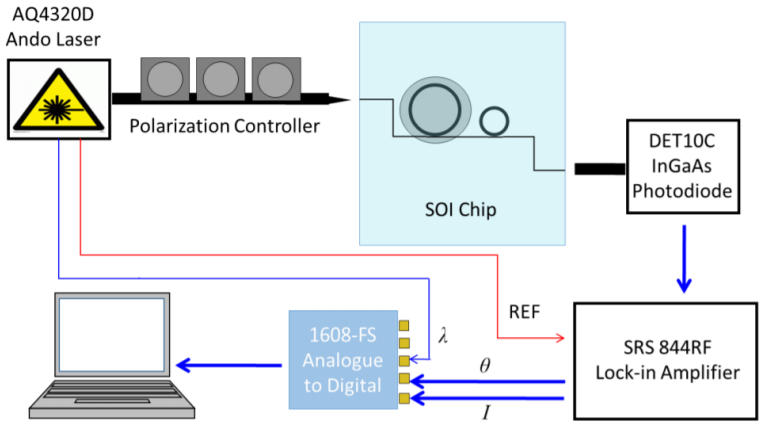

Figure 4-6 *Schematic of the experimental setup for SOI chip testing. A tunable external cavity diode laser (λ = 1520-1620 nm) was coupled to a fibre polarization controller to rotate the light to vertically polarized light to couple only TM modes into the SOI waveguides. A tapered single-mode optical fibre was used to couple into the SOI chip and a multi-mode optical fibre (100/140µm) collected the light leaving the chip, which was detected using an InGaAs photodetector. The signal was extracted using a lock-in amplifier and read by the computer using an A/D converter (From [17]).*

4.2.3 Experimental Parameter Setting

All the experimental parameters were set in the LabVIEW program, including laser power, wavelength scan range, and scan time. The laser power was set to 0.5 - 1 mW, a range in which the laser power was most stable. The wavelength scan was performed through a continuous ramp, as shown in Figure 4-7. The laser wavelength steadily increases until reaching the end point before jumping back to the starting wavelength, and the process starts again.

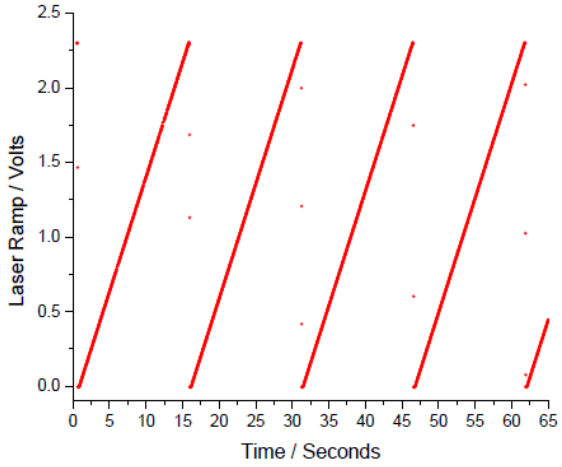

Figure 4-7 *Sample voltage ramp from the Ando laser in the continuous wavelength scan mode. The laser ramp ranges from 0 V to 2.3 V as a function of progress through the scan window. From [17]*

The data acquisition rate was determined by the wavelength scan range and the scan time.

$$Rate_{scan} = Range_{wavelength} / t_{scan} \tag{4.2}$$

The scan rate was chosen to be approximately 1 nm / 10 seconds. In most tests, the wavelength scan range was around 3 nm to include at least one sensing peak and one reference peak, and the scan time was therefore 30 seconds. As each scan can generate only one corrected resonance wavelength $\lambda_{sens,corr}$, the actual sample rate was one data point per 30 seconds. If the scan time were too long, the sample rate would not be enough to capture rapid peak shifts. The scan rate was also limited by the requirement to have a high spectral resolution. The effect of the scan time on transmission spectral resolution is shown in Figure 4-8.

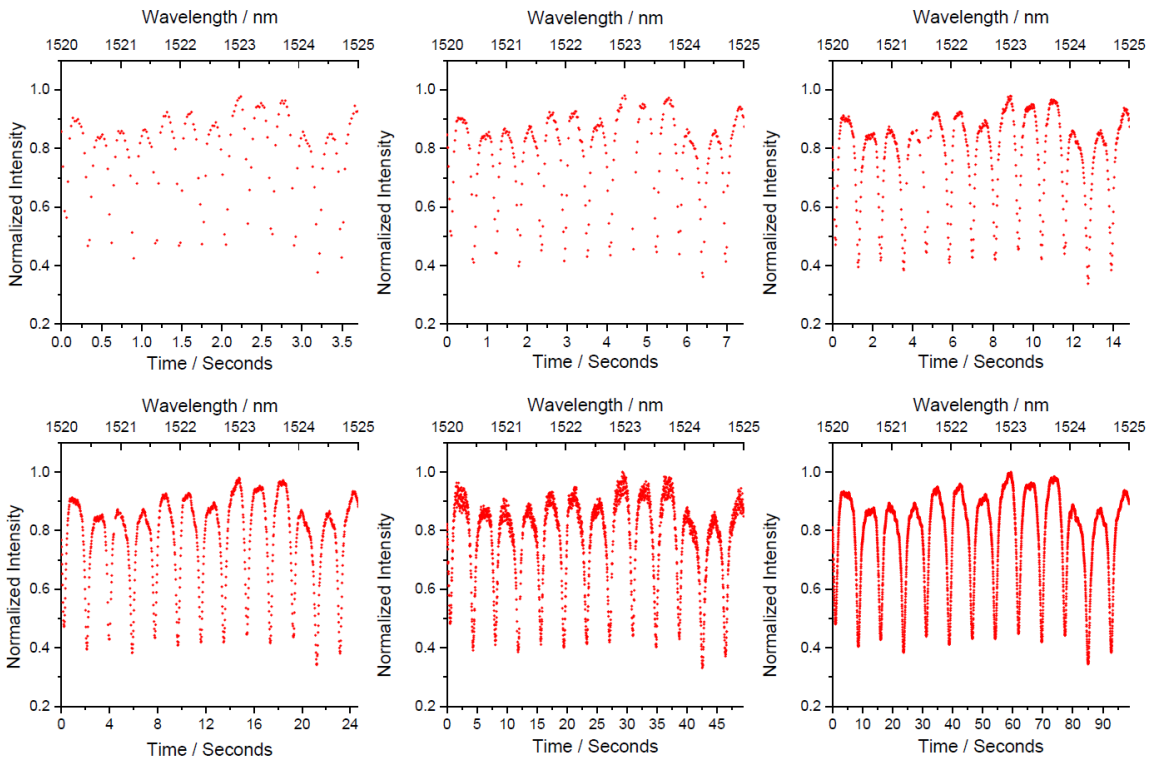

Figure 4-8 *Comparison of the spectral resolution as a function of laser scan rate over a fixed spectral window. The top row showed spectra when the laser was scanned at rates of 1.3 s/nm, 2.0 s/nm, and 4.0 s/nm. The bottom row shows spectra at rates of 6.7 s/nm, 13.3 s/nm, and 26.6 s/nm. The minimum resolution for accurate measurements depends on the full width at half maximum (FWHM) of the resonances. For the L = 1.27 mm ring resonator in this figure, the minimum laser scan rate was 3 s/nm, where each resonance was described by a minimum of 20 points. From [17]*

4.2.4 Data Storing and Processing

The experimental data were stored in a data file with four columns of data for each scan. The four columns of data were time (ms), ramp voltage (V), wavelength (nm), and signal intensity (V). During each scan, the signal intensity was graphed against wavelength and shown on the computer so that the tester knew that the alignment was good and the two peaks were in the scan range. In some tests, the sensing peaks shifted out of the scan ranges due to large refractive index changes. In that cases, the data acquisition was restarted to choose a larger scan range. After the experiments, the data was copied into Igor Pro™ 6, where the resonance peaks were fitted by Lorentzian lineshape functions. (Figure 4-9) Automation codes

in Igor Pro™ 6 were developed to process thousands of scanned data sets. The sensing peaks and reference peaks were fitted separately, and the resulting corrected wavelength was obtained using equation (4.1).

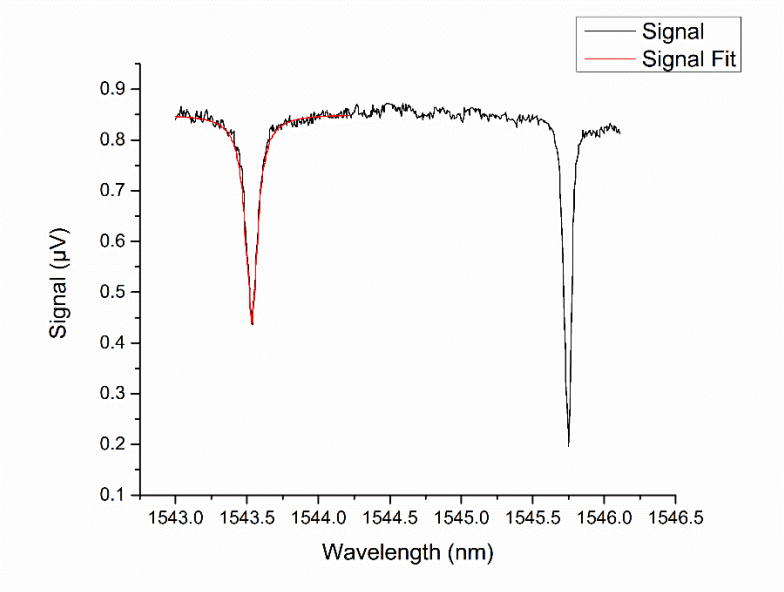

Figure 4-9 *A tandem ring spectrum and a Lorentzian function fit on the sensing peak.*

4.3 Microfluidic Device and Liquid Sample Pumping System

Microfluidic channels were made as that the solutions would steadily flow on the resonators without leakings. The channels were made of polydimethylsiloxane (PDMS) (SYLGARD® 184 Silicone Elastomer, Dow Corning Inc., Midland, MI, USA) by mold casting method. A SOI chip, a microfluidics channel, and two tube connectors were sandwiched between two plastic shells which were fastened by four screws, as shown in Figure 4-10. Aqueous samples were sucked into the channel from a solution reservoir using negative pressure generated by a syringe pump. Pressure driven flow method was also attempted but was not used due to excessive leakage.

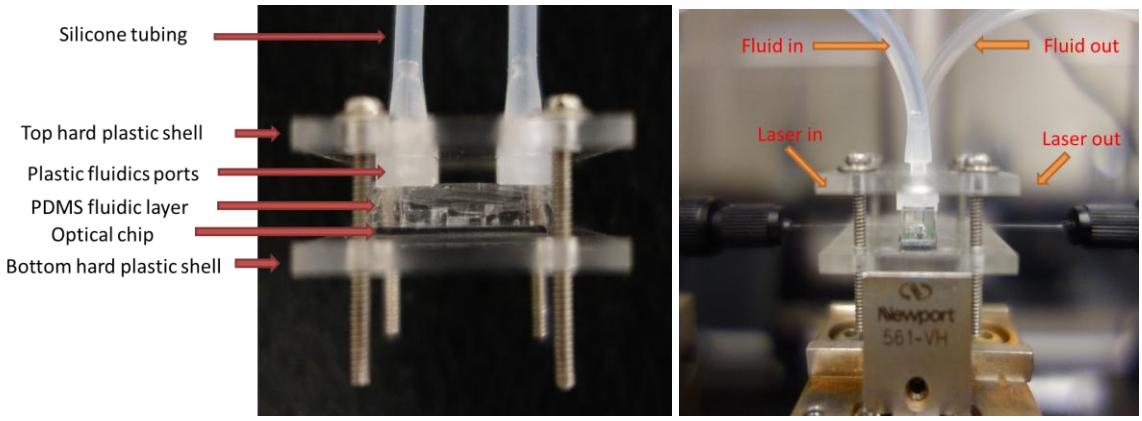

Figure 4-10 *The microfluidic device with the chip and the optical alignment. (Left) The side view shows the SOI chip was between the PDMS fluidic layer (channel) and bottom plastic shell. (Right) The front view shows the microfluidics, fibres, and tubing.*

4.4 Ring Resonators Calibration

The relationship between resonance peak shift and cladding reflective index change for a ring resonator was determined by calibration with solutions having known refractive indices. In this research, 6 sucrose-water solutions with concentrations from 0.5% to 3.0% w/w were used. Figure 4-11 shows one calibration example. In this case, the scan wavelength range was 1544 – 1556 nm and the scan time was 30 seconds. The flow of the solutions follows a pattern, i.e. 5 minutes water flow followed by 5 minutes of sucrose solution. The peak wavelengths were obtained from the fits were temperature-corrected and graphed in Figure 4-11(c). They fell in a straight line as expected and gave the sensitivity as $d\lambda_{sens,corr}/dn$ = 100.8(9) nm/RIU nm/RIU. The minimal detectable index change in this experiment was δn =0.0003 RIU (the average vertical width of the region between the dotted blue lines), which was calculated from a spreadsheet obtained from Loock and Wentzell [51].

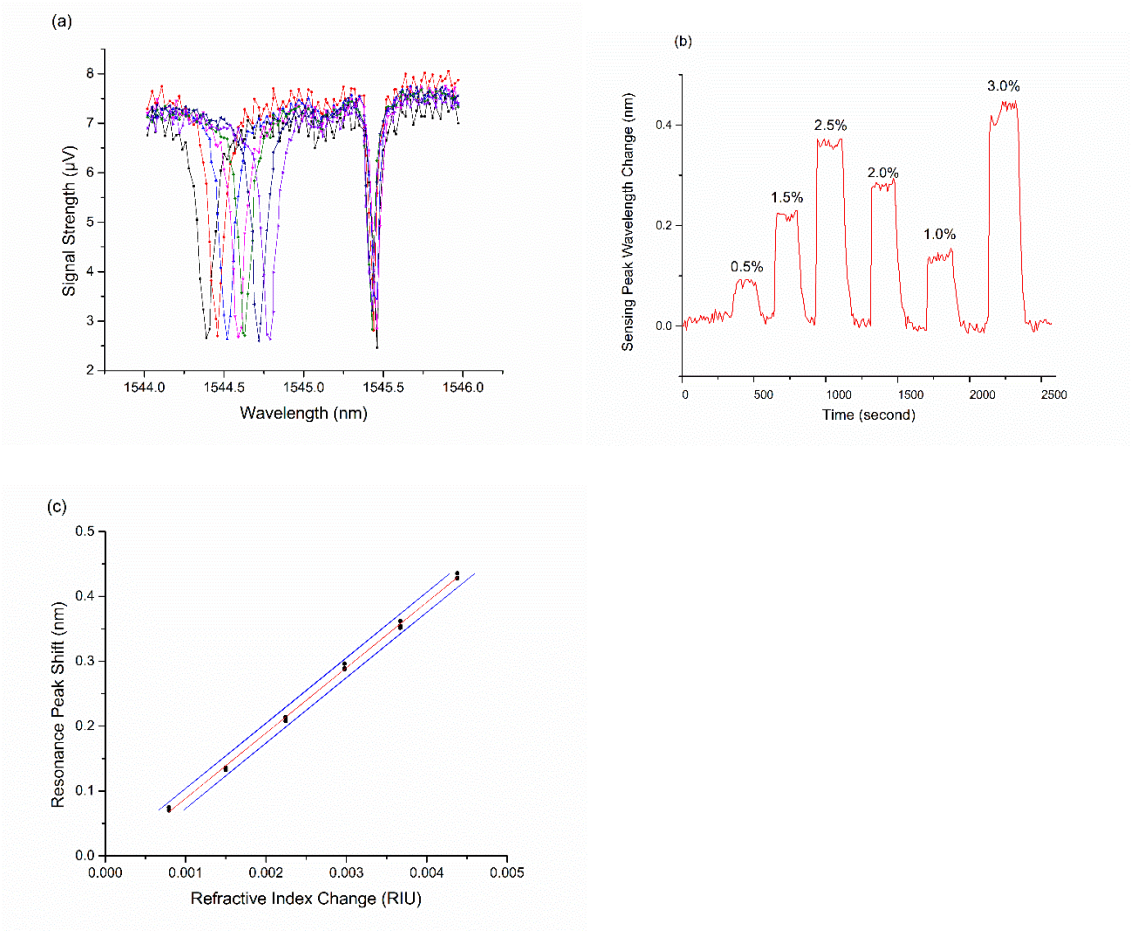

Figure 4-11 *Tandem ring resonator calibration. (a) Transmission spectrum between 1544 – 1546 nm shows one pair of sensing peak and reference peak at different concentration (w/w = 0%, 0.5%, 1.0%, 1.5%, 2.0%, 2.5%, 3.0%). The sensing peaks (peaks on the left) shifted when exposed to different concentration of sucrose solution and when the temperature changes. The reference peak (peaks on the right) only change positions when the temperature changes. (b) The wavelength shift of the sensing peak after temperature correction. (c) A linear fit to the sucrose calibration for the tandem ring resonators. The red line shows the linear fit of the refractive index change and resonance peak shift correlation. The two blue lines show +/- 95% confidence intervals of the fit. Sensitivity = 100.8(9) nm/RIU. Resolution limit = 0.00017 RIU, which is the width of the confident interval (the horizontal distance of the two blue line).*

4.5 Mesoporous Silica Coating

The mesoporous silica coating was synthesized according to the process used by Du *et al.* [15]. 1.98 g (9.5 mmol) of tetraethoxysilane (TEOS) and 0.256 g (0.475 mmol) of bis-[3-(triethoxysilyl)-propyl]-tetrasulfide (SIS) were dissolved in 3 ml of anhydrous ethanol. 1.2 ml of DI water and 0.16 ml of 6 M HCl

were added to the solution, and it was stirred at 60 ℃ for 2 hours. 0.719 g of Pluronic F127 was dissolved in 16 ml of anhydrous ethanol in another vial and was stirred at room temperature for 2 hours. The second solution was added to the first one drop at a time, and the resultant mixture was stirred for another 2 hours. The silica-covered SOI chips were cleaned first, by rinsing with isopropanol followed by exposure to an air plasma. The precursor solution was then spin-coated on the chips at 3000 rpm for 30 seconds. The thicknesses of the resulting films were around 400 nm. To avoid cracking of the films and to maintain constant conditions, the spin-coated films were kept at 42% relative humidity for 12 hours and dried in a vacuum oven at 65 ℃ for 2 hours. The Pluronic F127 surfactant was removed by refluxing in acetone for 16 hours. The films were then dried in a vacuum oven for 2 hours.

4.6 Water Flow Baseline Drift

The mesoporous silica coated chips were kept in a plastic petri dish with lid in a dark and dry cupboard. When the chip was used to sense analytes in flowing aqueous solutions, the sensing peaks shifted continually towards lower wavelengths. The baseline drift was tested with flow rates of 0.9 ml/min and 0 ml/min (stationary water), twice for each flow rate. The test results are shown in Figure 4-12. When the flow rate was 0.9 ml/min, the peak shifting rates were -1.49(1) $\times 10^{-8}$ RIU/second and -1.349(7)$\times 10^{-8}$ RIU/second. When the flow rate was 0, the peak shifting rates were -3.96(5) $\times 10^{-9}$ RIU/second and 1.5(1) $\times 10^{-9}$ RIU/second. This proved that in stationary water, the baseline drifted up or down by a very small amount, but was almost unchanged compared to the baseline with the flow rate at 0.9 ml/min. The baseline drift at 0.9 ml/min water flow was fairly constant, which might be due to the erosion of the coating in flowing solution, a process by which the debris were constantly washed away by the water flow. As all the adsorption and desorption tests were carried out at a flow rate of 0.9 ml/min, the baseline drift must be considered to determine the real refractive index change due to metal ion adsorption and desorption. The sloping baseline should be subtracted from the sensing signals to compensate for this slow drift.

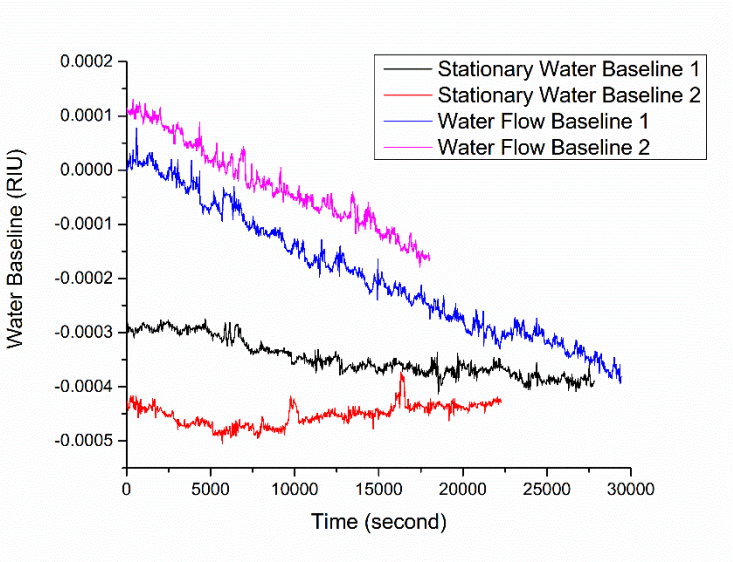

Figure 4-12 *Temperature-corrected sensing peak baselines at 0.9 ml/min and 0 ml/min flow rate of DI water.*

Chapter 5

Sensing of Lead, Pb(II), and Mercury, Hg(II)

This chapter discusses Pb(II) and Hg(II) adsorption and desorption measurements on tetrasulfide mesoporous silica (S_4-PMS) functionalized SOI ring resonators with DI water, tap water, and seawater solutions, as well as tetraethyl orthosilicate mesoporous silica (PMS) functionalized SOI ring resonators test with DI water solutions. Sections 5.1 - 5.3 discuss the Pb(II) ion tests with DI water, tap water, and seawater. Section 5.4 discusses the Hg(II) ion tests with DI water. Section 5.5 discusses X-ray photoelectron spectroscopy (XPS) measurements on film with adsorbed Pb(II) and Hg(II) ions.

The adsorption processes were fitted to either equation (5.1), derived from equation (3.11)

$$\begin{aligned} [MY](t) &= \frac{k_a'[Y]_0}{(k_a'+k_d)}\left[1-\exp\left(-(k_a'+k_d)t\right)\right] \\ q(t) &= q_e\left[1-\exp\left(-\frac{t}{\tau}\right)\right] \end{aligned} \tag{5.1}$$

, where $[MY](t) = q(t)$, $\frac{k_a'[Y]_0}{(k_a'+k_d)} = q_e$, and $k_a'+k_d = \frac{1}{\tau}$. The second equation is the built-in fitting equation in Igor Pro™.

For two binding-site adsorption, equation (5.2) can be derived from equation (3.18)

$$\begin{aligned} ([MX]+[MY])(t) &= \frac{k_{a,X}'[X]_0}{(k_{a,X}'+k_{d,X})}\left[1-\exp\left(-(k_{a,X}'+k_{d,X})t\right)\right] \\ &\quad + \frac{k_{a,Y}'[Y]_0}{(k_{a,Y}'+k_{d,Y})}\left[1-\exp\left(-(k_{a,Y}'+k_{d,Y})t\right)\right] \\ q(t) &= q_{e,X}\left[1-\exp\left(-\frac{t}{\tau_{a,X}}\right)\right] + q_{e,Y}\left[1-\exp\left(-\frac{t}{\tau_{a,Y}}\right)\right] \end{aligned} \tag{5.2}$$

where $\left(\left[MX\right]+\left[MY\right]\right)\left(t\right)=q(t)$, $\frac{k_{a,X}'\left[X\right]_0}{\left(k_{a,X}'+k_{d,X}\right)}=q_{e,X}$, $\frac{k_{a,Y}'\left[Y\right]_0}{\left(k_{a,Y}'+k_{d,Y}\right)}=q_{e,Y}$, $k_{a,X}'+k_{d,X}=\frac{1}{\tau_{a,X}}$, and $k_{a,Y}'+k_{d,Y}=\frac{1}{\tau_{a,Y}}$. The second equation is the built-in fitting equation in Igor Pro™.

The desorption processes were fitted to either equation (5.3), derived from equation (3.15)

$$\begin{aligned}\left[MY\right]\left(t\right)&=\left[MY\right]_0\left[\exp\left(-k_d t\right)\right]\\ q\left(t\right)&=q_0\left[\exp\left(-\frac{t}{\tau_d}\right)\right]\end{aligned}\tag{5.3}$$

where $\left[MY\right]\left(t\right)=q(t)$, $[MY]_0=q_0$, and $k_d=\frac{1}{\tau_d}$. The second equation is the built-in fitting equation in Igor Pro™.

For two binding-site desorption, equation (5.4), derived from equation (3.19)

$$\begin{aligned}\left(\left[MX\right]+\left[MY\right]\right)\left(t\right)&=\left[MX\right]_0\exp\left(-k_{d,X}t\right)+\left[MY\right]_0\exp\left(-k_{d,Y}t\right)\\ q\left(t\right)&=q_{0,X}\left[\exp\left(-\frac{t}{\tau_{d,X}}\right)\right]+q_{0,Y}\left[\exp\left(-\frac{t}{\tau_{d,Y}}\right)\right]\end{aligned}\tag{5.4}$$

where $\left(\left[MX\right]+\left[MY\right]\right)\left(t\right)=q(t)$, $[MX]_0=q_{0,X}$, $[MY]_0=q_{0,Y}$, $k_{d,X}=\frac{1}{\tau_{d,X}}$, and $k_{d,Y}=\frac{1}{\tau_{d,Y}}$. The second equation is the built-in fitting equation in Igor Pro™.

5.1 Pb(II) Ion Adsorption and Desorption Tests in DI Water

5.1.1 Adsorption and Desorption Tests on S_4-PMS Coating

The adsorption and desorption of Pb(II) in and out of an S_4-PMS coating were recorded by scanning the resonator transmission spectra at a scan interval of 30 s. As a result, the data acquisition rate was one data point per 30 seconds. The adsorption process was monitored for 3 hours, and the DI water desorption process was monitored for 6 hours. The experiment was completed by flushing the chip with 1 ppm (ppm

defined as mg/L) aqueous Na_2EDTA solution for 1 hour to remove the remaining metal ions and restore the coating. As shown in Figure 5-1, the coating's refractive index increased bi-exponentially during the adsorption process and decreased bi-exponentially in the water desorption process. The quality of the fit residuals increased dramatically when changing from a one-site binding model to a two-site binding model.

The fit parameters are shown in Table 5-1. The loading values with different units were calculated based on Table 3-1. It was apparent from the fit residuals that the double exponential functions fitted the adsorption and desorption process better. It was also clear from the fitting parameters that the fast adsorption process with τ_X = 300 s led to a strongly bound lead ion that took a long time (τ_X = 18000 s) to remove. Some of this tightly bound lead could only be removed using EDTA as a chelating agent. The loosely bound lead took a longer time to bind to the film (τ_Y = 4650 s) but was readily removed (τ_Y = 2150 s). This suggestes that the two binding sites in the coating have different affinities for Pb(II). Note that the $q_{0,Y}$ term in Na_2EDTA desorption was nearly zero with very large relative error, suggesting a single exponential decay process. That was probably because the loosely bound Pb(II) was mostly removed and EDTA removed Pb^{2+} ions only from the tightly bound site after 6 hours of DI water desorption.

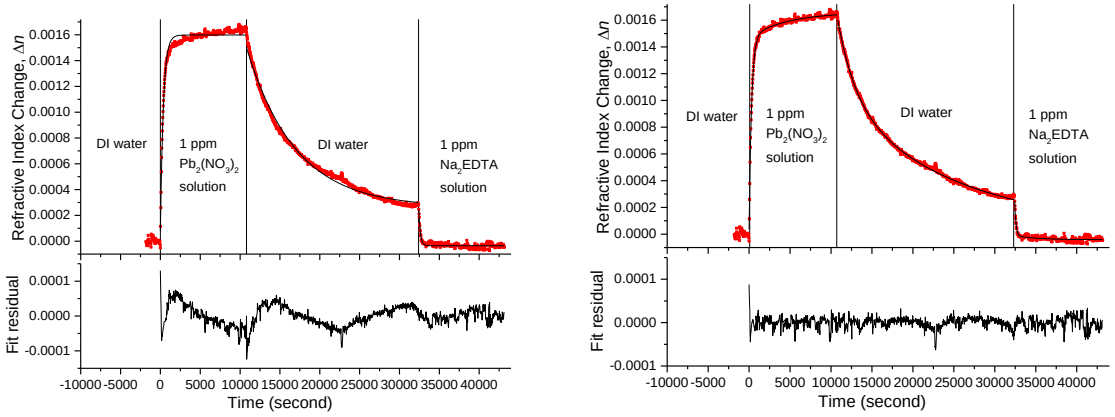

Figure 5-1 *Comparison between single and double exponential functions fits of 1 ppm Pb(II) ion DI water solution adsorption and desorption on the S_4-PMS coating. (Left) Single exponential functions fit with fit residual plotted on the bottom. The fit was poor. (Right) Double exponential functions fit with fit residual plotted on the bottom. This fit was much better than the single exponential functions fit.*

Table 5-1 Fitting parameters for single exponential functions (5.1) and (5.3), and double exponential equations (5.2) and (5.4) to describe the Pb(II) ion adsorption and desorption on the S_4-PMS coating of Figure 5-1. The decay time τ is given in seconds, and the loadings are given in values in three different units, calculated based on Table 3-1.

Single site model				
Parameter	**Unit**	**Adsorption**	**Desorption**	**Na_2EDTA rinse**
q_e or q_0	***RIU***	0.00152 (2)	0.00123(4)	0.00033(1)
	mol(Pb)/mol(film)	0.00195(2)	0.00159(5)	0.00042(1)
	g(Pb)/g(wet film)	0.0103(2)	0.00837(3)	0.00220(1)
	g(Pb)/g(dry film)	0.0135(1)	0.0110(4)	0.00288(1)
τ	**s**	375(7)	6130(60)	197(9)
Double site model				
Parameter	**Unit**	**Adsorption**	**Desorption**	**Na_2EDTA rinse**
$q_{e,X}$ or $q_{0,X}$	***RIU***	0.00143(7)	0.000979(6)	0.00031(1)
	mol(Pb)/mol(film)	0.00182(9)	0.00126(8)	0.00040(1)
	g(Pb)/g(wet film)	0.00969(5)	0.00662(4)	0.00212(7)
	g(Pb)/g(dry film)	0.0127(7)	0.00866(5)	0.00277(9)
τ_X or τ_X	**s**	301(3)	18000(600)	170(10)
$q_{e,Y}$ or $q_{0,Y}$	***RIU***	0.00019(3)	0.00059(2)	0.00003(5)
	mol(Pb)/mol(film)	0.000243(4)	0.000752(2)	0.00004(6)
	g(Pb)/g(wet film)	0.00128(2)	0.00396(1)	0.0002(3)
	(g(Pb)/g(dry film)	0.00168(3)	0.00519(1)	0.0003(4)
τ_Y or τ_Y	**(s)**	4650(40)	2150(70)	2610(40)

5.1.2 Adsorption and Desorption Tests on PMS Coating

The adsorption and desorption of Pb(II) of a PMS coating were recorded with the same data acquisition rate as in the S_4-PMS tests (30 seconds per data point). The adsorption was monitored for 3

hours, the DI water desorption process was also monitored for 3 hours, and the desorption process using 1 ppm Na_2EDTA solution was recorded for 2 hours.

The fit curves are shown in Figure 5-2 and the fit parameters are summarized in Table 5-2. The loading values with different units were calculated based on Table 3-1. It was clear from the fit residuals that the data can be fitted to single exponential functions with good agreement. This suggested that only one binding site was in the PMS coating.

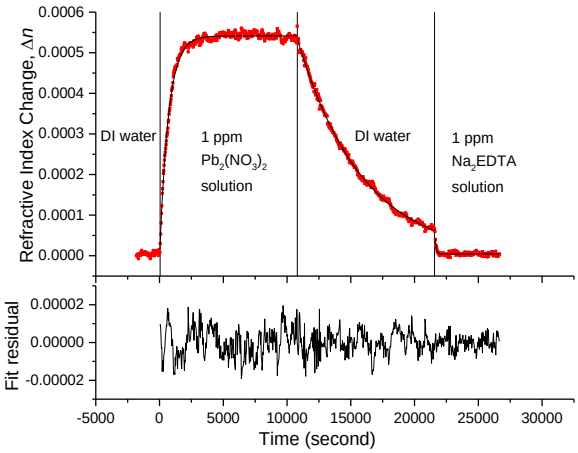

Figure 5-2 *Single exponential function fit to the 1 ppm Pb(II) adsorption and desorption processes of the PMS coating with fit residual plotted on the bottom.*

Table 5-2 Fitting parameters for single exponential functions (5.1) and (5.3) to describe the Pb(II) ion adsorption and desorption on the PMS coating of the figure above. The decay times τ were given in seconds, and the loadings q_e and q_0 were given in values in three different units, calculated based on Table 3-1.

Parameters	Units	Adsorption	Desorption	Na_2EDTA rinse
q_e or q_0	***RIU***	0.000548(3)	0.000537(2)	0.000053(3)
	mol(Pb)/mol(film)	0.000702(4)	0.000689(2)	0.000068(4)
	g(Pb)/g(wet film)	0.00370(3)	0.00363(1)	0.00036(2)
	g(Pb)/g(dry film)	0.00485(2)	0.00475(2)	0.00047(3)
τ	***s***	687(6)	5060(50)	86(9)

While the adsorption rate was slower compared to the fast uptake rate observed with the S_4-PMS coating, it was also much faster than the rate observed with the S_4-PMS film. Similarly, the desorption rate

fell between the fast and slow desorption rates observed for the S_4-PMS film. Therefore, it appeared as if the Pb(II) ions have an affinity for the PMS film that fell between the two distinct binding sites of the S_4-PMS film.

5.1.3 Test on Uncoated Chip

Before the chip was coated with S_4-PMS and PMS coatings, it was exposed to lead ions in aqueous solution by flowing DI water and 1 ppm Pb(II) solutions across the microphotonic devices. No observable refractive index change could be found in the data. The test results are shown in Figure 5-3. This suggested that 1 ppm Pb(II) solutions by themselves did not shift the resonance peaks. At 1550 nm and 20.0 ℃, the refractive index difference between water and 1 ppm $Pb(NO_3)_2$ was 2×10^{-6} RIU, which was below the detection limit of our ring resonators. This confirms that the adsorption of metal ions into the mesoporous silica coating was the reason for peak shifts.

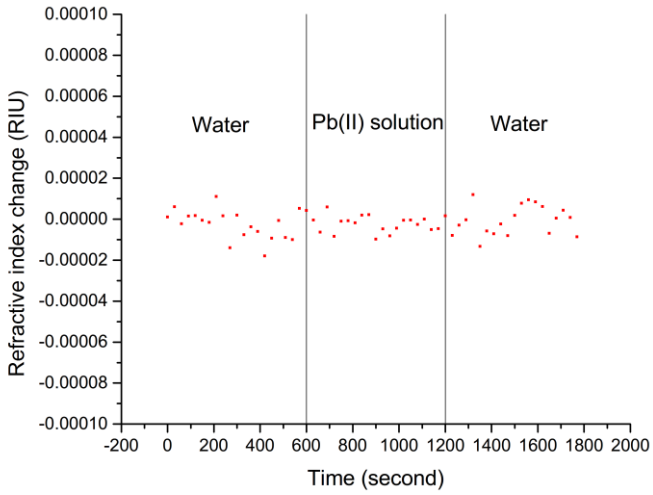

Figure 5-3 *Uncoated chip shows no refractive index change between water and Pb(II) solution.*

5.1.4 Adsorption and Desorption at Different Pb(II) Ion Concentrations

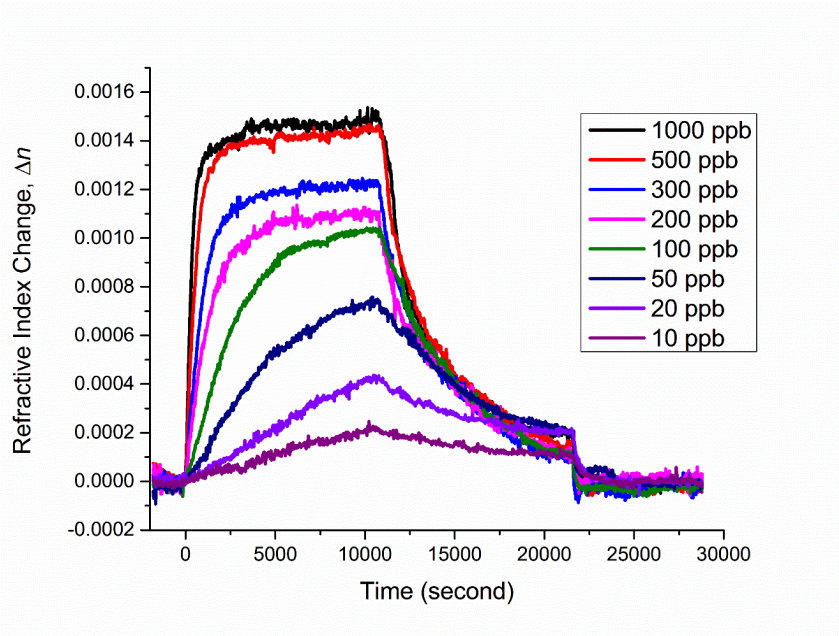

Figure 5-4 *Adsorption-desorption curve when the resonators were exposed to a series of Pb(II) solutions with concentrations of 1000 ppb, 500 ppb, 300 ppb, 200 ppb, 100 ppb, 50 ppb, 20 ppb, and 10 ppb.*

The adsorption-desorption curve for a series of Pb(II) ion solution samples (1000 ppb, 500 ppb, 300 ppb, 200 ppb, 100 ppb, 50 ppb, 20 ppb, and 10 ppb, ppb is defined as ng/mL) are shown in Figure 5-4. Each of these adsorption tests lasted 3 hours. The water desorption tests lasted 3 hours, and the Na_2EDTA solution desorption tests lasted 2-3 hours. Note that the 1 ppm Pb(II) solution data shown in Figure 5-4 and Table 5-3 are slightly different from those shown in Figure 5-1 and Table 5-1 although they were from the tests on the same film on the same chip. Those two tests were performed apart by five months. The resonator's response was slightly different as a result of many possible factors, including film aging and erosion from aqueous sample flows, and different PDMS channel positions.

Although the adsorption-desorption curves for high concentration Pb(II) solutions (1 ppm – 200 ppb) could be fitted well with double exponential equations, the curves for low concentration (100 ppb – 10 ppb) fitted better with single exponential equations. The most plausible explanation was that the strong

binding site would bind the Pb ions first before the weak binding sites started to be occupied. These curves and their fits are shown in Figure 5-5 to Figure 5-12, and the fit parameters are summarized in Table 5-3 to Table 5-10.

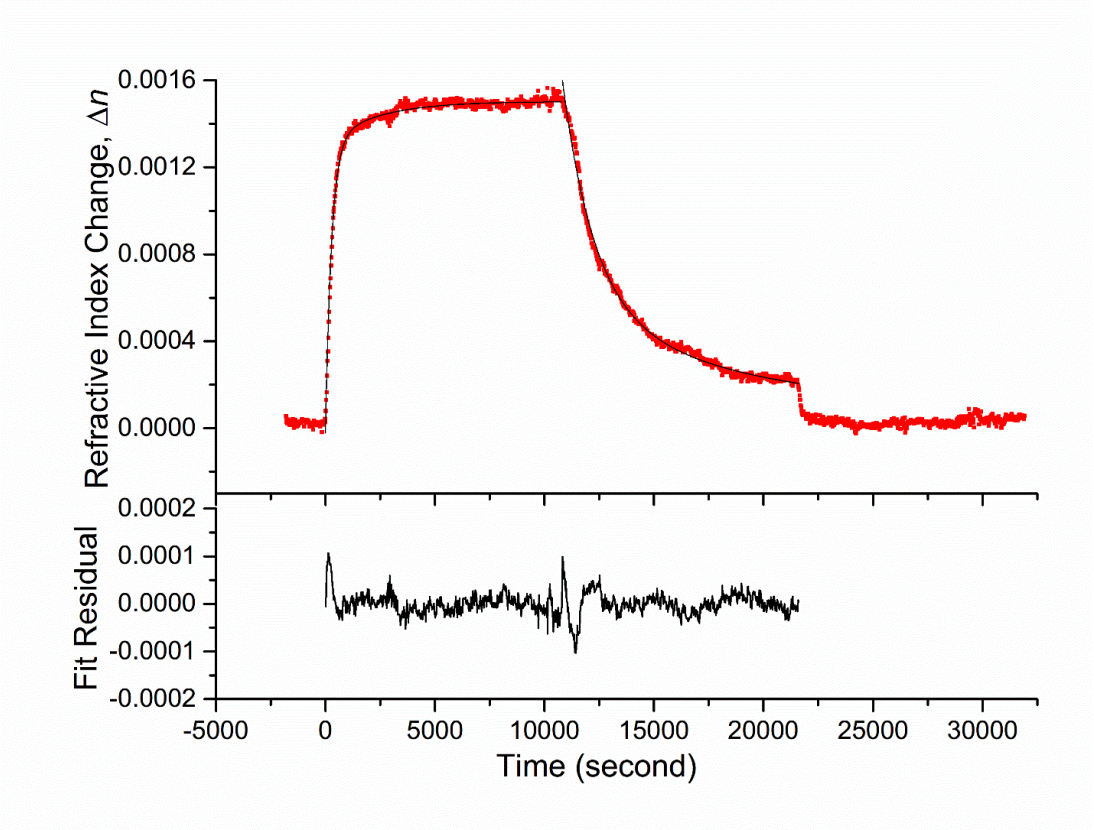

Figure 5-5 *Double exponential function fits of 1 ppm Pb(II) ion adsorption and desorption processes on the S_4-PMS coating, with fit residual shown below.*

Table 5-3 Fitting parameters for double exponential function (5.2) and (5.4) fits of the 1 ppm Pb(II) ion adsorption and desorption on the S_4-PMS coating of the figure above.

	Adsorption	**Desorption**
$q_{e,X}$ **or** $q_{0,X}$ ***(RIU)***	0.00139(1)	0.0005(1)
τ_X **or** τ_X **(s)**	238(5)	5300(100)
$q_{e,Y}$ **or** $q_{0,Y}$ ***(RIU)***	0.00019(1)	0.00092(5)
τ_Y **or** τ_Y **(s)**	2260(20)	1300(100)

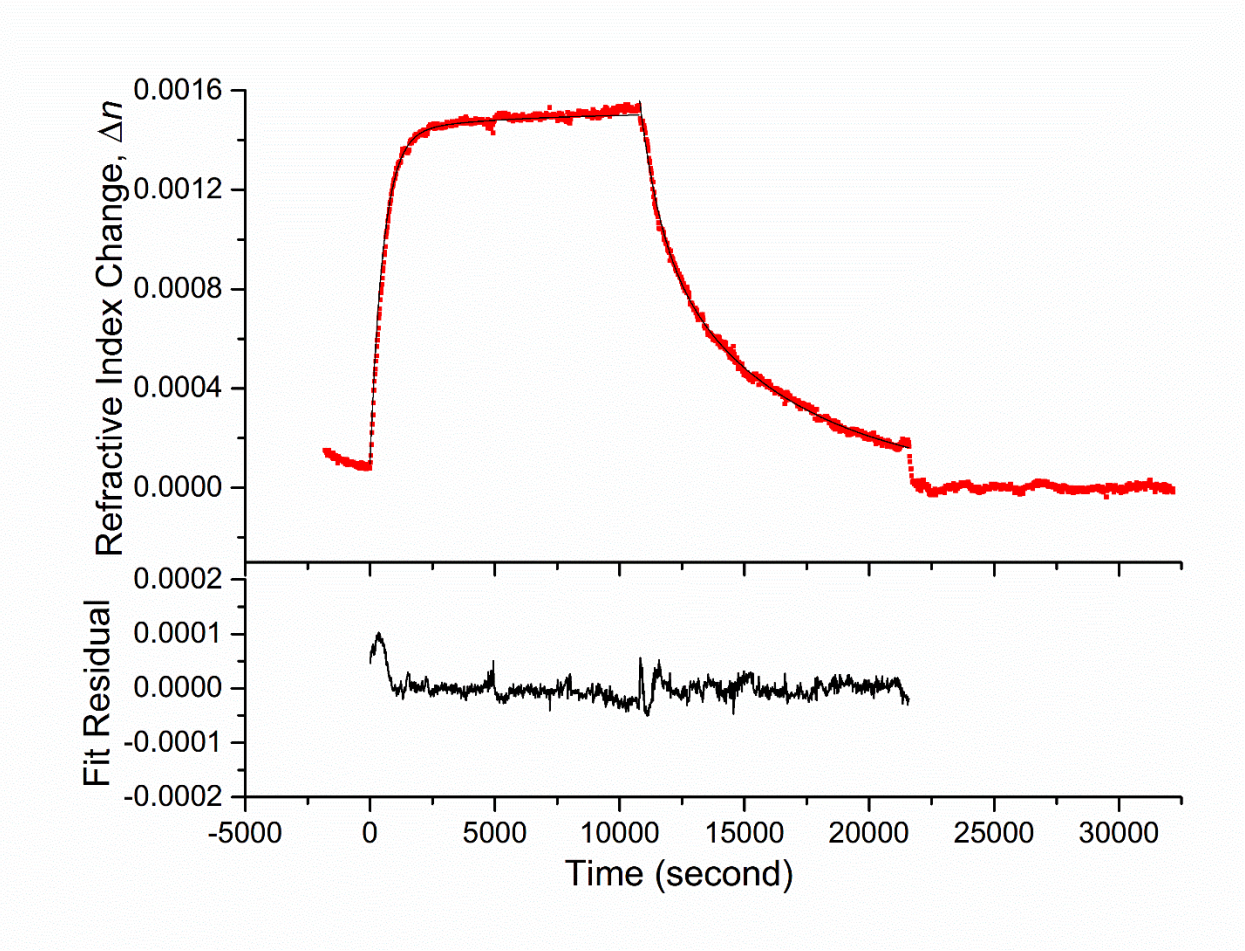

Figure 5-6 *Double exponential function fits of 500 ppb Pb(II) ion adsorption and desorption processes on the S_4-PMS coating, with fit residual shown below.*

Table 5-4 Fitting parameters for double exponential function (5.2) and (5.4) fits of the 500 ppb Pb(II) ion adsorption and desorption on the S_4-PMS coating of the figure above.

	Adsorption	**Desorption**
$q_{e,X}$ **or** $q_{0,X}$ **(RIU)**	0.00133(2)	0.00097 (2)
τ_X **or** τ_X **(s)**	515 (8)	5710(40)
$q_{e,Y}$ **or** $q_{0,Y}$ **(RIU)**	0.00009(1)	0.000584(9)
τ_Y **or** τ_Y **(s)**	1920(40)	900(300)

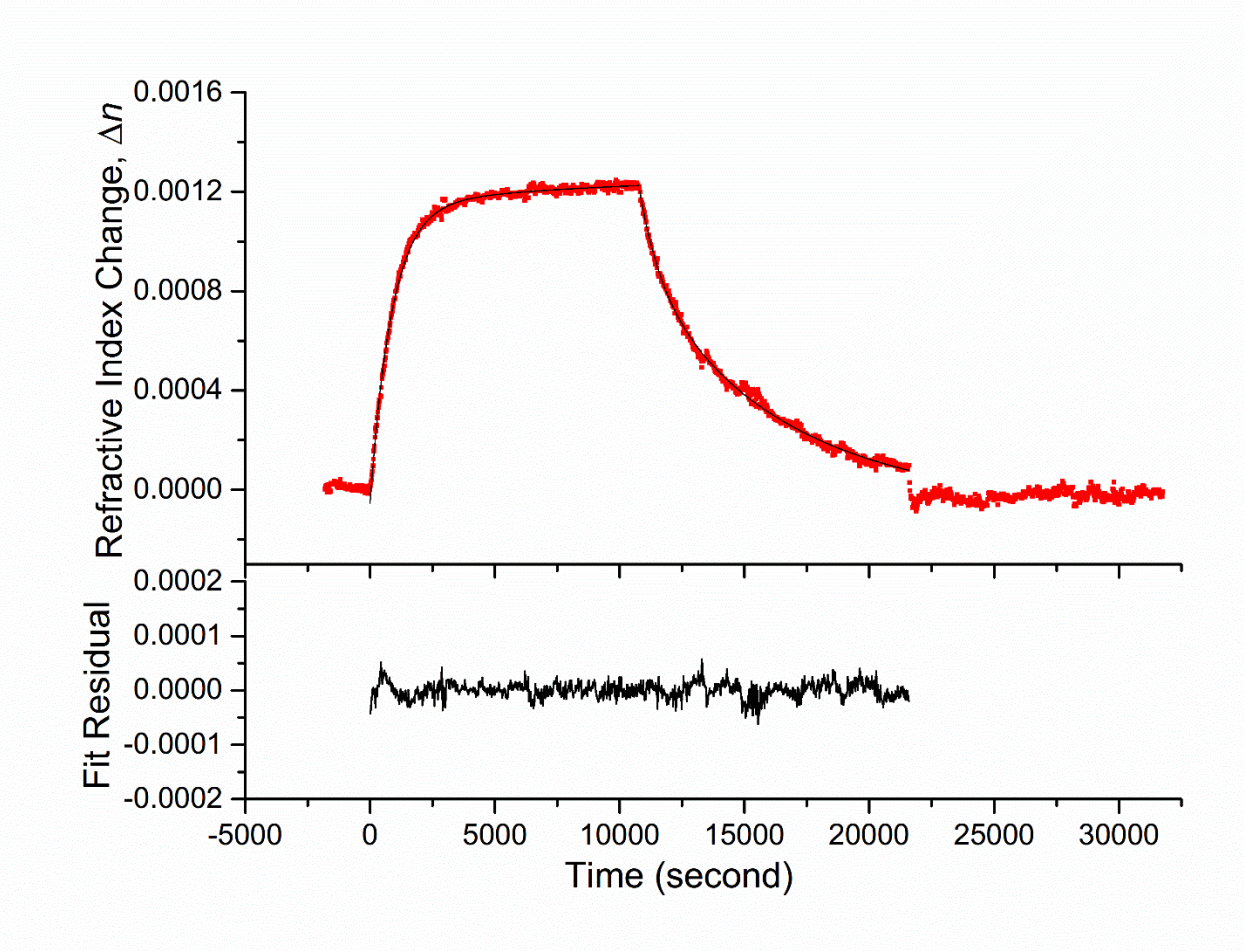

Figure 5-7 *Double exponential function fits of 300 ppb Pb(II) ion adsorption and desorption processes on the S_4-PMS coating, with fit residual shown below.*

Table 5-5 Fitting parameters for double exponential function (5.2) and (5.4) fits of the 300 ppb Pb(II) ion adsorption and desorption on the S_4-PMS coating of the figure above.

	Adsorption	**Desorption**
$q_{e,X}$ **or** $q_{0,X}$ **(RIU)**	0.00119(1)	0.000922(9)
τ_X **or** τ_X **(s)**	870(10)	5700(300)
$q_{e,Y}$ **or** $q_{0,Y}$ **(RIU)**	0.00014(2)	0.00034(2)
τ_Y **or** τ_Y **(s)**	9600(200)	820(60)

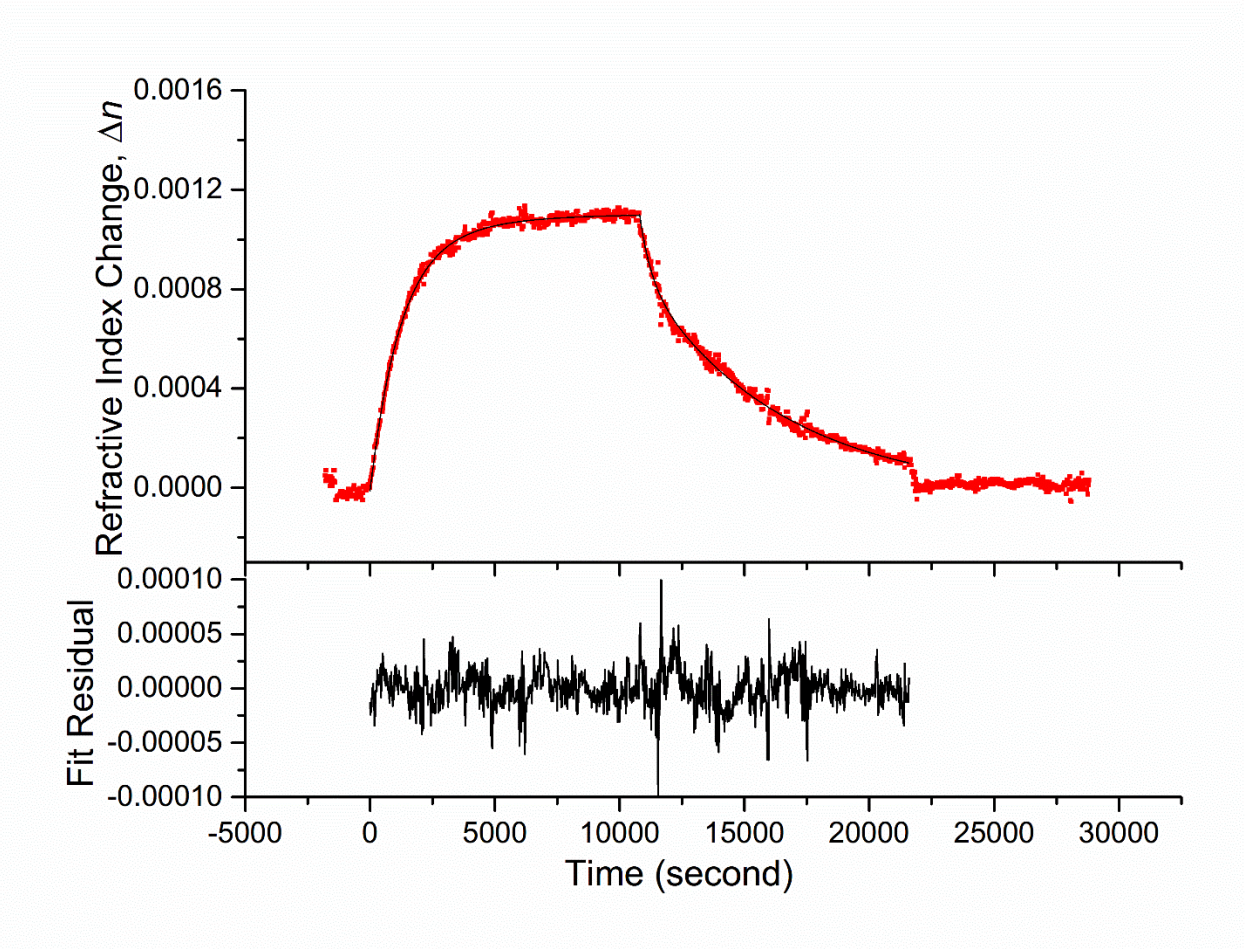

Figure 5-8 *Double exponential function fits of 200 ppb Pb(II) ion adsorption and desorption processes on the S_4-PMS coating, with fit residual shown below.*

Table 5-6 Fitting parameters for double exponential function (5.2) and (5.4) fits of the 200 ppb Pb(II) ion adsorption and desorption on the S_4-PMS coating of the figure above.

	Adsorption	**Desorption**
$q_{e,X}$ **or** $q_{0,X}$ ***(RIU)***	0.0009(1)	0.000888(5)
τ_X **or** τ_X **(s)**	1180(70)	5600(200)
$q_{e,Y}$ **or** $q_{0,Y}$ ***(RIU)***	0.00017(8)	0.00024(1)
τ_Y **or** τ_Y **(s)**	3000(500)	400 (40)

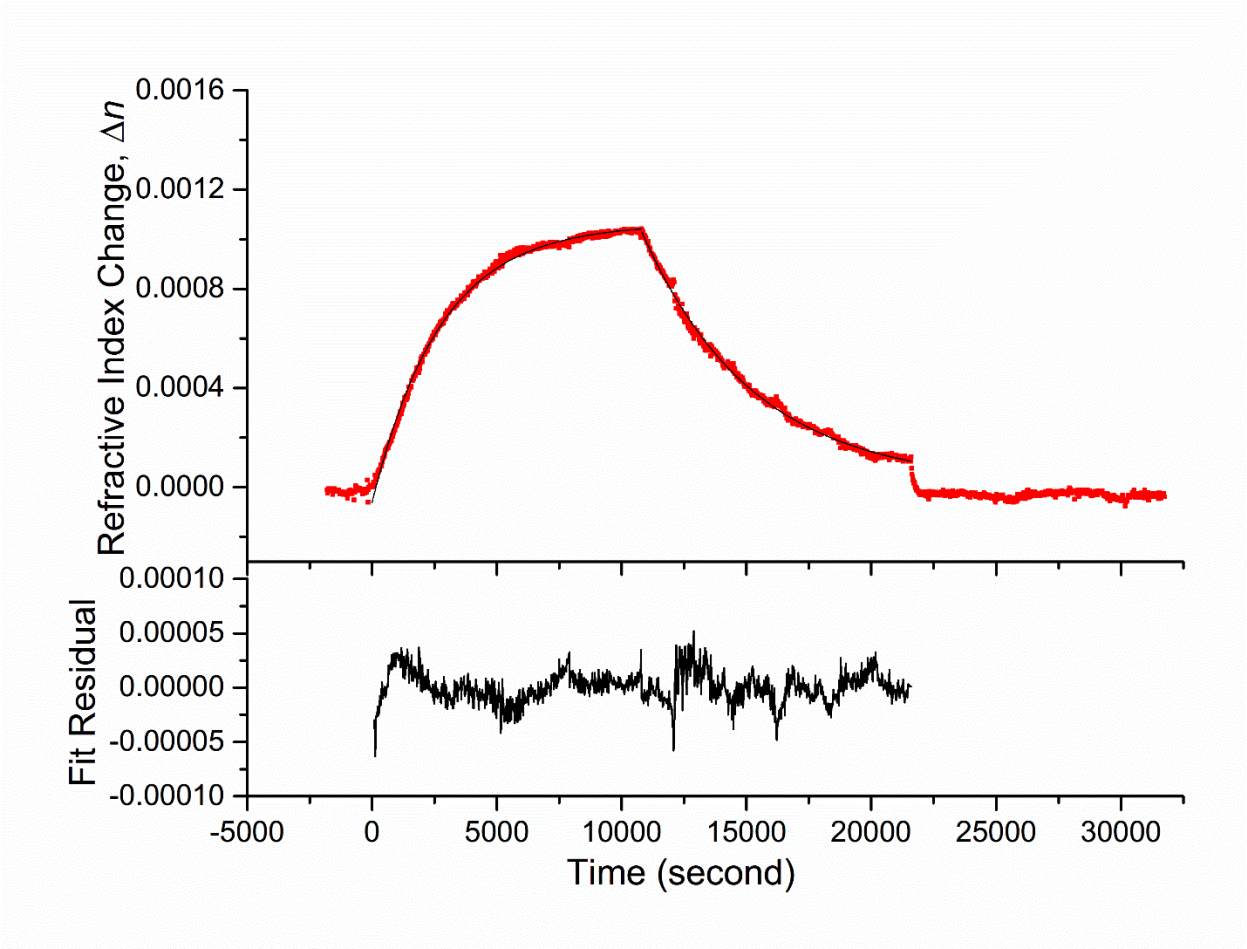

Figure 5-9 *Single exponential function fits of 100 ppb Pb(II) ion adsorption and desorption processes on the S_4-PMS coating, with fit residual shown below.*

Table 5-7 Fitting parameters for single exponential function (5.1) and (5.3) fits of the 100 ppb Pb(II) ion adsorption and desorption on the S_4-PMS coating of the figure above.

	Adsorption	**Desorption**
$q_{e,X}$ **or** $q_{0,X}$ ***(RIU)***	0.00107(2)	0.001016 (3)
τ_X **or** τ_X **(s)**	2660(20)	4440(40)

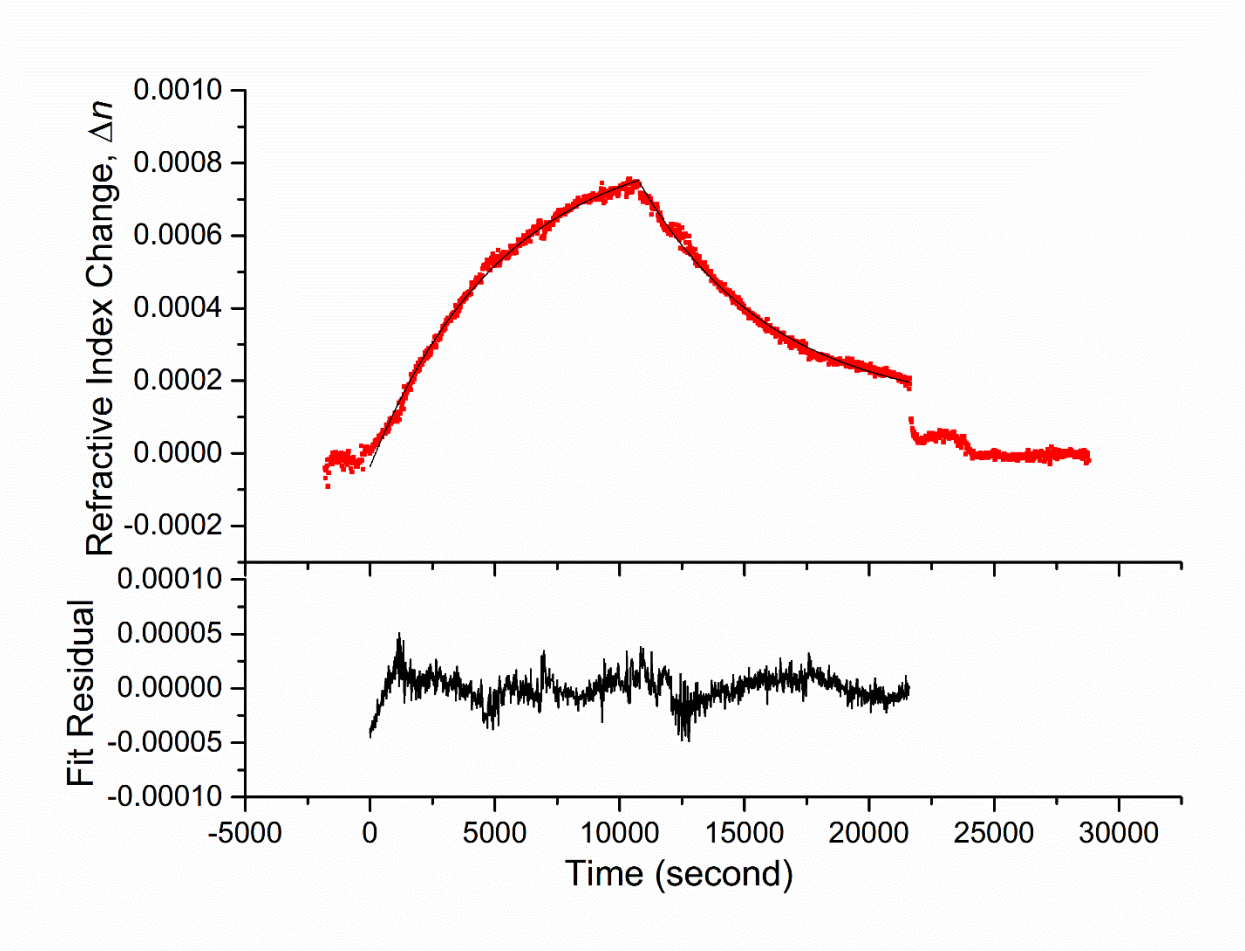

Figure 5-10 *Single exponential function fits of 50 ppb Pb(II) ion adsorption and desorption processes on the S_4-PMS coating, with fit residual shown below.*

Table 5-8 Fitting parameters for single exponential function (5.1) and (5.3) fits of the 50 ppb Pb(II) ion adsorption and desorption on the S_4-PMS coating of the figure above.

	Adsorption	**Desorption**
$q_{e,X}$ **or** $q_{0,X}$ ***(RIU)***	0.000911(4)	0.000633(3)
τ_X **or** τ_X **(s)**	5340(60)	5340(80)

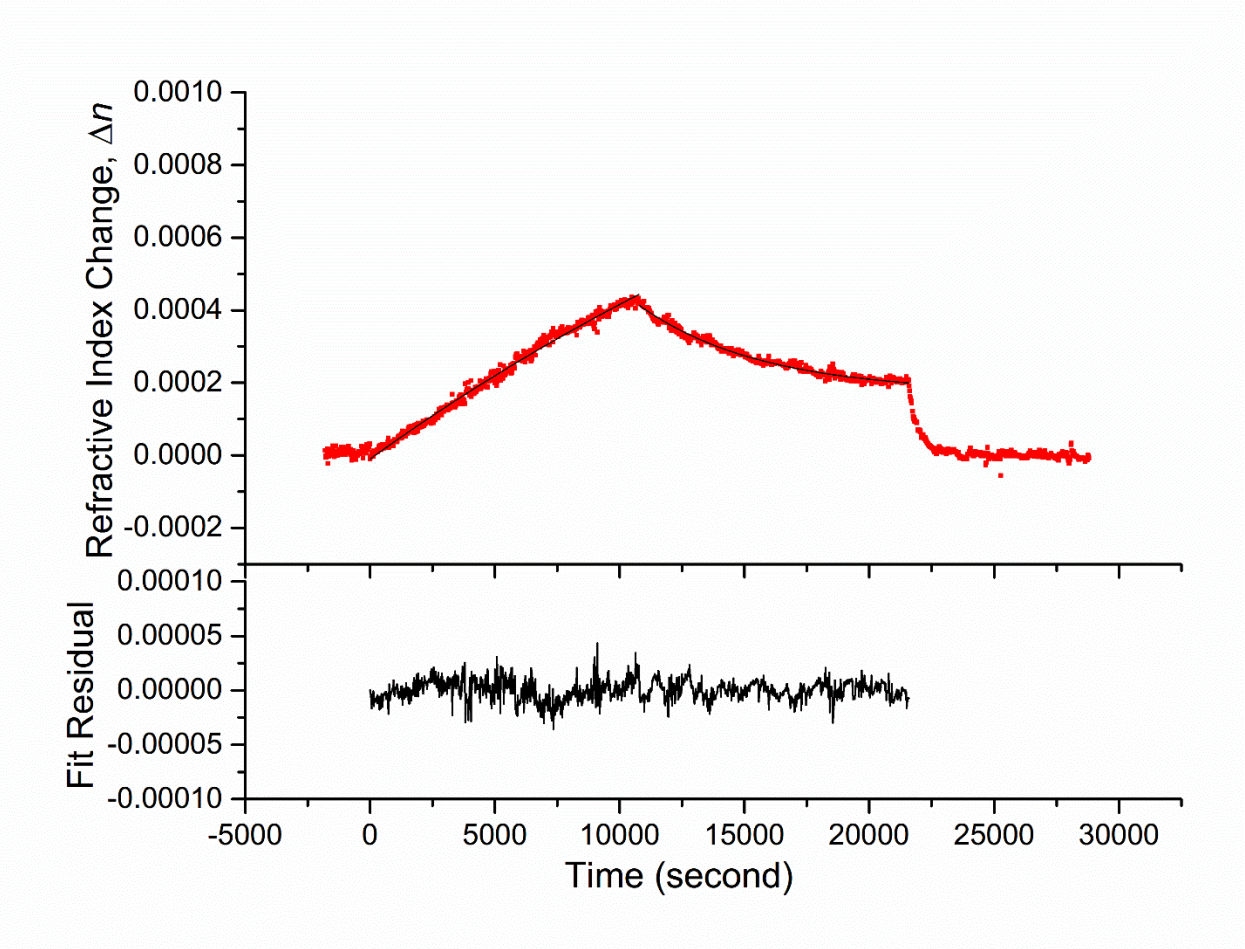

Figure 5-11 *Single exponential function fits of 20 ppb Pb(II) ion adsorption and desorption processes on the S_4-PMS coating, with fit residual shown below.*

Table 5-9 Fitting parameters for single exponential function (5.1) and (5.3) fits of the 20 ppb Pb(II) ion adsorption and desorption on the S_4-PMS coating of the figure above.

	Adsorption	**Desorption**
$q_{e,X}$ **or** $q_{0,X}$ **(RIU)**	0.00016(1)	0.000240(2)
τ_X **or** τ_X **(s)**	32000(3000)	4900(100)

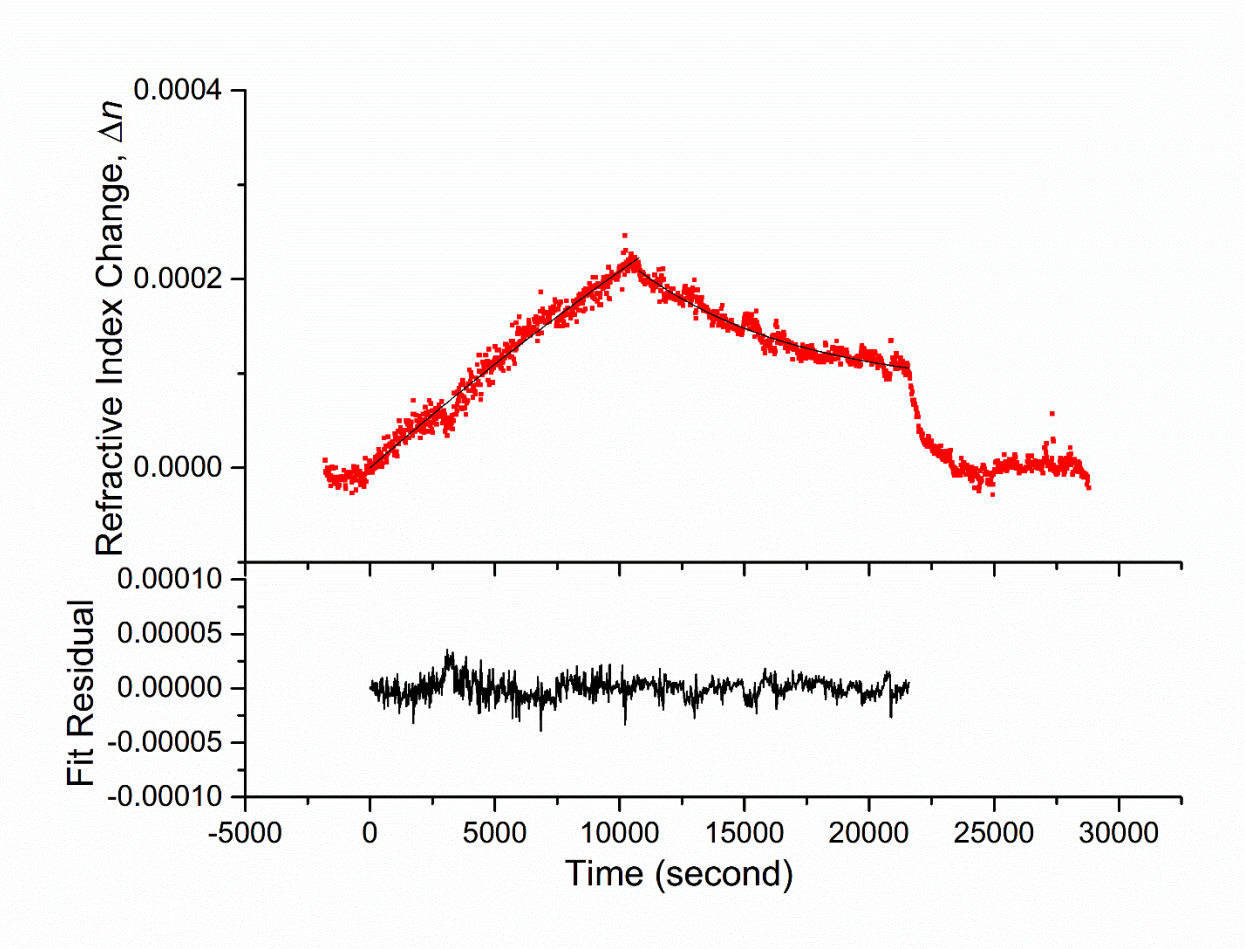

Figure 5-12 *Single exponential function fits of 10 ppb Pb(II) ion adsorption and desorption processes on the S_4-PMS coating, with fit residual shown below.*

Table 5-10 Fitting parameters for single exponential function (5.1) and (5.3) fits of the 10 ppb Pb(II) ion adsorption and desorption on the S_4-PMS coating of the figure above.

	Adsorption	**Desorption**
$q_{e,X}$ **or** $q_{0,X}$ **(RIU)**	0.0011(2)	0.000126(3)
τ_X **or** τ_X **(s)**	46000(9000)	6400(300)

5.1.5 The Linear Relationship Between the Initial Adsorption Rates and the Pb(II) concentration

The initial adsorption rates could be calculated by using equation (5.5).

$$\text{single site:}\quad \left.\frac{d[MY](t)}{dt}\right]_{t=0} = k_a[Y]_0[M] = \frac{q_e}{\tau_a}$$
$$\text{two site:}\quad \left.\frac{d([MX]+[MY])(t)}{dt}\right]_{t=0} = \left(k_{a,X}[X]_0 + k_{a,Y}[Y]_0\right)[M] = \frac{q_{e,X}}{\tau_{a,X}} + \frac{q_{e,Y}}{\tau_{a,Y}} \tag{5.5}$$

The results are shown in Table 5-11 and plotted in Figure 5-13. As shown in Table 5-11, the double exponential fit errors were large for low concentrations (100 ppb, 50 ppb, 20 ppb, and 10 ppb). For these low concentration tests, a single exponential fit gave a smaller error. The most plausible explanation was that the strong binding site would bind the Pb(II) ions first before the weak binding sites started to be occupied. When the concentration was high (1000ppb – 200ppb), the strong binding sites quickly get saturated so that the weak binding sites started to adsorb Pb(II). When the concentration was low(< 100ppb), however, the strong binding site had not reached saturation in the 3-hour adsorption test, and the weak binding site did not adsorb Pb(II) ions at detectable concentrations. Hence the single adsorption curves were observed.

A linear relationship could be observed for initial adsorption rate into the tightly bound site, with a slope of $k_{a,Y}[X]_0 = 5.05(5)\times10^{-9}$ RIU/s. The detection limit was 30 ppb, assuming error free calibration. The detection limit was calculated using the spreadsheet of reference [51].

Table 5-11 Initial Adsorption rate of Pb(II) solutions at different concentrations

	Pb(II) Conc. (ppb)	***q_e or $q_{e,X}$***	***τ_a or $\tau_{a,X}$* (s)**	***$q_{e,Y}$***	***$\tau_{a,Y}$* (s)**	***Initial Rate (RIU/s)***
Double exponential fit	1000	0.00140(1)	283(5)	0.00019(1)	2000(200)	$5.01(3)\times10^{-6}$
	500	0.00133(2)	515(8)	0.00009(4)	4915(400)	$2.06(9)\times10^{-6}$
	300	0.00120(1)	869(13)	0.00014(2)	10000(5000)	$1.39(4)\times10^{-6}$
	200	0.0009(1)	1182(74)	0.0002(1)	3000(1000)	$8\ (1)\times10^{-7}$
Single exponential function fit		***q_e***	***τ_a*(s)**	***Initial Rate (RIU/s)***		
	100	0.00107 (2)	2660(20)	$4.03(3)\times10^{-7}$		
	50	0.00091(3)	5340(60)	$1.70(3)\times10^{-8}$		
	20	0.0016(1)	32000(3000)	$5.0(8)\times10^{-8}$		
	10	0.0011(2)	50000(10000)	$2(1)\times10^{-8}$		

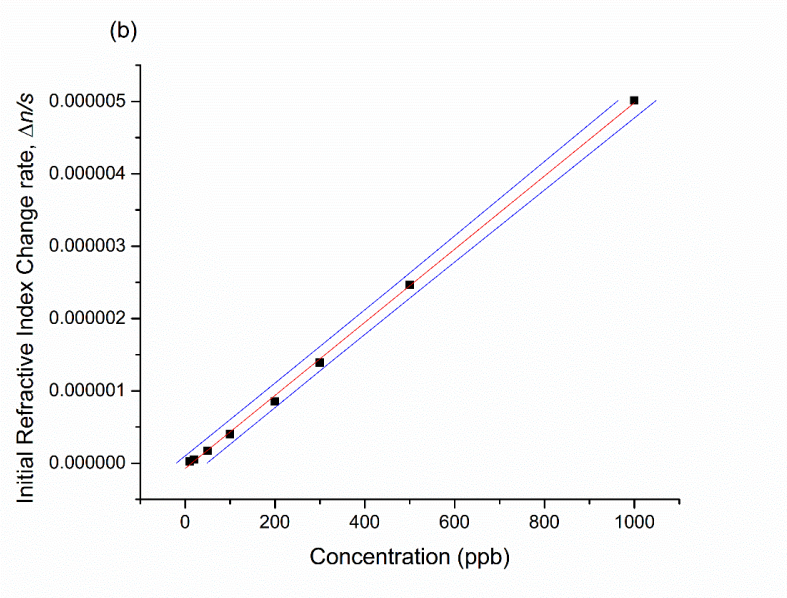

Figure 5-13 *Initial refractive index change rate at different concentrations of Pb(II) ion. The black dots represent calculated initial rates. The red line represents a linear fit. The two blue lines represent the 99% confidence intervals calculated as ±3σ. [51].*

5.1.6 Determination of Rate Constants, Equilibrium Constants and Adsorption Capacities for Pb(II) ion adsorption

This section used the models and all experimental results to determine the films characteristic parameters as described in chapter 3. As explained in the previous section, the double exponential fit worked for high concentration, and the single exponential fit worked for low concentrations. This suggested that at low concentration (100 ppb, 50 ppb, 20 ppb, 10 ppb), only the strong binding sites X bound Pb(II) ions. Also, data from the two lowest concentrations (20 ppb and 10 ppb) was not used due to large fit errors. As a result, only data for strong binding sites with Pb(II) concentration at 1 ppm to 50 ppb was used in the following calculation.

Calculate $k_{d,X}$ From Desorption Curves

Based on equation (5.6)

$$\left(\left[MX\right]+\left[MY\right]\right)(t)=\left[MX\right]_0\exp\left(-k_{d,X}t\right)+\left[MY\right]_0\exp\left(-k_{d,Y}t\right) \tag{5.6}$$

$k_{d,X} = 1/\tau_{d,X}$. The rate constants $k_{d,X}$ for each desorption curve are shown in Table 5-12. The average value was $1.84(3)\times10^{-4}$ s^{-1}.

Table 5-12 Pb(II) Desorption data sets for $k_{d,X}$ calculation

Pb(II) Conc. (ppb)	$\tau_{d,X}$ (s)	$k_{d,X}$ (s^{-1})
1000	5300(100)	$1.90(4)\times10^{-4}$
500	5700(40)	$1.75(1)\times10^{-3}$
300	5700(300)	$1.76\ (8)\times10^{-3}$
200	5600(200)	$1.77(5)\times10^{-4}$
100	5540(70)	$1.81(2)\times10^{-4}$
50	5340(80)	$1.87(3)\times10^{-4}$
20	4900(100)	$2.05(5)\times10^{-4}$
10	6400(300)	$1.55(8)\times10^{-4}$

Calculate $k_{a,X}$, $k_{d,X}$, and $K_{a,X}$ from Adsorption Curves

The adsorption time constants were obtained by fitting the data to equation (5.7),

$$\begin{aligned}\left(\left[MX\right]+\left[MY\right]\right)(t) = &\frac{k_{a,X}'\left[X\right]_0}{\left(k_{a,X}'+k_{d,X}\right)}\left[1-\exp\left(-\left(k_{a,X}'+k_{d,X}\right)t\right)\right] \\ &+\frac{k_{a,Y}'\left[Y\right]_0}{\left(k_{a,Y}'+k_{d,Y}\right)}\left[1-\exp\left(-\left(k_{a,Y}'+k_{d,Y}\right)t\right)\right]\end{aligned} \tag{5.8}$$

Recognizing that $\tau_{a,X} = 1/(k_{a,X}'+k_{d,X})$ and $k_{a,X}' = k_{a,X}[M]$, both $k_{a,X}$ and $k_{d,X}$ can be obtained from the linear fit

$$\frac{1}{\tau_{a,X}} = k_{a,X}[M]+k_{d,X} \tag{5.9}$$

Fitting $1/\tau_{a,X}$ as a function of $[M]$ with a linear function yielded $k_{a,X} = 5.2(1)\times10^{1}$ $(RIU\cdot s)^{-1}$, $k_{d,X} = 8(4)\times10^{-5}$ s^{-1}, and an equilibrium constant $K_{a,X} = k_{a,X}/k_{d,X} = 8\ (4)\times10^{5}$ RIU^{-1}. The fit line is shown in Figure 5-14, and the parameters are listed in Table 5-13.

However, this $k_{d,X}$ had a large error. By using $k_{d,X}$ calculated from desorption curves in the previous step, a more precise $K_{a,X}$ could be obtained. In this fit, $k_{a,X} = 5.0(1)\times10^{1}$ $(RIU\cdot s)^{-1}$, $k_{d,X} = 1.84(3)\times10^{-4}$ s^{-1}, $K_{a,X} = 2.8\ (1)\times10^{5}$ RIU^{-1}.

Table 5-13 Pb(II) data sets for $k_{a,X}$, $k_{d,X}$, $K_{a,X}$, and $[X]_0$ calculation

Pb(II) Conc. (ppb)	*Pb(II) Conc. (RIU)*	$[MX]_{eq,a}$ *(RIU)*	$\tau_{a,X}$ (s)	$[MY]_{eq,a}$ *(RIU)*	$\tau_{a,Y}$ (s)	$1/\tau_{a,X} = k_{a,X} \cdot [M] + k_{d,X}$	$[M]/[MX]_{eq,a}$
1000	6.776×10^{-5}	0.00140(1)	283(5)	0.00019(1)	2000(200)	$3.52(6)\times10^{-3}$	0.0485(5)
500	3.388×10^{-5}	0.00133(2)	515(8)	0.00009(4)	4900(400)	$1.94(3)\times10^{-3}$	0.0255(5)
300	2.033×10^{-5}	0.00120(1)	869(13)	0.00014(2)	10000(5000)	$1.15\ (2)\times10^{-3}$	0.0169(2)
200	1.355×10^{-5}	0.0009(1)	1182(74)	0.0002(1)	3000(1000)	$8.5(5)\times10^{-4}$	0.014(2)
100	6.78×10^{-6}	0.001073(2)	2660(20)	---	---	$3.76(2)\times10^{-4}$	0.006(1)
50	3.39×10^{-6}	0.000911(4)	5350(60)	---	---	$1.87(2)\times10^{-4}$	0.004(2)

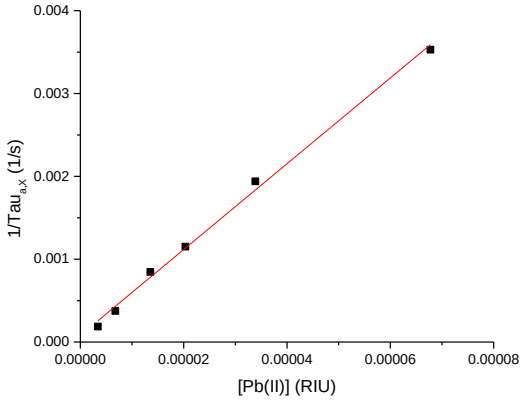

Figure 5-14 *Diagram showing $1/\tau_{a,X}$ has a linear relationship with Pb(II) concentration. By fitting $1/\tau_{a,X}$ vs. Pb(II) concentration, $k_{a,X}$, $k_{d,X}$, and $K_{a,X}$ for Pb(II) ion adsorption on the S_4-PMS coating could be calculated from a linear fit.*

Calculate $K_{a,X}$ and $[X]_0$ from Adsorption Curves

The second Method to calculate equilibrium constant K was using equation (3.13)

$$\frac{1}{[MX]_{eq,a}} = \frac{1}{[X]_0} + \frac{k_{d,X}}{k_{a,X}[X]_0}\frac{1}{[M]} \tag{3.13}$$

which could be rearranged to give

$$\frac{[M]}{[MX]_{eq,a}} = \frac{[M]}{[X]_0} + \frac{1}{K_{a,X}[X]_0} \tag{5.10}$$

By fitting $[M]/[MX]_{eq,a}$ vs. $[M]$ with a linear function (data listed in Table 5-13), $K_{a,X}$ and $[X]_0$ could be calculated from the intercept and the slope. The fit curve is shown in Figure 5-15. The equilibrium constant

$K_{a,X}$ was calculated to be 2.5 (9)×10^5 RIU^{-1}, close to the value (2.8 (1)×10^5 RIU^{-1}) calculated using the previous method. From this equilibrium constant, $\Delta_r G_m^\circ$(Pb(II)X) was calculated to be $\Delta_r G_m^\circ$(Pb(II)X) $= RT\ln K_{a,X}$ = 42(2)kJ/mol. The concentration of total binding sites was $[X]_0$ = 0.00147(6) RIU. Mole fraction of binding site X = 0.00147(6) RIU/(0.780RIU/mole fraction) = 0.00188(8) mol X binding site/mol film.

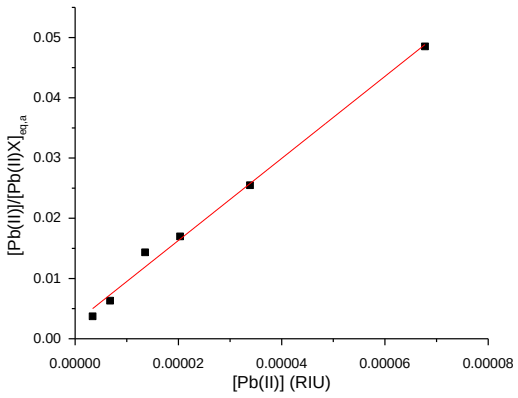

Figure 5-15 *[Pb(II)]/[Pb(II)X]$_{eq,a}$ showing a linear relationship with Pb(II) concentration. By fitting [Pb(II)]/[Pb(II)X]$_{eq,a}$ vs. [M] with a linear function, $K_{a,X}$ and $[X]_0$ for Pb(II) ion adsorption on the S_4-PMS coating could be calculated.*

Notice that Figure 5-15 and Figure 5-14 have similar shapes. That is because Equation (5.11) and equation (5.12) are equivalent. From equation (3.11), equation (5.13) can be derived.

$$[MX]_{eq} = \left([MX]\right)(t)_{eq} \underline{\underline{t \to \infty}} \frac{k_{a,X}'[X]_0}{\left(k_{a,X}' + k_{d,X}\right)} = k_{a,X}[M][X]_0\tau_{a,X} \qquad (5.13)$$

Equation (5.14) can be derived by substituting equation (5.13) into (5.15). Both equations are useful, as they give different reaction constants.

5.2 Pb(II) Ion Adsorption and Desorption in Tap Water

$Pb(NO_3)_2$ was spiked into tap water (Kingston, 2016) to make a 1 ppm Pb(II) solution. The solution was pumped flowing across the S_4-TEOS-coated chip, and the adsorption curves and tap water desorption curves were recorded.

5.2.1 Adsorption Curve of Tap Water of the S_4-PMS Coating

The tap water used in this research was obtained from the Chernoff Hall, room 334 tap water faucet. According to Kingston water treatment plant report, tap water in Kingston contained high concentrations of Ca(II), Na(I), and other ions (Table 5-14) [52]. These ions bound to the binding sites in the coating, and increased the coating's refractive index by about 0.005 RIU, as shown in Figure 5-16, which was about 2-3 times higher than the largest shifts in the 1 ppm Pb(II) adsorption tests. The adsorption took at least 5 hours to reach equilibrium. The coating was immersed in tap water overnight before conducting Pb(II) tests.

Table 5-14 Ion concentrations in Kingston tap water.

Parameter	Results Range	Unit of measure
pH	8.04 – 8.22	
Al	0.01-0.03	mg/L
Ca	33.5 – 38.2	mg/L
Fe	<0.005	mg/L
Na	16.6-17.2	mg/L
Pb	0.00002-0.00003	mg/L
Hg	<0.00002	mg/L

The tap water appeared to erode the S_4-PMS coating faster than DI water. The baseline drifted by $-6.62(1)\times10^{-8}$ RIU/s, compared to $-1.359(7)\times10^{-8}$ RIU/s for DI water (Figure 5-17).

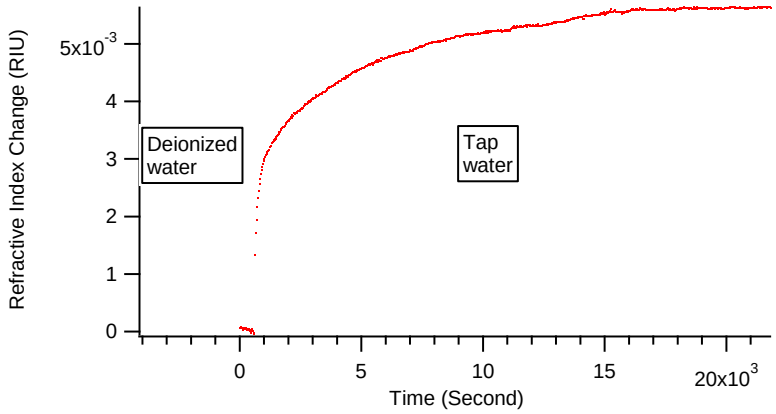

Figure 5-16 *Tap water adsorption curve of S_4-PMS coating.*

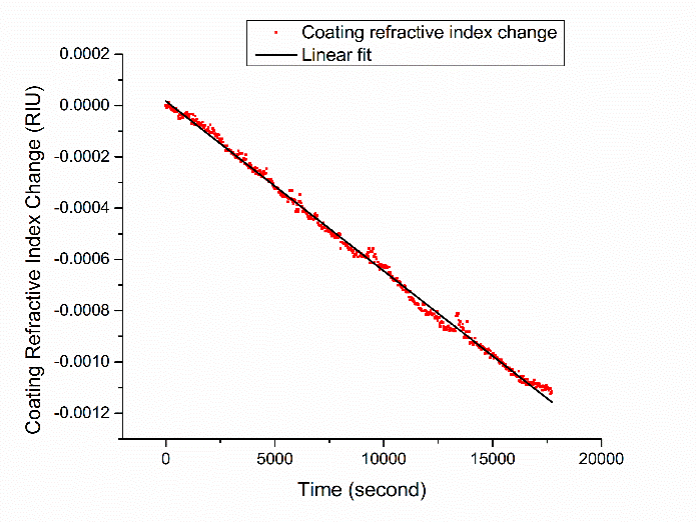

Figure 5-17 *Tap water baseline of S4-PMS coating.*

5.2.2 Pb(II) Ion Adsorption and Desorption on the S_4-PMS Coating in Tap Water

The coating was immersed in tap water overnight, and conditioned for 1 hour in tap water flow (flow rate = 0.9 ml/min) before changing to 1 ppm Pb(II) tap water solution. The Pb(II) adsorption test was done for 3 hours before the 3-hour tap water desorption test. In these experiments, Na_2EDTA desorption was not attempted, as Na_2EDTA would remove not only adsorbed Pb(II) ion but all other metal ions as well.

The adsorption-desorption curve could be fitted satisfactorily with single exponential functions, but the bi-exponential reduced the residual substantially. The fit curves are shown in Figure 5-18, and the fit parameters are shown in Table 5-15. The initial adsorption rate was calculated as 6.50×10^{-7} RIU/second, which was much smaller than the initial adsorption rate in DI water (4.78×10^{-4} RIU/second) for the same concentration of 1 ppm Pb(II). Consequently, adsorption took a much longer time to reach equilibrium. It was likely that the coating already contained other ions (Ca^{2+}, Mg^{2+}, etc.) in its binding sites after exposure to tap water. The adsorption process and desorption processes were then, in effect, ion exchange processes.

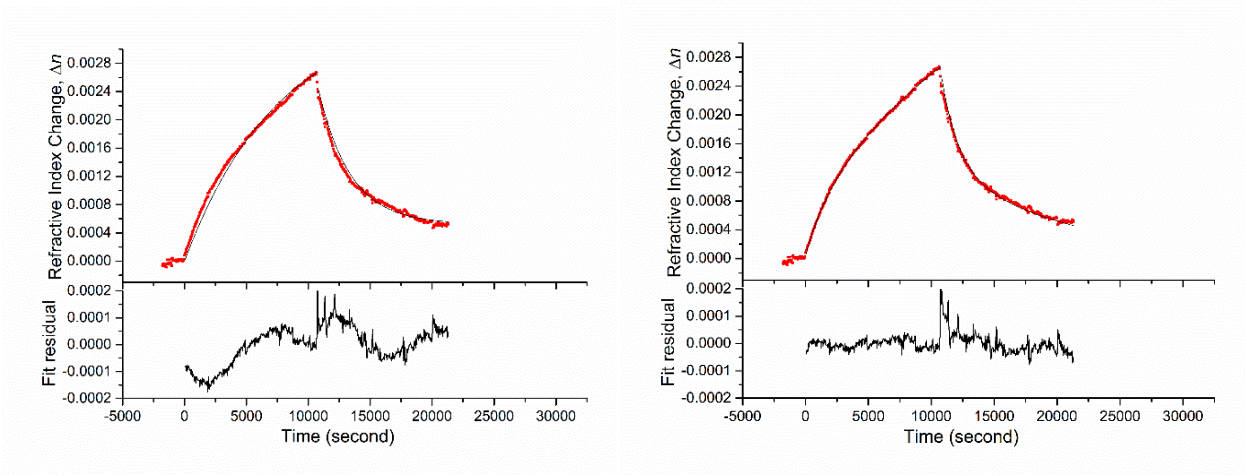

Figure 5-18 *Comparison between single and double exponential functions fits of 1ppm Pb(II) ion tap water solution adsorption and desorption on the S_4-PMS coating. (Left) The fit to a single exponential function with the fit residual plotted on the bottom. (Right) The fit to a double exponential function with the fit residual plotted on the bottom.*

Table 5-15 Fitting parameters for single and double exponential function fits of Pb(II) tap water solution adsorption and desorption of S_4-PMS coating.

Single site model			Two site model		
	Adsorption	**Desorption**		**Adsorption**	**Desorption**
q_e **or** q_0 ***(RIU)***	0.00350(2)	0.00192(1)	$q_{e,X}$ **or** $q_{0,X}$ ***(RIU)***	0.00056(9)	0.0013 (1)
τ **(s)**	7460(10)	2590(30)	τ_X **or** τ_X **(s)**	1460(20)	11200(300)
---	---	---	$q_{e,Y}$ **or** $q_{0,Y}$ ***(RIU)***	0.0042(2)	0.00128(7)
---	---	---	τ_Y **or** τ_Y **(s)**	15900(200)	1360(70)

The data were not simple to interpret, but drawing on the above hypothesis of the two site model, the fast adsorption process was followed by a slow desorption process, with time constants τ_X = 1460 s and 11200 s, which were comparable to those listed in Table 5-1, i.e. τ_X = 300 s and 18000 s, albeit with a much slower adsorption process. Maybe not surprisingly, the slower of the two processes with an adsorption time constant of τ_X = 16000 s and desorption constant of 1400 s, also showed a slower uptake compared to the adsorption in DI water (τ_X = 4650 s) and a faster release (τ_X = 2610 s with DI water). All this was consistent

with a replacement of loosely bound ions found in tap water by Pb(II), a process that was efficient when these ions were bound to tetrasulfide groups, but very slow when they were bound non-specifically.

5.3 Pb(II) Ion Adsorption in Seawater on S_4-PMS coating

A seawater sample (Sigma-Aldrich, St. Louis, MO)) was applied to the S_4-PMS coated ring resonator and the response was recorded. Like tap water, the seawater eroded the coating faster than tap water did. When DI water was replaced with seawater, the coating's refractive index jumped by 0.004, and then decreased quickly. As shown in Figure 5-19 and Figure 5-20, the seawater baseline drifted fast, with a rate of $-1.233(4)\times10^{-6}$ RIU/s, compared to $-1.359(7)\times10^{-8}$ RIU/s for DI water. The seawater was then spiked with 1 ppm Pb(II) and flowed on the chip to test whether adsorption can be observed (Figure 5-20). Unfortunately, no adsorption was observed. All binding sites were presumably occupied by other ions, especially Fe(III), which was found to bind strongly to the binding sites in the S_4-PMS coating (see section 6.8). Binding processes of other metal ions were discussed in chapter 6. It was also possible that Pb formed stable complexes with the anions in the seawater, such as CO_3^{2-}, and thereby lost its binding ability with the binding site in the S_4-PMS coating.

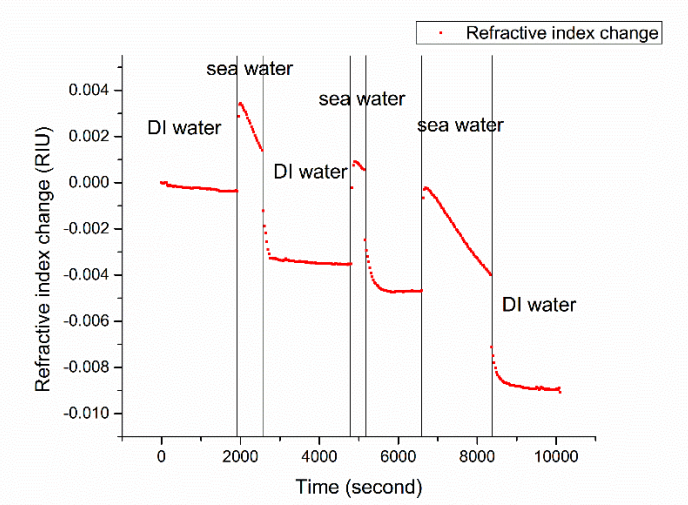

Figure 5-19 *S_4-PMS coating refractive index change when alternating between DI water and seawater flow. Flow rate = 0.9 ml/min. Seawater was corrosive to the S_4-PMS coating.*

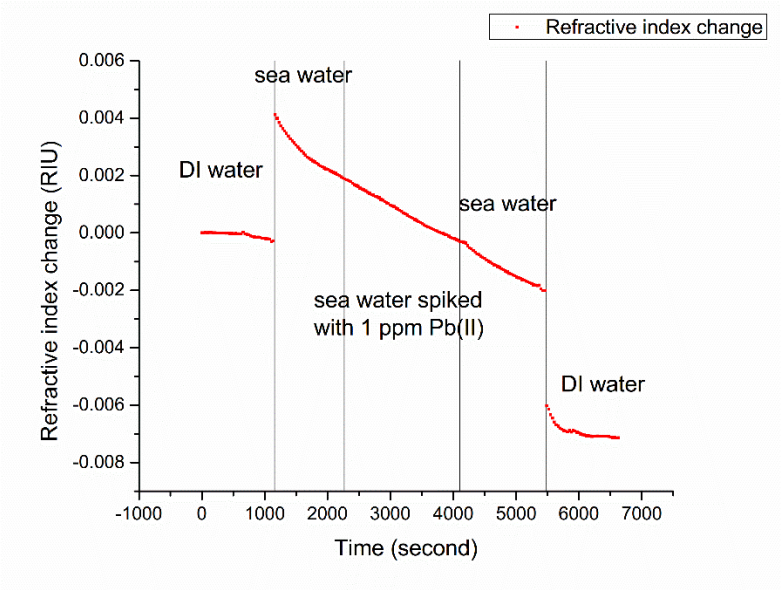

Figure 5-20 *Seawater spiked with 1ppm Pb(II) adsorption and desorption test on S_4-PMS coated ring resonator. The recorded coating refractive index showed a great decrease due to corrosion, but no measurable change for Pb(II) adsorption or desorption.*

5.4 Hg(II) Ion Adsorption and Desorption Tests in DI Water

This section includes the models and all experimental results on the adsorption and desorption of Hg(II) solutions in DI water on S_4-PMS-coated SOI tandem ring resonators. The tests were carried out at different concentrations (1000 ppb to 20 ppb) to determine the relationship between the Hg (II) concentrations, the respective rate constants, available sites and initial adsorption rates.

5.4.1 Tests on the S_4-PMS Coating

The initial way to prepare Hg(II) sample was to dissolve $Hg(NO_3)_2 \bullet H_2O$ (Sigma-Aldrich) in DI water to make a 1000 ppb Hg(II) solution. However, the salt hydrolyzed, leaving an orange solid residue that did not dissolve. To fully dissolve the salt, HNO_3 was added to adjust the pH to 5.30. The pH of DI water used when recording desorption curve was also adjusted with HNO_3 to pH = 5.3 to remain consistent. As usual, the data sample rate was 30 seconds per data point, and the flow rate was 0.9 ml/min. The adsorption lasted 3 hours, the desorption process with acidified DI water lasted for 3 hours, and 1 ppm Na_2EDTA solution was added for 1 hour to remove residual bound metal ions. Single exponential and

double exponential equations (5.1) to (5.4) were used to fit the adsorption-desorption curve. The fit parameters are listed in Table 5-16. As shown in Figure 5-21, the fit residuals improved dramatically when changing from a one-site binding model to a two-site binding model for the adsorption and water desorption process. The fit to the desorption process using Na_2EDTA did not require a second exponential function, however. The single exponential and double exponential functions fitted equally well. Later tests showed that acidified EDTA was required to fully remove Hg from the coating.

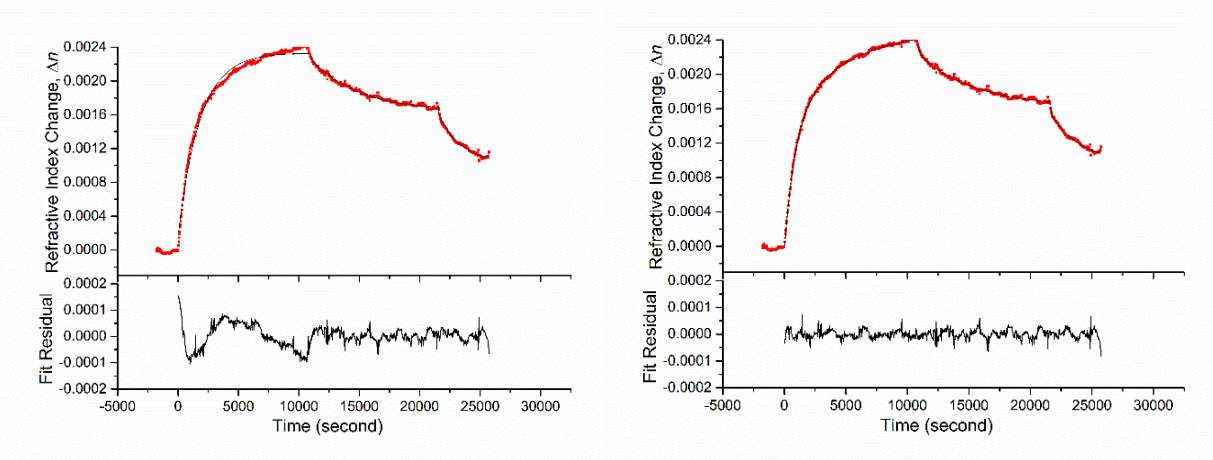

Figure 5-21 *Comparison between single and double exponential functions fits of 1 ppm Hg(II) ion DI water solution adsorption and desorption on the S_4-PMS coating. (Left) The fit to a single binding site adsorption-desorption process with residual. (Right) The fit to a two binding site adsorption-desorption process with residual.*

Table 5-16 Fitting parameters for single exponential functions (5.1) and (5.3), and double exponential equations (5.2) and (5.4) to describe the Hg(II) ion adsorption and desorption on the S_4-PMS coating of Figure 5-21. The decay time τ are given in seconds, and the loadings are given in values in three different units, calculated based on Table 3-1.

Single site model				
Parameter	**Unit**	**Adsorption**	**Desorption**	**Na_2EDTA rinse**
q_e **or** q_0	***RIU***	0.00216 (1)	0.00065(4)	0.00057(9)
	mol(Hg)/mol(film)	0.00179(1)	0.000539(4)	0.000471(7)
	g(Hg)/g(wet film)	0.00916(6)	0.00276(2)	0.00241(4)
	g(Hg)/g(dry film)	0.0119(8)	0.00360(2)	0.00315(5)
τ	**s**	1820(20)	3900(90)	1830(30)
Two site model				
Parameter	**Unit**	**Adsorption**	**Desorption**	**Na_2EDTA rinse**
$q_{e,X}$ **or** $q_{0,X}$	***RIU***	0.00159(4)	0.00012(1)	0.00011(2)
	mol(Hg)/mol(film)	0.00132(3)	0.0001(1)	0.00008(1)
	g(Hg)/g(wet film)	0.00676(2)	0.00049(5)	0.00045(6)
	g(Hg)/g(dry film)	0.00881(2)	0.00064(7)	0.00058(8)
τ_X **or** τ_X	**s**	960(30)	220(40)	90(30)
$q_{e,Y}$ **or** $q_{0,Y}$	***RIU***	0.00102(2)	0.00063(4)	0.00059(1)
	mol(Hg)/mol(film)	0.000840(2)	0.000519(4)	0.00048(1)
	g(Hg)/g(wet film)	0.00430(9)	0.00266(2)	0.00248(6)
	(g(Hg)/g(dry film)	0.00561(1)	0.00347(3)	0.00323(8)
τ_Y **or** τ_Y	**(s)**	6000(500)	4600(100)	22500(200)

The results indicate that two binding sites compete for the adsorption of Hg(II), with one site having a strong affinity for the metal ion and resulting in a fast adsorption process with a time constant τ = 860 s,

comparable to that of Pb(II) (τ = 900 s). The second process was slower, having an almost identical adsorption rate compared to Pb (II), i.e. τ = 4500 s for Hg(II) compared to τ = 4650 s for Pb(II). The desorption with water only removes the loosely bound Hg(II) ions. The second, fast desorption component having τ = 220 s for Hg(II) and a very small amplitude 0.00012 RIU was likely an artifact of the fit. The desorption was the best fit using a single exponential function, with a desorption time constant that was comparable to the Pb(II) desorption rate — it was τ = 3900 s for Hg(II) compared to τ = 2150 s for Pb(II). The remainder of the bound Hg(II) can only be removed with EDTA solution, or, better, with acidified EDTA solution.

5.4.2 Adsorption and Desorption at Different Hg(II) Concentrations

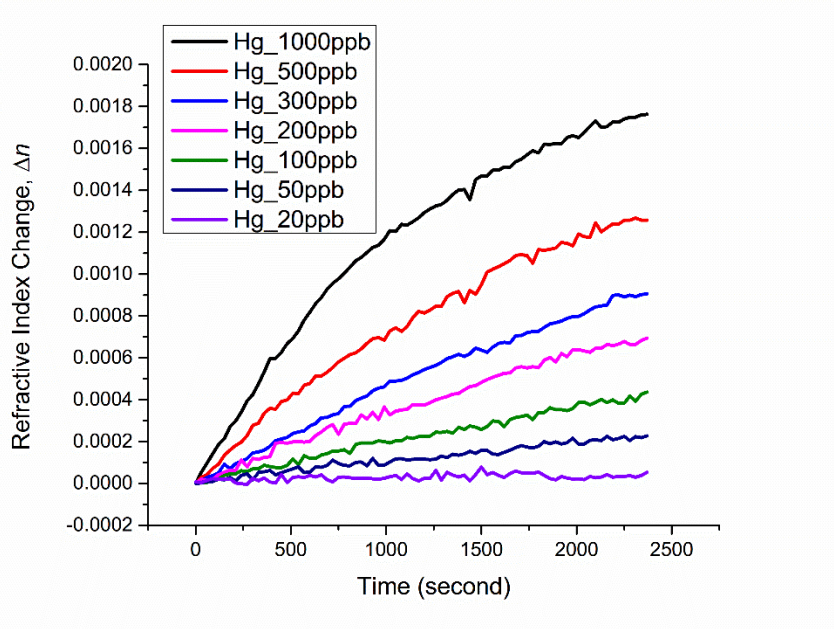

Figure 5-22 *The adsorption curve curves when the resonators were exposed to a series of Hg(II) solutions at 1000 ppb, 500 ppb, 300 ppb, 200 ppb, 100 ppb, 50 ppb, 20 ppb.*

The adsorption curves for a series of Hg ion solution samples (1000 ppb, 500 ppb, 300 ppb, 200 ppb, 100 ppb, 50 ppb, and 20 ppb) are shown in Figure 5-22. Each of these adsorption tests lasted 40 minutes. Although the 3-hour adsorption data presented in section 5.4.1 was fitted with a double exponential equation, the data sets shown in this section can be fitted with single exponential equations. The most

plausible explanation was that the strong binding site would bind the Hg ions first before the weak binding sites started to be occupied and, especially at low Hg(II) concentrations, the loading of Hg in the loose binding sites was negligible. The single exponential or linear fits for each curve are shown in Figure 5-23 to Figure 5-29, with fitting parameters shown in Table 5-17 to Table 5-23. For low concentrations (100 ppb, 50ppb, and 20 ppb), the single exponential functions had a large error on fitting parameters. When the concentrations were low and the adsorption time was short, the linear fit was a good approximation of single exponential fit at the given noise level.

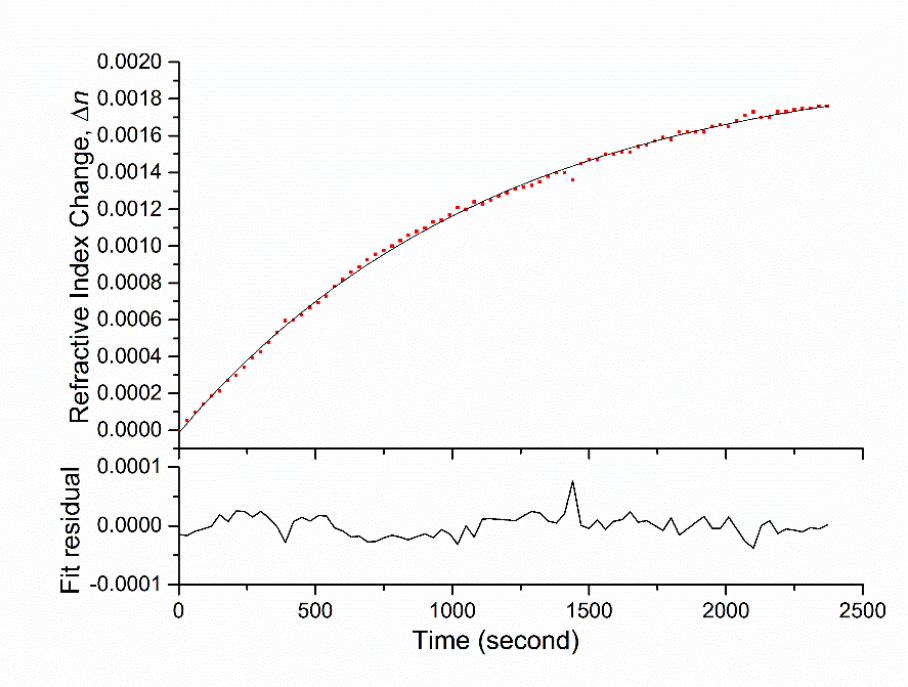

Figure 5-23 *Single exponential function fit of 1ppm Hg(II) ion 40 minutes adsorption process on the S_4-PMS coating, with fit residual shown below.*

Table 5-17 Fitting parameters for single exponential function (5.1) and (5.3) fits of the 1 ppm Hg(II) ion adsorption and desorption on the S_4-PMS coating of the figure above.

	Adsorption (Single Fit)
q_e **(RIU)**	0.00204 (1)
τ_a **(s)**	1160(20)

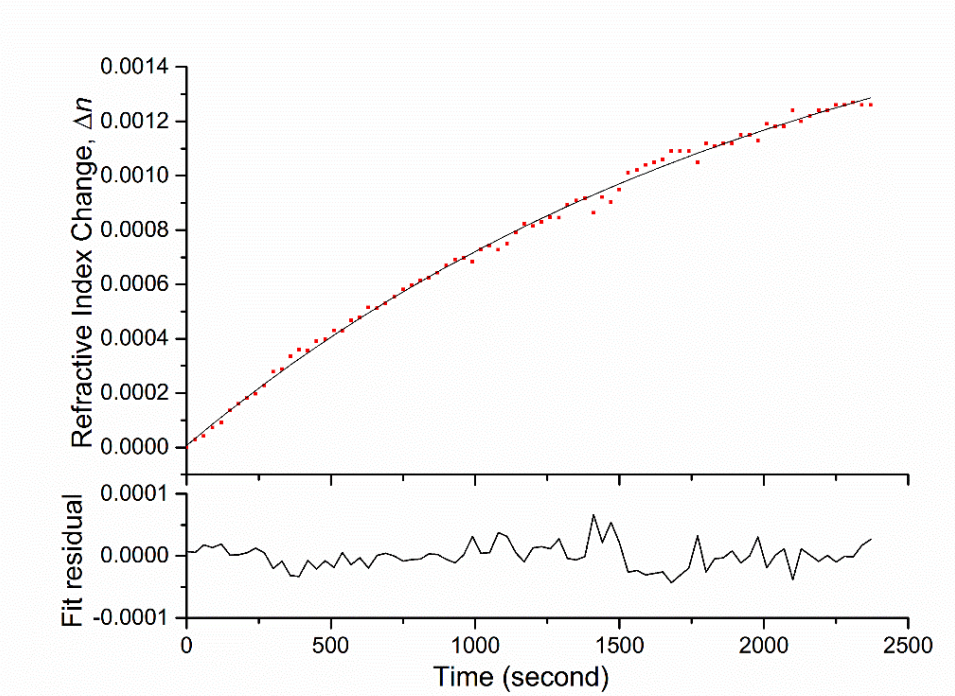

Figure 5-24 *Single exponential function fit of 500 ppb Hg(II) ion 40 minutes adsorption process on the S_4-PMS coating, with fit residual shown below.*

Table 5-18 Fitting parameters for single exponential function (5.1) and (5.3) fits of the 500 ppb Hg(II) ion adsorption and desorption on the S_4-PMS coating of the figure above.

	Adsorption (Single Fit)
q_e *(RIU)*	0.00191 (4)
τ_a **(s)**	2130(90)

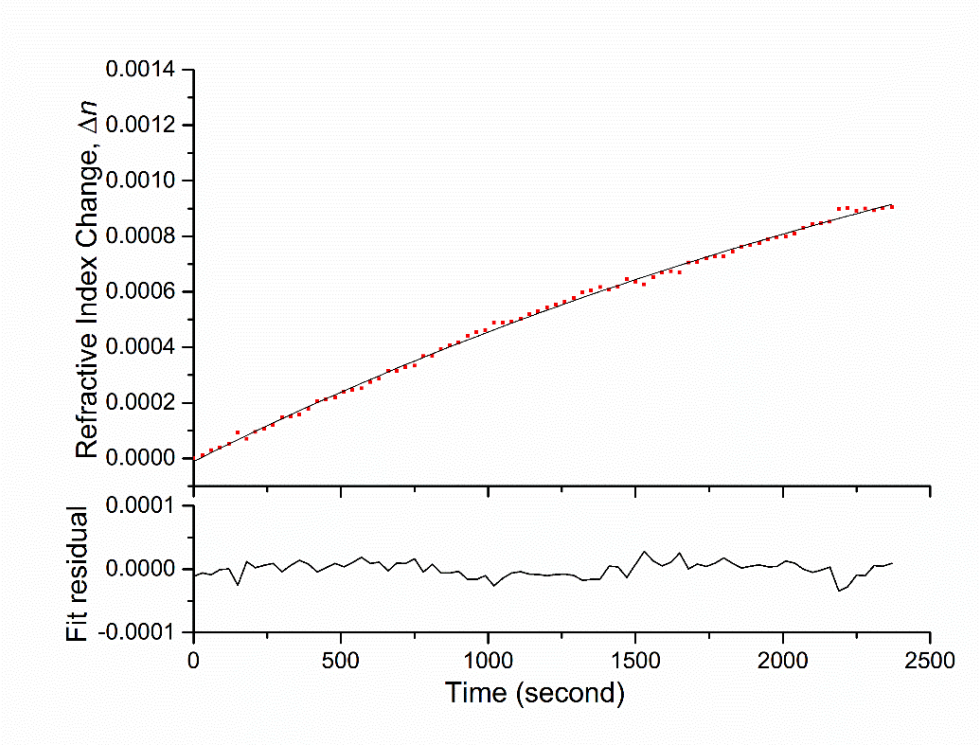

Figure 5-25 *Single exponential function fit of 300 ppb Hg(II) ion 40 minutes adsorption process on the S_4-PMS coating, with fit residual shown below.*

Table 5-19 Fitting parameters for single exponential function (5.1) and (5.3) fits of the 300 ppb Hg(II) ion adsorption and desorption on the S_4-PMS coating of the figure above.

	Adsorption (Single Fit)
q_e ***(RIU)***	0.00191 (8)
τ_a **(s)**	3600(200)

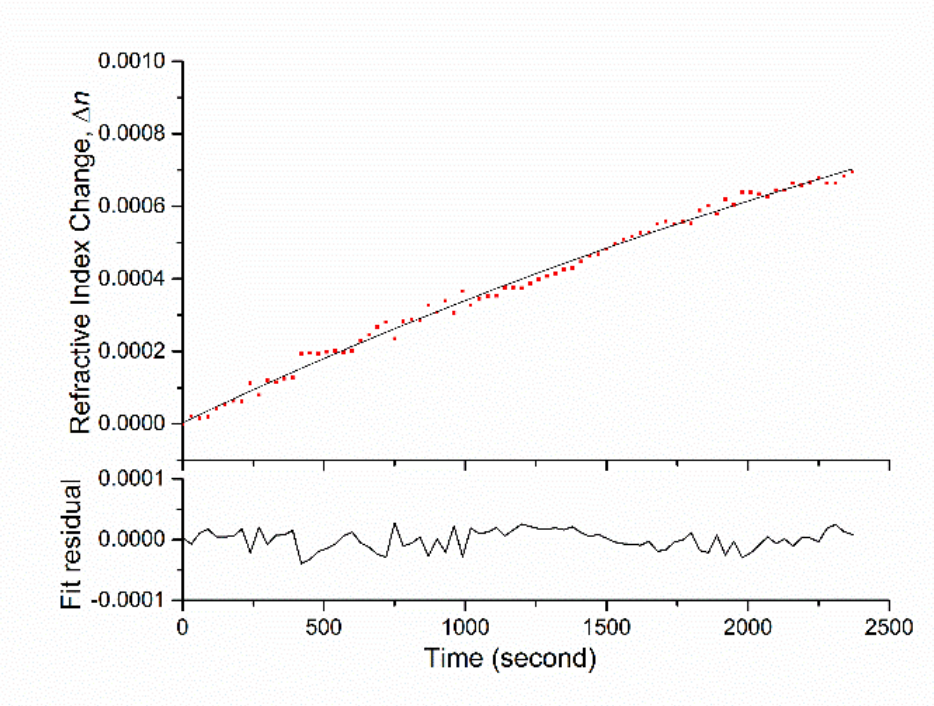

Figure 5-26 *Single exponential function fit of 200 ppb Hg(II) ion 40 minutes adsorption process on the S_4-PMS coating, with fit residual shown below.*

Table 5-20 Fitting parameters for single exponential function (5.1) and (5.3) fits of the 200 ppb Hg(II) ion adsorption and desorption on the S_4-PMS coating of the figure above.

	Adsorption (Single Fit)
q_e *(RIU)*	0.0018 (2)
τ_a **(s)**	4900(700)

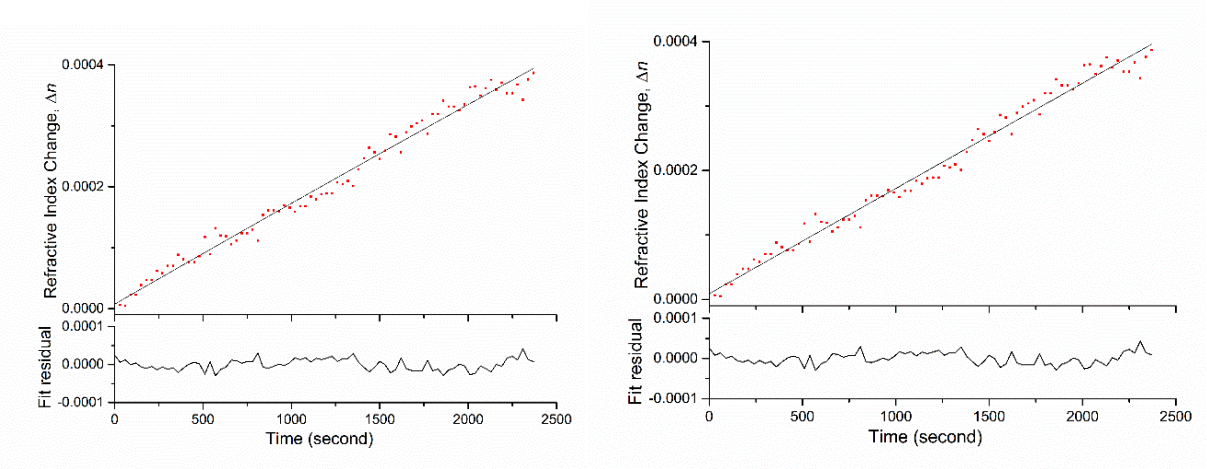

Figure 5-27 *Comparison between single exponential functions and linear fits of 100 ppb Hg(II) ion adsorption and desorption on the S_4-PMS coating. (Left) Single exponential function fit (Right) Linear function fit. Both fits had small residual, but the single exponential fit has large fit errors.*

Table 5-21 Fitting parameters for single exponential function (5.1) and (5.3) fits and linear fit of the 100 ppb Hg(II) ion adsorption and desorption on the S_4-PMS coating of the figure above.

	Adsorption (Single Fit)			**Adsorption (Linear Fit)**
q_e ***(RIU)***	0.0008(2)		***Intercept (RIU)***	$9(3)\times10^{-6}$
τ_a **(s)**	50000(1000)		***slope***	$1.63(2)\times10^{-7}$

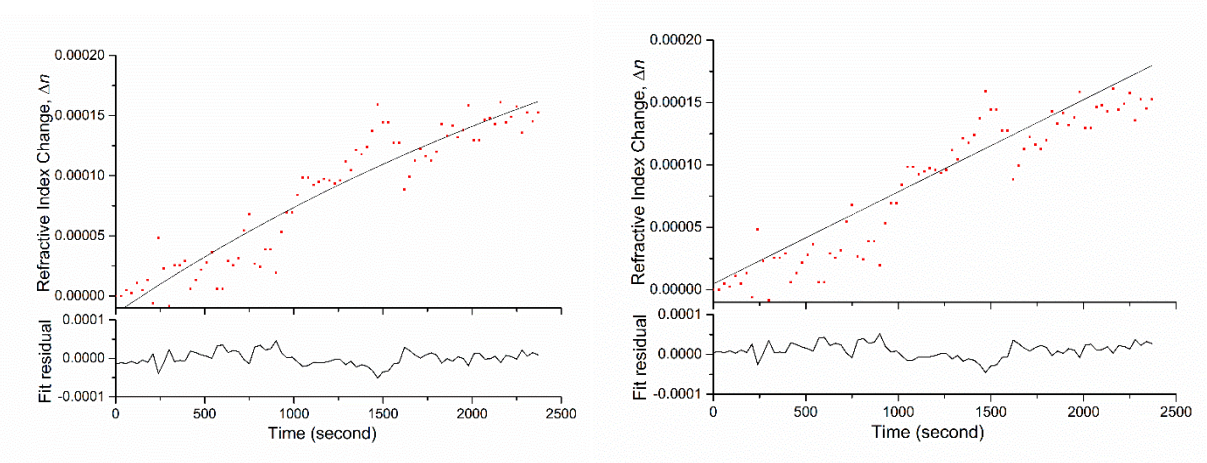

Figure 5-28 *Comparison between single exponential functions and linear fits of 50 ppb Hg(II) ion adsorption and desorption on the S_4-PMS coating. (Left) Single exponential function fit (Right) Linear function fit. Both fits had small residual, but the single exponential fit has large fit errors.*

Table 5-22 Fitting parameters for single exponential function (5.1) and (5.3) fits and linear fit of the 50 ppb Hg(II) ion adsorption and desorption on the S_4-PMS coating of the figure above.

	Adsorption (Single Fit)			**Adsorption (Linear Fit)**
q_e ***(RIU)***	0.0004 (1)		***Intercept (RIU)***	$5\,(4)\times10^{-6}$
τ_a **(s)**	4000(2000)		***slope***	$7.4(3)\times10^{-8}$

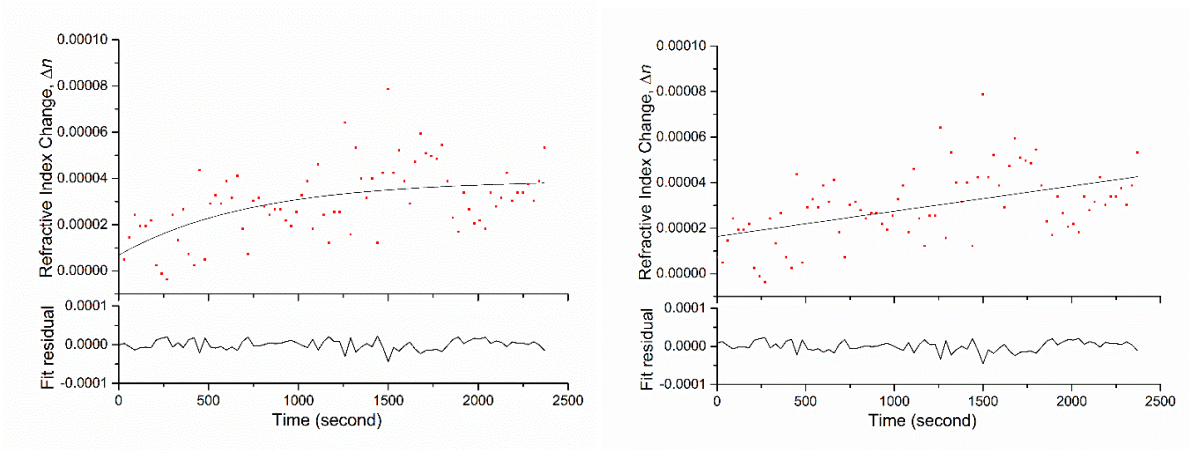

Figure 5-29 *Comparison between single exponential functions and linear fits of 20 ppb Hg(II) ion adsorption and desorption on the S_4-PMS coating. (Left) Single exponential function fit (Right) Linear function fit. Both fits had small residual, but the single exponential fit has large fit errors.*

Table 5-23 Fitting parameters for single exponential function (5.1) and (5.3) fits and linear fit of the 20 ppb Hg(II) ion adsorption and desorption on the S_4-PMS coating of the figure above.

	Adsorption (Single Fit)			**Adsorption (Linear Fit)**
q_e ***(RIU)***	0.000032(6)		***Intercept (RIU)***	$1.6(3)\times10^{-5}$
τ_a **(s)**	700(400)		***slope***	$1.1(2)\times10^{-8}$

5.4.3 Initial adsorption rates have a linear relationship with the Hg(II) concentration.

The initial adsorption rates could be calculated by using equation (5.5). The data are shown in Table 5-24 and plotted in **Figure 5-30**. As shown in Table 5-24, the single exponential fit errors were large for low concentrations (100 ppb, 50 ppb, 20 ppb). For these data sets, the values of τ were too large and the adsorption time was not long enough to give good fits at the current noise level. Linear fits gave smaller errors, while also giving a lower estimate of the initial adsorption rate. As a result, the single exponential function fit results were used for 1000 ppb to 200 ppb, while the linear fit results were used for 100 ppb to 20 ppb.

A linear relationship could be observed with a slope of $k_{a,Y}[Y]_0 = 1.74(1)\times10^{-9}$ RIU/s. The detection limit was 30 ppb, assuming error free calibration. The detection limit was calculated from the spreadsheet of reference. [51]

Table 5-24 Initial Adsorption rates at different concentration of Hg(II) solutions.

	Hg(II) Conc. (ppb)	q_e	τ_a **(s)**	***Initial Rate (RIU/s)***
Single exponential function fit	1000	0.00204(1)	1160(20)	$1.76(4)\times10^{-6}$
	500	0.00191(4)	2100(90)	$8.9(6)\times10^{-7}$
	300	0.00191(8)	3600(200)	$5.3(5)\times10^{-7}$
	200	0.0018(2)	4900(700)	$3.7(9)\times10^{-7}$
	100	0.0017(4)	8000(2000)	$1.7\ (8)\times10^{-7}$
	50	0.0012(8)	11000(8000)	$1.0(8)\times10^{-8}$
	20	0.000032(6)	700(400)	$4(3)\times10^{-8}$
Linear fit			***slops***	***Initial Rate (RIU/s)***
	100	-	$1.63(2)\times10^{-7}$	$1.63(2)\times10^{-7}$
	50	-	$7.4\ (3)\times10^{-8}$	$7.4\ (3)\times10^{-8}$
	20	-	$1.1(2)\times10^{-8}$	$1.1(2)\times10^{-8}$

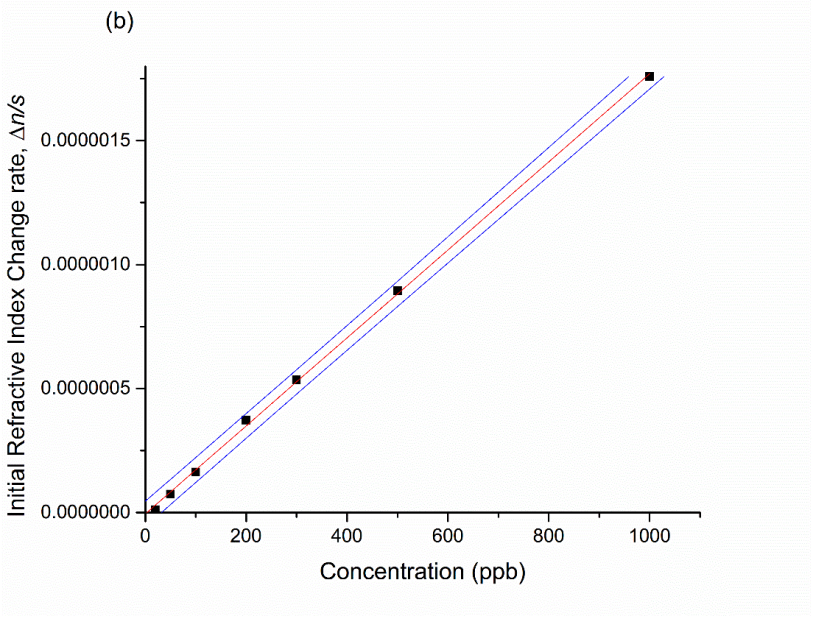

Figure 5-30 *Initial refractive index change rate at different concentrations of Hg(II) ion. The black dots represented calculated initial rates. The red line represents a linear fit. The two blue lines represent the 99% confidence intervals calculated as ±3σ. [51].*

5.4.4 Determination of Rate Constants, Equilibrium Constants and Adsorption capacities for Hg(II) ion

This section used the models and all experimental results to determine the films characteristic parameters as described in chapter 3. Binding sites X was used to represented strong binding sites.

Calculate $k_{a,X}$, $k_{d,X}$, and $K_{a,X}$ from Adsorption Curves

The determination of $k_{a,X}$ and $k_{d,X}$ for the strong binding sites was done using the same linear fit model as in section 5.1.6. A linear fit of the Hg(II) concentration, [M], to the inverse time constants $1/\tau_{a,X}$ according to equation (5.9) $1/\tau_{a,X} = (k_{a,X}'+k_{d,X})$ yielded $k_{a,X}$ = 3.33 (8) $\times 10^{1}$ (RIU•s)$^{-1}$, $k_{d,X}$ = 8 (4) $\times 10^{-5}$ s^{-1}, and the equilibrium constant $K_{a,X} = k_{a,X}/k_{d,X}$ = 4(3)$\times 10^{5}$ RIU^{-1}. The data are listed in Table 5-25, and the fit curve is shown in Figure 5-31.

However, $k_{d,X}$ calculated from this method had a large error. In section 5.4.1, the strong binding site's desorption time constant was 6000(20) s, from which $k_{d,X}$ could be calculated as 1.7(1) $\times 10^{-4}$ s^{-1}. By using this more precise $k_{d,X}$, we calculated a more precise $K_{a,X}$. In this fit, $k_{a,X}$ = 3.17(8) $\times 10^{1}$ (RIU•s)$^{-1}$, $k_{d,X}$ = 1.7(1)$\times 10^{-4}$ s^{-1}, and $K_{a,X} = k_{a,X}/k_{d,X}$ = 1.9 (2)$\times 10^{5}$ RIU^{-1}.

Table 5-25 Hg(II) adsorption data sets for $k_{a,X}$, $k_{d,X}$, $K_{a,X}$, and $[X]_0$ calculation

Hg (II) Conc. (ppb)	*Hg (II) Conc. (RIU)*	$[MX]_{eq,a}$ *(RIU)*	$\tau_{a,X}$ **(s)**	$1/\tau_{a,X} = k_{a,X}$ •[M]+$k_{d,X}$	$[M]/[MX]_{eq,a}$
1000	1.050$\times 10^{-4}$	0.00204(1)	1160(20)	8.6(1)$\times 10^{-4}$	0.0514(3)
500	5.250$\times 10^{-5}$	0.00191(4)	2100(90)	4.7(2)$\times 10^{-4}$	0.0276(7)
300	3.150$\times 10^{-5}$	0.00191(8)	3600(200)	2.8 (2)$\times 10^{-4}$	0.0165(7)
200	2.100$\times 10^{-5}$	0.0018(2)	4900(700)	2.1(3)$\times 10^{-4}$	0.0116(1)
100	1.050$\times 10^{-5}$	0.0008(3)	50000(10000)	2.0(5)$\times 10^{-5}$	0.0012(3)
50	2.25$\times 10^{-6}$	0.0004(1)	4000(1000)	2(1)$\times 10^{-4}$	0.0140(5)

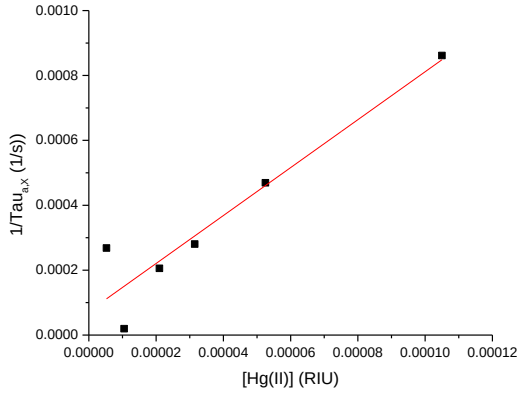

Figure 5-31 *By fitting $1/\tau_{a,X}$ vs. Hg(II) concentration, $k_{a,X}$, $k_{d,X}$, and $K_{a,X}$ for Hg(II) ion adsorption on the S_4-PMS coating can be calculated.*

Calculate $K_{a,X}$ and $[X]_0$ from Adsorption Curves

Again, in analogy to the interpretation of the Pb(II) data, the equilibrium constant *K* was determined using equation (5.10)

$$\frac{[M]}{[MX]_{eq,a}} = \frac{[M]}{[X]_0} + \frac{1}{K_{a,X}[X]_0} \tag{5.10}$$

By fitting $[Hg(II)]/[Hg(II)X]_{eq,a}$ vs. $[Hg(II)]$ with a linear function (Table 5-25, **Error! Reference source ot found.**), $K_{a,X}$ and $[X]_0$ could be calculated from the intercept and the slope.

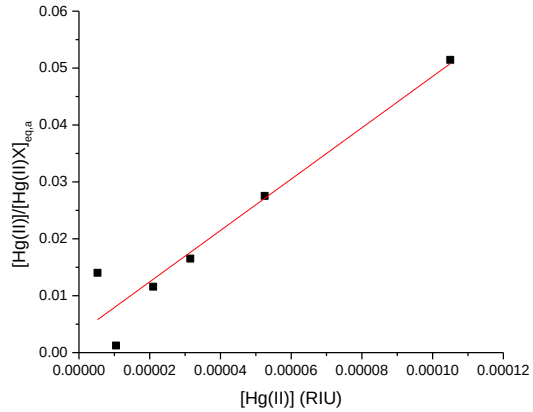

Figure 5-32 *By fitting $[Hg(II)]/[Hg(II)X]_{eq,a}$ vs. $[Hg(II)]$ with a linear function, $K_{a,X}$ and $[X]_0$ for Hg(II) ion adsorption on the S_4-PMS coating can be calculated.*

The equilibrium constant $K_{a,X}$ was calculated to be 1(1) $\times 10^5$ RIU^{-1}, which was close to but less precise than the $K_{a,X}$ in the first method (1.9 (2)$\times 10^5$ RIU^{-1}.) $\Delta_r G_m^\circ$(Hg(II)X) $= RT\ln K_{a,X}$ = 38(1)kJ/mol. The concentration of total binding sites was $[X]_0$ = 0.0022(3) RIU. Mole fraction of binding site X = 0.0022(3) RIU/(1.209RIU/mole fraction) = 0.0018(2) mol X binding site / mol film. This value was close to the X binding site surface concentration calculated from Pb(II) tests (0.00188(8) mol X binding site/mol film). Table 5-26 contains a summary of all the rate constants, equilibrium constants and adsorption capacities for Pb(II) and Hg(II) adsorption and desorption on the S4-PMS film.

The similarity between Figure 5-32 and Figure 5-31 is due to the fact that Equation (5.16) and equation (5.17) are equivalent. See section 5.1.6 for proof.

Table 5-26 Rate constants, equilibrium constants and adsorption capacities for Pb(II) and Hg(II) adsorption and desorption on the S_4-PMS film.

	Pb(II)	Hg(II)
k_a ($RIU^{-1}\bullet s^{-1}$)	5.0(1) $\times 10^1$	3.17(8) $\times 10^1$
k_d (s^{-1})	1.84(3)$\times 10^{-4}$	1.7(1)$\times 10^{-4}$
$K = k_a / k_d$ (RIU^{-1})	2.8 (1)$\times 10^5$	1.9 (2)$\times 10^5$
K(RIU^{-1}) Mothod 2	2.5 (9)$\times 10^5$	1(1) $\times 10^5$
G(kJ/mol)	42(2)	38(1)
$[X]_0$(RIU)	0.00147(6)	0.0022(3)
$[X]_0$(mole fraction)	0.00188(8)	0.0018(2)

Table 5-26 shows that the $\Delta_r G_m^\circ$(Hg(II)X) was smaller than $\Delta_r G_m^\circ$(Pb(II)X). Note that the pH for Hg(II) test was 5.3. Under this pH, the binding process was less favored than at neutral pH.

The equilibrium constant errors for Hg(II) was larger than that of Pb(II). One reason was that the short adsorption time (40 minutes vs. 3 hours) lead to large fit errors. A longer adsorption time and tests on more concentrations would lead to more accurate and precise equilibrium constants.

5.5 X-ray Photoelectron Spectroscopy (XPS) Measurement

5.5.1 XPS Measurement Conditions

To verify that the S_4-PMS indeed adsorbed Pb(II) ions, an X-ray Photoelectron Spectrum was recorded. Thin films were coated on silicon wafers using the method described in section 4.5. After post-treatment to remove all the surfactants, two pieces of Si wafer were immersed in 1 ppm $Pb(NO_3)_2$ solution and 1 ppm $Hg(NO_3)_2$ solution overnight, respectively. The two pieces of Si wafer were then dried in a desiccator for 12 hours before their XPS spectra were recorded under the conditions described below. Another piece of Si wafer with S_4-PMS but without heavy metal adsorption was also analyzed to obtain a control data set ("blank").

The XPS instrument was a Thermo Instruments Microlab 310F surface analysis system (Hastings, UK). The analysis was performed under ultrahigh vacuum conditions ($10^{-9} - 10^{-10}$ Torr) using a Mg Kα X-ray source (1253.6 eV) at an anode potential of 15 kV and an emission current of 20 mA. The fixed analyzer transmission (FAT) mode was used for scanning at a pass energy of 20 eV and a surface/detector take-off angle of 75°. The Shirley algorithm was used as the background subtraction method for all peaks. The Powell peak-fit algorithm was used with peak areas normalized between different elements using relative XPS sensitivity factors.[53]

5.5.2 XPS Measurement on S_4-PMS Film after Pb(II) Ion Absorption

As shown in the Pb and Hg XPS spectrum in Figure 5-33, two Pb peaks (left) and two Hg peaks (right) could be observed. The peak doublets represent the two spin-orbit states of the Pb 4f electron signal and two spin-orbit states of the Hg 3d electron signal, respectively.

The ratio of elements was calculated by peak fit, integration, and conversion by the Scofield sensitivity factor. As shown in Table 5-27, the ratio of Pb:S was roughly 1:2, and the ratio of Hg:S was roughly 2:1. The XPS data confirmed that the S_4-PMS film could adsorb Pb(II) and Hg(II). As the Pb(II) and Hg(II) could bind to both S_4 and silanol binding sites, it was hard to tell exactly how many metal ions

were bound to the tetra-sulfide groups. Nevertheless, the amount of metal in the film was much larger than expected even if all tetrasulfide sites were holding one metal ion. At this limit of complete saturation of all S_4-groups, an M:S ratio of 1:4 was expected. Instead, the metal loading in the film was higher by at least a factor of 2 for Pb(II) and a factor of 8 for Hg(II). This suggested that a large fraction of metals was either occupying other sites or that one S_4 site could hold several metal ions.

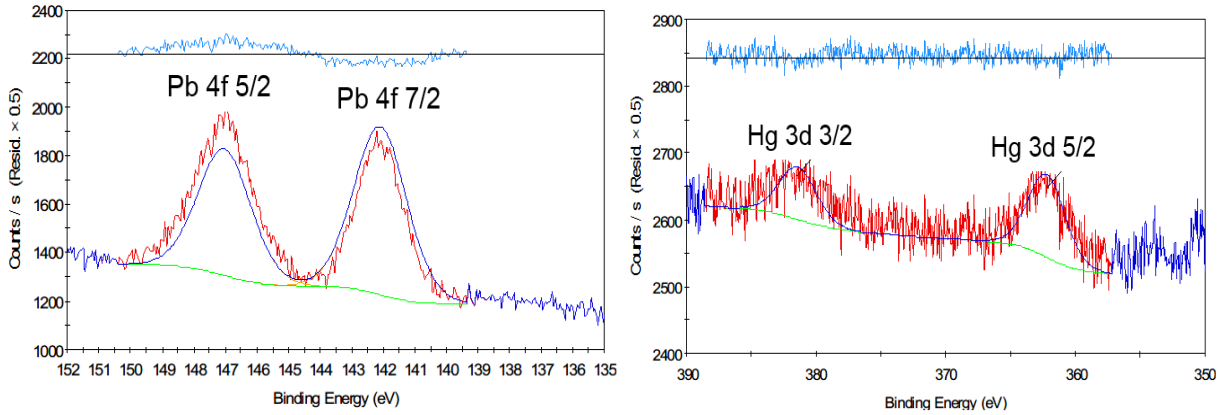

Figure 5-33 *XPS spectra of adsorbed heavy metals. (Left) XPS spectra of Pb(II) adsorbed in S_4-PMS coating. (Right) XPS spectra of Hg(II) adsorbed in S_4-PMS coating.*

Table 5-27 Element ratio calculated from XPS data

	Before adsorption	Pb(II) adsorption	Hg(II) adsorption
Si	21.5	21.45	19.95
O	55.87	52.47	47.54
C	21.66	24.45	28.44
S	0.97	1.14	1.25
Pb	---	0.50	
Hg	---		2.82

Chapter 6

Adsorption and Desorption of Other Metal Ions

This chapter discussed the response of the tetrasulfide mesoporous silica (S_4-PMS) functionalized SOI ring resonators and tetraethyl orthosilicate mesoporous silica (PMS) functionalized SOI ring resonators to several common ions. These ions include Na(I), K(I), Mg(II), Ca(II), Fe(II), Zn(II), Cd(II), Fe(III), and Al(III). The goal of these tests was to identify possible interferences of these ions on the desired detection of the heavy metal ions Pb(II), and Hg(II) discussed in the previous chapter. The results indicate that single, double, and triple charged metal ions have minor, medium, and large responses, respectively.

For all the tests described in this chapter, the data acquisition rate was one refractive index measurement per 30 s. The adsorption process and the subsequent DI water desorption process were both monitored for 3 hours. The experiment was completed by flushing the chip with 1 ppm aqueous Na_2EDTA solution for 1-3 hours to remove the remaining metal ions and restore the coating if necessary. For the discussion of the model and equations used to analyze the adsorption-desorption curves, see Chapter 3, section 3.2 and Chapter 5, section 5.1.

6.1 Na(I) Ion Adsorption and Desorption Tests

6.1.1 Na(I) Ion S_4-PMS Coating Tests

$NaNO_3$ was used to make 43.48 μmol/L (1 ppm) $NaNO_3$ DI water solution. The test results are shown in Figure 6-1, and the fit parameters are shown in Table 6-1. Single exponential functions gave good fits of the adsorption and desorption processes on the S_4-PMS coating, suggesting that the S_4-PMS coating had only one kind of binding site for Na(I).

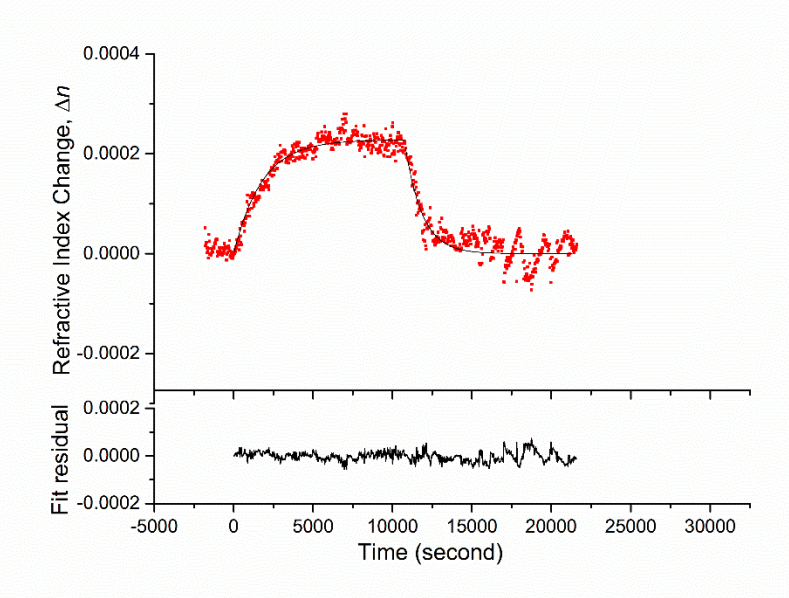

Figure 6-1 *Single exponential function fit of Na(I) ion adsorption and desorption processes on the S_4-PMS coating, with fit residual shown below. The fit was good, suggesting a single binding site model.*

Table 6-1 Fitting parameters for single exponential function fit on 43.48 μmol/L (1 ppm) $NaNO_3$ DI water adsorption and desorption processes on S_4-PMS coating.

	Adsorption (Single Fit)	**Water Desorption (Single Fit)**
q_e **or** q_0 ***(RIU)***	0.000228 (4)	0.00022(1)
τ_a **or** τ_d **(s)**	1780(60)	1070(40)

6.1.2 Na(I) Ion PMS Coating Tests

$NaNO_3$ was used to make 4.826 μmol/L $NaNO_3$ DI water solution. The test results are shown in Figure 6-2, and the fit parameters are shown in Table 6-2. Single exponential functions gave good fits of the adsorption and desorption processes on the PMS coating, suggesting the PMS coating had one kind of binding site for Na(I).

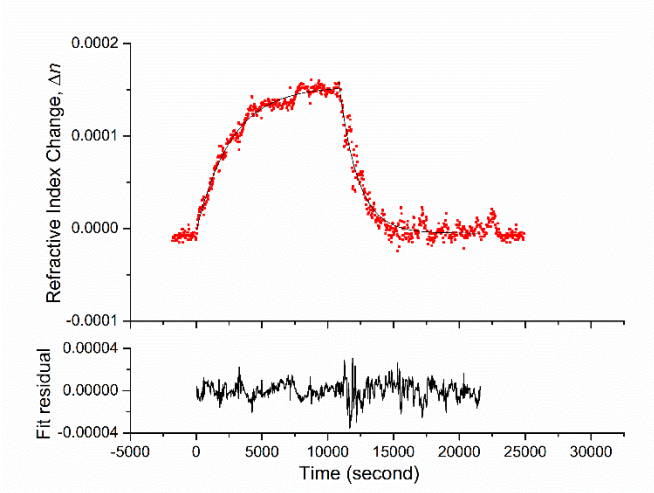

Figure 6-2 *Single exponential function fit of Na(I) ion adsorption and desorption processes on the TOESMPS coating, with fit residual shown below. The fit was good suggesting a single binding site model.*

Table 6-2 Fitting parameters for single exponential function fit on 4.826 μmol/L $NaNO_3$ DI water adsorption and desorption processes on PMS coating

	Adsorption (Single Fit)	**Water Desorption (Single Fit)**
q_e **or** q_0 ***(RIU)***	0.000157 (1)	0.000168(3)
τ_a **or** τ_d **(s)**	2690(60)	1430(40)

The capacity of the second film was slightly less – not surprising given its differing composition. Note that the small response in this test may be misleading. The Na(I) ion had a small polarizability, and the mole fraction in the film may, in fact, be very high. In both films, the adsorption rate constant was slightly greater than the desorption rate constant and comparable to that of the loosely bound heavy metal ions.

6.2 K(I) Ion Adsorption and Desorption Tests

6.2.1 K(I) Ion S_4-PMS Coating Tests

KNO_3 was used to make 25.58 μmol/L (1 ppm) KNO_3 DI water solution. The test results are shown in Figure 6-3, and the fit parameters are shown in Table 6-3. Single exponential functions gave good fits

of the adsorption and desorption processes on the S_4-PMS coating, suggesting again that the S_4-PMS coating had only one kind of binding site for K(I).

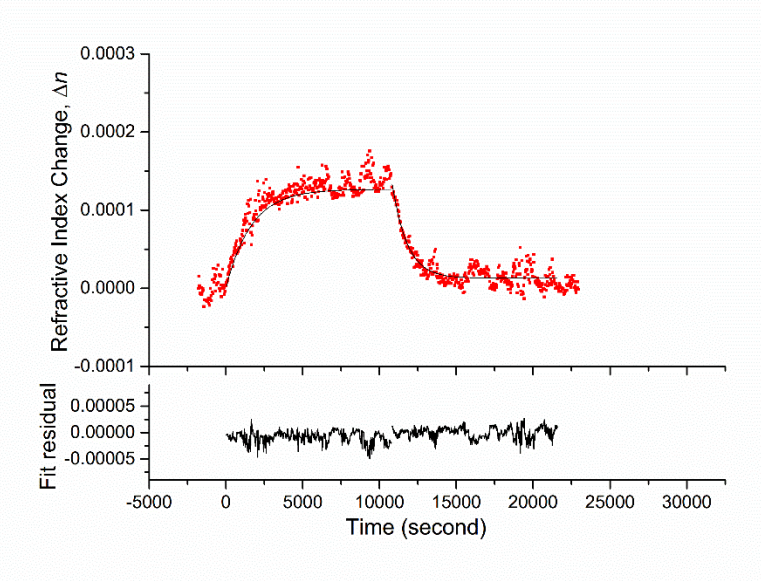

Figure 6-3 *Single exponential function fit of K(I) ion adsorption and desorption processes on the S_4-PMS coating, with fit residual shown below. The fit was good suggesting a single binding site model.*

Table 6-3 Fitting parameters for single exponential function fit on 25.58 μmol/L (1 ppm) KNO_3 DI water adsorption and desorption processes on S_4-PMS coating.

	Adsorption (Single Fit)	**Water Desorption (Single Fit)**
q_e **or** q_0 ***(RIU)***	0.000127 (3)	0.000124(4)
τ_a **or** τ_d **(s)**	1640(70)	970(50)

6.2.2 K(I) Ion PMS Coating Tests

KNO_3 was used to make 4.826 μmol/L KNO_3 DI water solution. The test results are shown in Figure 6-4, and the fit parameters are shown in Table 6-4. Single exponential functions gave good fits of the adsorption and desorption processes on the PMS coating, suggesting that the PMS coating had only one kind of binding site for K(I).

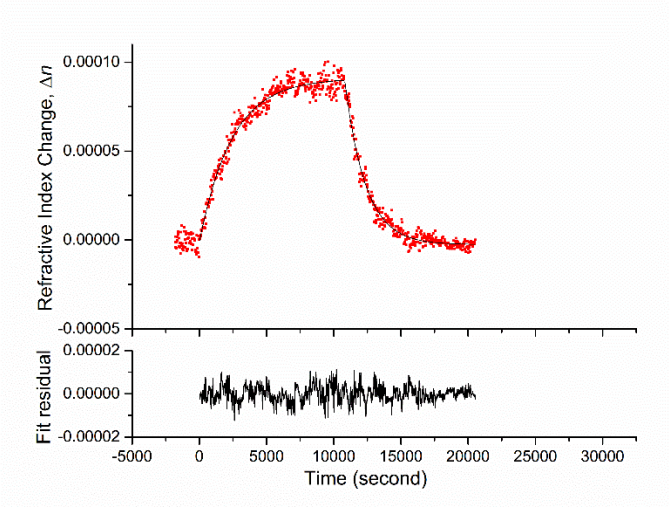

Figure 6-4 *Single exponential function fit of K(I) ion adsorption and desorption processes on the TOESMPS coating, with fit residual shown below. The fit was good suggesting a single binding site model.*

Table 6-4 Fitting parameters for single exponential function fit on 4.826 μmol/L KNO_3 DI water adsorption and desorption processes on PMS coating

	Adsorption (Single Fit)	**Water Desorption (Single Fit)**
q_e **or** q_0 ***(RIU)***	0.000092 (9)	0.00009(1)
τ_a **or** τ_d **(s)**	2430(70)	1540(30)

The response curves and time constants were similar to those obtained for sodium ions, and the same conclusions apply.

6.3 Mg(II) Ion Adsorption and Desorption Tests

$Mg(NO_3)_2$ was used to make 41.15 μmol/L (1ppm) $Mg(NO_3)_2$ DI water solution. The test results are shown in Figure 6-5, and the fit parameters are shown in Table 6-5. Single exponential functions gave good fits of the adsorption and desorption processes on the S_4-PMS coating, suggesting that the S_4-PMS coating had one kind of binding site for Mg(II).

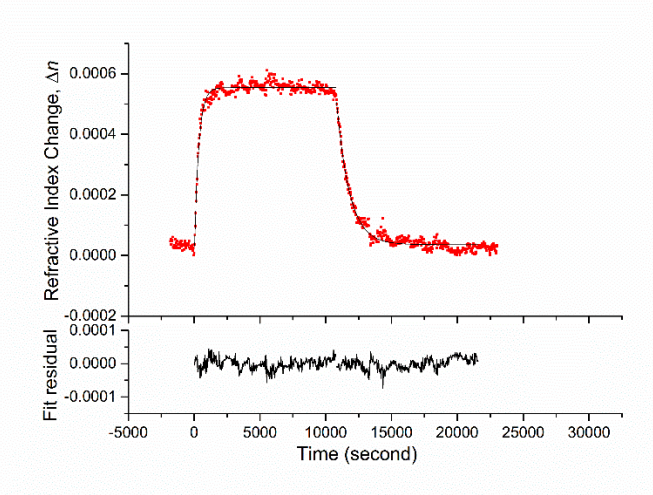

Figure 6-5 *Single exponential function fit of Mg(II) ion adsorption and desorption processes on the S_4-PMS coating, with fit residual shown below. The fit was good suggesting a single binding site model.*

Table 6-5 Fitting parameters for single exponential function fit on 41.15 µmol/L (1ppm) $Mg(NO_3)_2$ DI water adsorption and desorption processes on S_4-PMS coating.

	Adsorption (Single Fit)	**Water Desorption (Single Fit)**
q_e **or** q_0 ***(RIU)***	0.000572 (9)	0.000484(5)
τ_a **or** τ_d **(s)**	330(8)	970(20)

The adsorption and desorption processes were remarkably fast when Mg(II) was used as a metal ion. While only a single site was responsible for binding the ion, it did appear that the affinity was quite strong.

6.4 Ca(II) Ion Adsorption and Desorption Tests

6.4.1 Ca(II) Ion S_4-PMS Coating Tests

$Ca(NO_3)_2$ was used to make 25.00 µmol/L (1ppm) $Ca(NO_3)_2$ DI water solution. The test results are shown in Figure 6-6, and the fit parameters are shown in Table 6-6. Single exponential functions gave good

fits of the adsorption and desorption processes on the S_4-PMS coating, suggesting that the S_4-PMS coating had one kind of binding site for Ca(II)

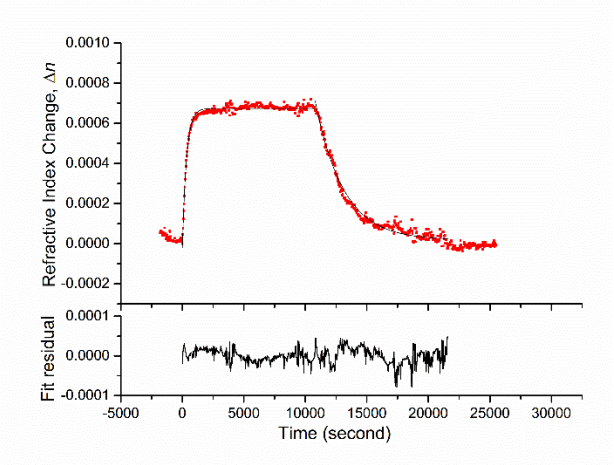

Figure 6-6 *Single exponential function fit of Ca(II) ion adsorption and desorption processes on the S_4-PMS coating, with fit residual shown below. The fit was good suggesting a single binding site model.*

Table 6-6 Fitting parameters for single exponential function fit on 25.00 μmol/L (1ppm)$Ca(NO_3)_2$ DI water adsorption and desorption processes on S_4-PMS coating.

	Adsorption (Single Fit)	**Water Desorption (Single Fit)**
q_e **or** q_0 ***(RIU)***	0.000693(8)	0.000692(7)
τ_a **or** τ_d **(s)**	339(6)	2290(20)

Compared to Mg(II) the Ca(II) desorption process was much slower while the adsorption rate was almost identical. Ca(II) appeared to be more strongly bound to the single type of binding site.

6.4.2 Ca(II) Ion PMS Coating Tests

$Ca(NO_3)_2$ was used to make 4.826 μmol/L $Ca(NO_3)_2$ DI water solution. The test results are shown in Figure 6-7, and the fit parameters are shown in Table 6-7. Single exponential functions gave good fits of the adsorption and desorption processes on the PMS coating, suggesting that the PMS coating had one kind of binding site for Ca(II).

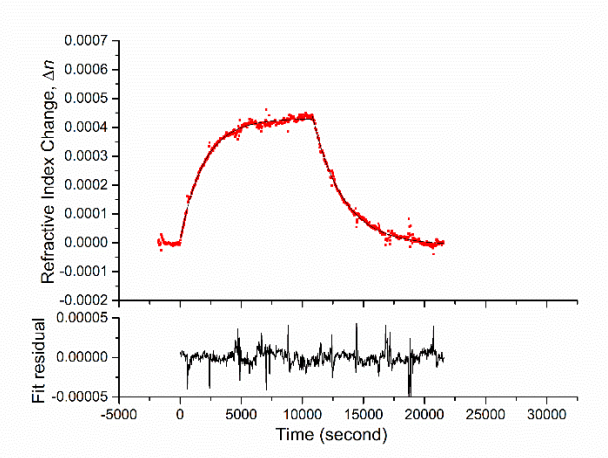

Figure 6-7 *Single exponential function fit of Ca(II) ion adsorption and desorption processes on the PMS coating, with fit residual shown below. The fit was good suggesting a single binding site model.*

Table 6-7 Fitting parameters for single exponential function fit on 4.826 μmol/L $Ca(NO_3)_2$ DI water adsorption and desorption processes on PMS coating

	Adsorption (Single Fit)	**Water Desorption (Single Fit)**
q_e **or** q_0 ***(RIU)***	0.000422 (2)	0.000452(3)
τ_a **or** τ_d **(s)**	1930(20)	2490(30)

The Ca(II) ion adsorbed only quite slowly into the film without a tetrasulfide binding site and was readily removed using water with a rate that was comparable to that of the tetrasulfide containing film. Note that the Ca(II) solution in the PMS tests had lower Ca(II) concentration (4.826 μmol/L) than that in S_4-PMS test (25.00 μmol/L, 1 ppm). As a result, the S_4-PMS test had a higher adsorption rate, which largely due to the higher concentration. As it had been demonstrated in chapter 5, high concentration ion solution had higher adsorption rates and a smaller τs.

6.5 Fe(II) Ion Adsorption and Desorption Tests

6.5.1 Fe(II) Ion S_4-PMS Coating Tests

$Fe(NO_3)_2$ was used to make 17.86 μmol/L (1 ppm) $Fe(NO_3)_2$ DI water solution. The comparison between single and double exponential functions fits of Fe(II) ion adsorption-desorption curve are shown in Figure 6-8, and the fit parameters are shown in Table 6-8. Single exponential functions gave a poor fit to the adsorption-desorption curve while double exponential functions gave a much better fit, suggesting that the S_4-PMS coating had two kinds of binding sites for Fe(II).

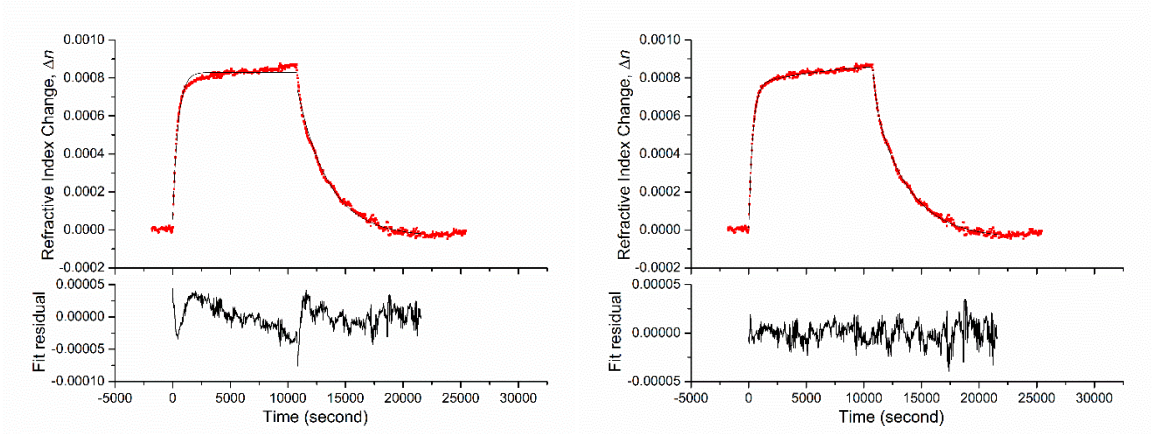

Figure 6-8 *Comparison between single and double exponential functions fits of Fe(II) ion adsorption and desorption on the S_4-PMS coating. (Left) Single exponential functions fit with fit residual shown below. (Right) Double exponential functions with fit residual shown below.*

Table 6-8 Fitting parameters for single and double exponential functions fits of 17.86 μmol/L (1 ppm) Fe(II) ion adsorption and desorption on the S_4-PMS coating.

Single site model			Two site model		
	Adsorption	**Desorption**		**Adsorption**	**Desorption**
q_e **or** q_0 ***(RIU)***	0.00079(1)	0.000842(3)	$q_{e,X}$ **or** $q_{0,X}$ ***(RIU)***	0.000764(5)	0.00071(3)
τ **(s)**	758(10)	1910(10)	τ_X **or** τ_X **(s)**	616(8)	2210(60)
---	---	---	$q_{e,Y}$ **or** $q_{0,Y}$ ***(RIU)***	0.000195(7)	0.00018(3)
---	---	---	τ_Y **or** τ_Y **(s)**	19400(100)	620(90)

The fitting parameters indicated that the majority of the Fe (II) ions bind strongly and quickly to one of the binding sites. A smaller fraction was rather loosely bound and readily removed.

6.5.2 Fe(II) Ion PMS Coating Tests

$Fe(NO_3)_2$ was used to make 4.826 μmol/L $Fe(NO_3)_2$ DI water solution. The test results are shown in Figure 6-9, and the fit parameters are shown in Table 6-9. Single exponential functions gave good fits of the adsorption and desorption processes on the PMS coating, suggesting that the PMS coating had one kind of binding site for Fe(II).

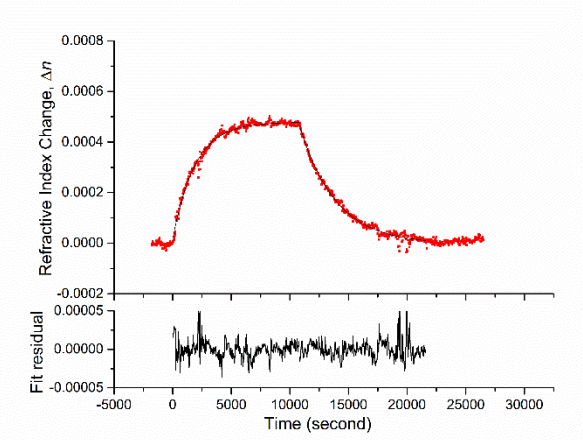

Figure 6-9 *Single exponential function fit of Fe(II) ion adsorption and desorption processes on the TOESMPS coating, with fit residual shown below. The fit was good, suggesting a single binding site model.*

Table 6-9 Fitting parameters for single exponential function fit on 4.826 μmol/L $Fe(NO_3)_2$ DI water adsorption and desorption processes on PMS coating

	Adsorption (Single Fit)	**Water Desorption (Single Fit)**
q_e **or** q_0 ***(RIU)***	0.000464 (3)	0.000472(2)
τ_a **or** τ_d **(s)**	1890(20)	3090(30)

The TEOS-based film showed a Fe(II) adsorption rate that fell between the two rates for the tetrasulfide-containing film, whereas the desorption rate was slower than either one of them. It appears

therefore that more binding sites for Fe(II) were available in this film and that they form a quite strong binding.

6.6 Zn(II) Ion Adsorption and Desorption Tests

$Zn(NO_3)_2$ was used to make 15.29 μmol/L (1ppm) $Zn(NO_3)_2$ DI water solution. The comparison between single and double exponential functions fits of Zn (II) ion adsorption-desorption curves were shown in Figure 6-10, and the fit parameters are shown in Table 6-10. Single exponential functions gave poor fits of the adsorption and desorption processes while double exponential functions gave good fits, suggesting that the S_4-PMS coating had two kinds of binding site for Zn (II).

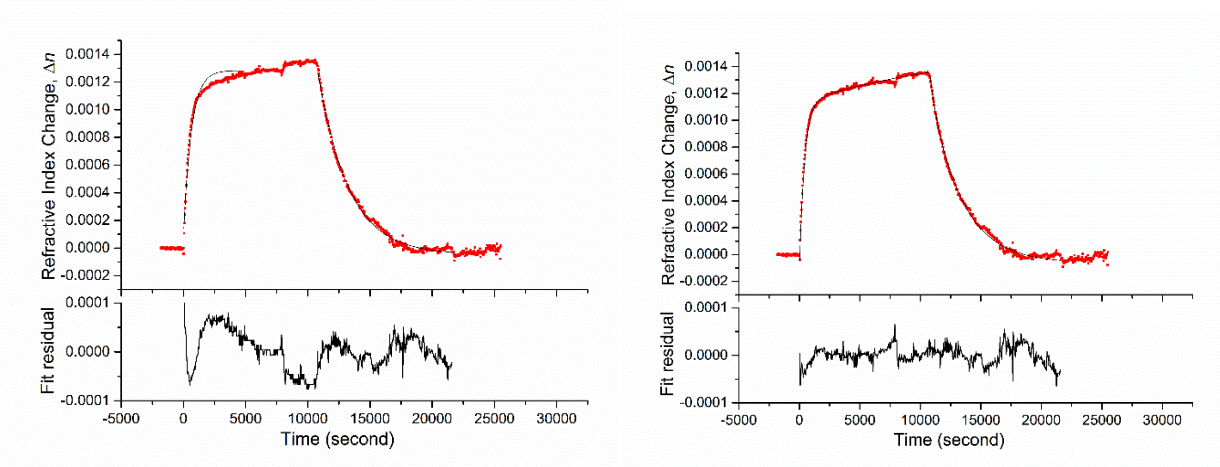

Figure 6-10 *Comparison between single and double exponential functions fits of Zn(II) ion adsorption and desorption on the S_4-PMS coating. (Left) Single exponential functions fit with fit residual shown below. The fit was poor. (Right) Double exponential functions fit with fit residual shown below. This fit was much better than the single exponential functions fit, suggesting a double binding site model.*

Table 6-10 Fitting parameters for single and double exponential functions fits of 15.29 μmol/L (1ppm) Zn(II) ion adsorption and desorption on the S_4-PMS coating.

Single site model			Two site model		
	Adsorption	**Desorption**		**Adsorption**	**Desorption**
q_e **or** q_0 ***(RIU)***	0.00120 (2)	0.001330(5)	$q_{e,X}$ **or** $q_{0,X}$ ***(RIU)***	0.001168(7)	0.00129 (2)
τ **(s)**	640(20)	2460(20)	τ_X **or** τ_X **(s)**	421(5)	2620(50)
---	---	---	$q_{e,Y}$ **or** $q_{0,Y}$ ***(RIU)***	0.000445(5)	0.00012(2)
---	---	---	τ_Y **or** τ_Y **(s)**	15000(3000)	420(40)

The pattern for Zn(II) was almost identical to that for Fe(II). The parameters showed that the majority of the Zn(II) ions bound strongly and quickly to one of the binding sites and a smaller fraction was rather loosely bound and readily removed.

6.7 Cd(II) Ion Adsorption and Desorption Tests

$Cd(NO_3)_2$ was used to make 8.900 μmol/L (1ppm) $Cd(NO_3)_2$ DI water solution. The comparison between single exponential functions, and double exponential functions fits of Cd(II) ion adsorption-desorption curves were shown in Figure 6-11, and the fit parameters are shown in Table 6-11. Single exponential functions gave poor fits of the adsorption and desorption processes while double exponential functions gave good fits, suggesting S_4-PMS coating had two kinds of binding site for Cd(II). Notice that the Na_2EDTA desorption process took only 90 to 120 seconds (3 to 4 data points) to complete. The lack of data points on the desorption curve led to a better single exponential function fit.

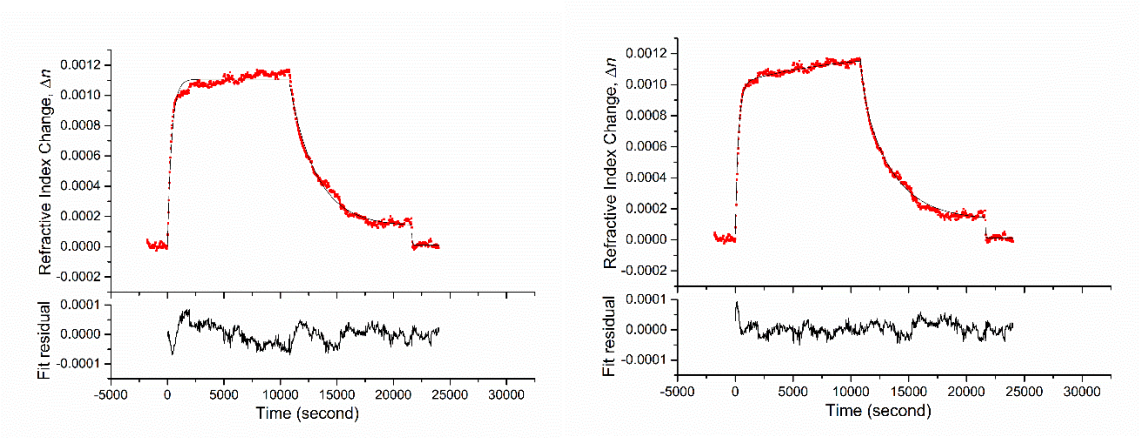

Figure 6-11 *Comparison between single and double exponential functions fits of Cd(II) ion adsorption and desorption on the S_4-PMS coating. (Left) Single exponential functions fit with fit residual shown below. The fit was poor. (Right) Double exponential functions fit with fit residual shown below. This fit was much better than the single exponential functions fit, suggesting a double binding site model.*

Table 6-11 Fitting parameters for single and double exponential functions fits of 8.900 μmol/L (1ppm) Cd(II) ion adsorption and desorption on the S_4-PMS coating.

Single site model				Two site model			
	Adsorption	**Desorption**	**Na_2EDTA rinse**		**Adsorption**	**Desorption**	**Na_2EDTA rinse**
q_e **or** q_0 ***(RIU)***	0.001105(2)	0.000941(6)	0.00019(2)	$q_{e,X}$ **or** $q_{0,X}$ ***(RIU)***	0.00097(1)	0.00086(1)	0.00019(2)
τ **(s)**	376(10)	2380(30)	34(6)	τ_X **or** τ_X **(s)**	267(5)	2730(70)	34(6)
---	---	---	---	$q_{e,Y}$ **or** $q_{0,Y}$ ***(RIU)***	0.00021 (2)	0.00019(2)	---
---	---	---	---	τ_Y **or** τ_Y **(s)**	37000(2000)	330(60)	---

As for Zn(II) and Fe(II) in previous sections, we also found that Cd(II) showed binding to two distinct sites. One had such a high affinity to Cd(II) that EDTA was required to remove the metal ion. The rates were comparable to those observed for the two lighter ions, though.

6.8 Fe(III) Ion Adsorption and Desorption Tests

6.8.1 Fe(III) Ion S_4-PMS Coating Tests

$Fe(NO_3)_3$ was used to make 17.90 μmol/L (1ppm) $Fe(NO_3)_3$ DI water solution. The comparison between single and double exponential functions fits of Fe(III) ion adsorption-desorption curve are shown in Figure 6-12, and the fit parameters are shown in Table 6-12. Double exponential functions gave much better fits of the adsorption and Na_2EDTA desorption processes than those using single exponential functions. However, for the DI water desorption process, the large error in double exponential fitting parameters suggest that a single-exponential fit should be used. These results suggest that S_4-PMS coating has two kinds of binding site for Fe(III). Only the ions binding to one kind of binding site, however, can be removed by DI water at a slow rate ($\tau 1$ =50000 s). Ions bound to the other binding site can only be removed by Na_2EDTA solution.

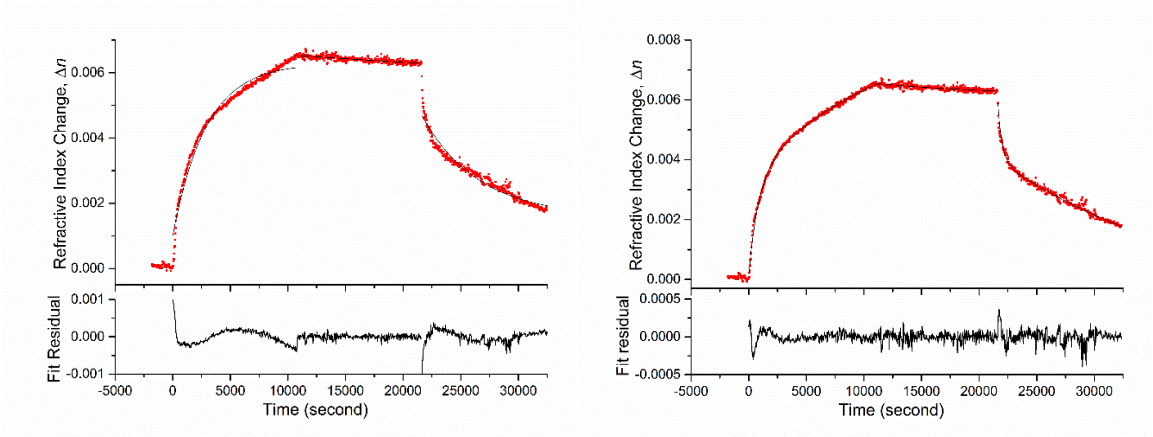

Figure 6-12 *Comparison between single and double exponential functions fits of Fe(III) ion adsorption and desorption on the S_4-PMS coating. (Left) Single exponential functions fit, with fit residual shown below. The fit was poor. (Right) Double exponential functions fit, with fit residual shown below. This fit was much better than the single exponential functions fit, suggesting a double binding site model.*

Table 6-12 Fitting parameters for single and double exponential functions fits of 17.90 μmol/L (1ppm) Fe(III) ion adsorption and desorption on the S_4-PMS coating.

Single site model				Two site model			
	Adsorption	**Desorption**	**Na_2EDTA rinse**		**Adsorption**	**Desorption**	**Na_2EDTA rinse**
q_e **or** q_0 ***(RIU)***	0.00528 (4)	0.001(2)	0.00312(5)	$q_{e,X}$ **or** $q_{0,X}$ ***(RIU)***	0.003164(6)	---	0.0048(1)
τ **(s)**	2910(6)	50000(9000)	4900(200)	τ_X **or** τ_X **(s)**	830(30)	---	17000(400)
---	---	---	---	$q_{e,Y}$ **or** $q_{0,Y}$ ***(RIU)***	0.0051(2)	0.001(2)	0.00204 (7)
---	---	---	---	τ_Y **or** τ_Y **(s)**	11200(900)	50000(9000)	350(10)

The single exponential adsorption model gave a poor fit to the data so that it was almost certain that two binding sites compete. The fast uptake process had a rate comparable to that of Pb(II), Hg(II) and other heavy metal ions, but was entirely non-reversible in water (the fits to a bi-exponential model did not converge). The slower of the two processes was reversible but only very slowly. It was interesting that the desorption process using the EDTA chelating agent also shows clearly a bi-exponential behaviour. The faster of the two processes presumably removed Fe(III) from the relatively weak binding sites, whereas the slow process removed the tightly bound Fe(III). By comparison, the removal of divalent ions using EDTA was much faster with $\tau < 200$ s, with the possible exception of Hg(II) and Pb(II), although even in those cases the slow component contained in the EDTA removal process was not very pronounced.

6.8.2 Fe(III) Ion PMS Coating Tests

$Fe(NO_3)_3$ was used to make 4.826 μmol/L $Fe(NO_3)_2$ DI water solution. The test results are shown in Figure 6-13, and the fit parameters are shown in Table 6-13. Single exponential functions gave good fits of the adsorption and desorption processes on the PMS coating, suggesting PMS coating have one kind of binding site for Fe(III).

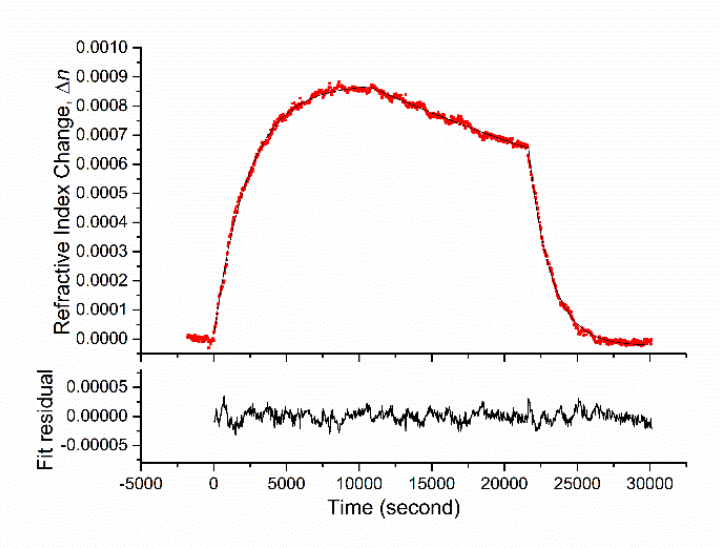

Figure 6-13 *Single exponential function fit of Fe(II) ion adsorption and desorption processes on the TOESMPS coating, with fit residual shown below. The fit was good suggesting a single binding site model.*

Table 6-13 Fitting parameters for single exponential function fit on 4.826 μmol/L $Fe(NO_3)_3$ DI water adsorption and desorption processes on PMS coating

	Adsorption	**Desorption**	**Na_2EDTA rinse**
q_e* or *q_0* *(RIU)	0.000871 (2)	0.000877(2)	0.000680(1)
***τ* (s)**	2340(60)	39500(800)	1540(10)

The adsorption time of 2340 s fell between the two times observed for the S_4-PMS model, while the desorption processes on Fe(III) in the PMS film was slow but observable with a time constant similar to the desorption from the less active binding site in S_4-PMS. This suggested the affinity of the silica film to Fe(III) is surprisingly high.

6.9 Al(III) Ion Adsorption and Desorption Tests

$Al(NO_3)_3$ was used to make 37.04 μmol/L (1ppm) $Al(NO_3)_3$ DI water solution. The comparison between single and double exponential functions fits of Al(III) ion adsorption-desorption curve are shown

in Figure 6-14, and the fit parameters are shown in Table 6-14. Similar to the case of Fe(III) adsorption and desorption, double exponential functions gave much better fits of the adsorption and Na_2EDTA desorption processes than that of single exponential functions. However, for the DI water desorption process, the large error in the double exponential fitting parameters suggests that a single exponential fit may be more appropriate. These results suggest that S_4-PMS coating had two kinds of binding sites for Al(III). Only the ions bind to one kind of binding site, however, could be removed by DI water at a slow rate (τ_1 =23000 s). The remaining ions, as well as those bound to the other binding site, could only be removed by Na_2EDTA solution.

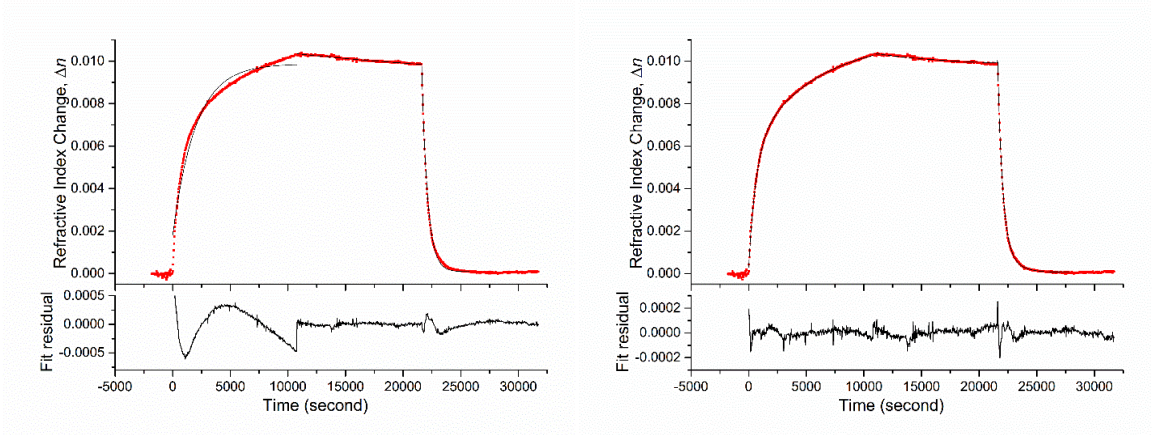

Figure 6-14 *Comparison between single and double exponential functions fits of Al(III) ion adsorption and desorption on the S_4-PMS coating. (Left) Single exponential functions fit, with fit residual shown below. The fit was poor. (Right) Double exponential functions fit, with fit residual shown below. This fit was much better than the single exponential functions fit, suggesting a double binding site model.*

Table 6-14 Fitting parameters for single and double exponential functions fits of 37.04 μmol/L (1ppm) Al(III) ion adsorption and desorption on the S_4-PMS coating.

Single site model				Two site model			
	Adsorption	**Desorption**	**Na_2EDTA rinse**		**Adsorption**	**Desorption**	**Na_2EDTA rinse**
q_e **or** q_0 ***(RIU)***	0.0080 (8)	0.0013(2)	0.00980(3)	$q_{e,X}$ **or** $q_{0,X}$ ***(RIU)***	0.00554 (3)	---	0.0014(2)
τ **(s)**	1990(40)	22847(3980)	512(2)	τ_X **or** τ_X **(s)**	631(5)	---	1220(80)
---	---	---	---	$q_{e,Y}$ **or** $q_{0,Y}$ ***(RIU)***	0.00519(2)	0.0013(2)	0.0087(2)
---	---	---	---	τ_Y **or** τ_Y **(s)**	5640(90)	22847(3980)	430(6)

Al(III) shows a similar behaviour to Fe(III). It was found that the fast uptake process was not reversible but that the slow adsorption could be reversed, albeit very gradually. The rinsing process with EDTA was also biexponential and likely indicative of removal from two distinct binding sites.

6.10 Summary

As shown in Table 6-15, the test results suggest that the PMS coatings had only one type of binding site, likely the deprotonated silanol groups, which bound all the cations in our tests to a different extent. By comparison, the S_4-PMS coating had an additional binding site in the form of the tetra-sulfide group, which does not bind Na(I), K(I), Mg(II), Ca(II), Fe(II), and Zn(II), but does bind to Cd(II), Pb(II), Hg(II), Fe(III), and Al(III). The trend was reflected approximately by the solubility of the corresponding metal sulfides. Consider that sulfides of the alkali and alkaline earth metals have some water solubility whereas sulfides of the Cu and Zn families (including CuS, AgS AuS, ZnS, CdS, and HgS) are among the least soluble compounds known. Similarly, PbS has such a low solubility that it is one of the least toxic forms of lead. Both FeS and Fe_2S_3 are considered insoluble in water whereas Al_2S_3 decomposes in water.

Table 6-15 Different ion binding patterns with PMS coating and S_4-PMS coating.[54]

	PMS			S_4-PMS					
	Adsorption	DI water Desorption	Na_2EDTA Desorption	Adsorption	DI water Desorption	Na_2EDTA Desorption	Binding to silanol	Binding to sulfur	K_{sp} of metal sulfide
Na(I)	Single	Single	n/a	Single	Single	n/a	Weak	No	(reacts)
K(I)	Single	Single	n/a	Single	Single	n/a	Weak	No	(reacts)
Mg(II)				Single	Single	n/a		No	(reacts)
Ca(II)	Single	Single	n/a	Single	Single	n/a		No	(reacts)
Fe(II)	Single	Single	n/a	double	double	n/a		Weak	6×10^{-19}
Zn(II)				double	double	n/a		Weak	2×10^{-25}
Cd(II)				double	double	double		Medium	8.0×10^{-27}
Pb(II)	Single	Single	Single	double	double	double		Medium	3×10^{-29}
Hg(II)				double	double	double		Strong	1.6×10^{-53}
Fe(III)	Single	Single	Single	double	Single	double	Strong	Strong	unstable
Al(III)				double	Single	double	Strong	Strong	unknown

Table 6-16 Cation and oxide polarizability for some ions [44, 47]

Data from Dimitrov and Sakka (1995) [44]			**Data from Mon et. al. (1979) [47]**	
Oxide	**Cation polarizability (Å3)**	**Oxide polarizability (Å3)**	**Cation**	**Cation polarizability (Å3)**
CuO	0.437	2.838	Cu	1.7
MgO	0.094	1.699	Na	0.2
CaO	0.469	2.505	K	0.9
ZnO	0.283	2.612	Zn	0.8
CdO	0.1054	2.909	Cd	1.8
Al_2O_3	0.054	1.365	Al	0.053
PbO	3.623	3.450		
Fe_2O_3	0.437	2.647		

Figure 6-15 and Table 6-17 show the maximum refractive index change ($q_{e,1} + q_{e,2}$) for each of the 1-ppm metal ion solutions, the maximum refractive index changes for each ion per μmol/L, as well as the initial refractive index change rates during adsorption process for each 1 ppm ion solution, and the initial refractive index change rates during adsorption process for each ion per μmol/L.

The maximum refractive index change for each ion depends on the mole of ions bound to the coating and the polarizability of the ions. The relationship between polarizability and refractive index follows the Lorentz–Lorenz equation. Table 6-16 listed some of the ions' cation polarizability and oxide polarizability from two publications. The values in the table suggest large increases on polarizability from cation to oxide for the all the metal ions, with the exception of Pb(II), which drops slightly. Some of the values from the two publications didn't agree on the same elements. At least, these values gave us a rough idea of the ion polarizability.

The high maximum refractive index change for Fe(III) and Al(III) is probably due to their high affinity, as their polarizability are not particularly high. For Na(I) and K(I), the small maximum refractive index changes and the low initial adsorption rates could be explained by their low affinity to the coating and low polarizability.

For Mg(II), Ca(II), Fe(II), and Zn(II), the maximum refractive index change and initial adsorption rate increased with the atomic weight and the number of electrons.

For Fe(II), and Zn(II), Cd(II), Pb(II), and Hg(II), which bound to the tetra-sulfide binding site, their affinity was consistent with the K_{sp} value of the corresponding metal sulfides. The Hg(II) initial adsorption rates cannot be directly compared with that of the other ions, as the Hg(II) adsorption process was tested at a pH = 5.3 (instead of a neutral pH). At the low pH, some of the binding sites were protonated, and the binding process was expected to be slower. At the same pH level, the initial adsorption rate for Hg(II) would probably be higher than that of Pb(II).

Fe(III) and Al(III) ions showed a strong affinity with both silanol groups and the tetra-sulfide group, probably due to high charge-charge interaction.

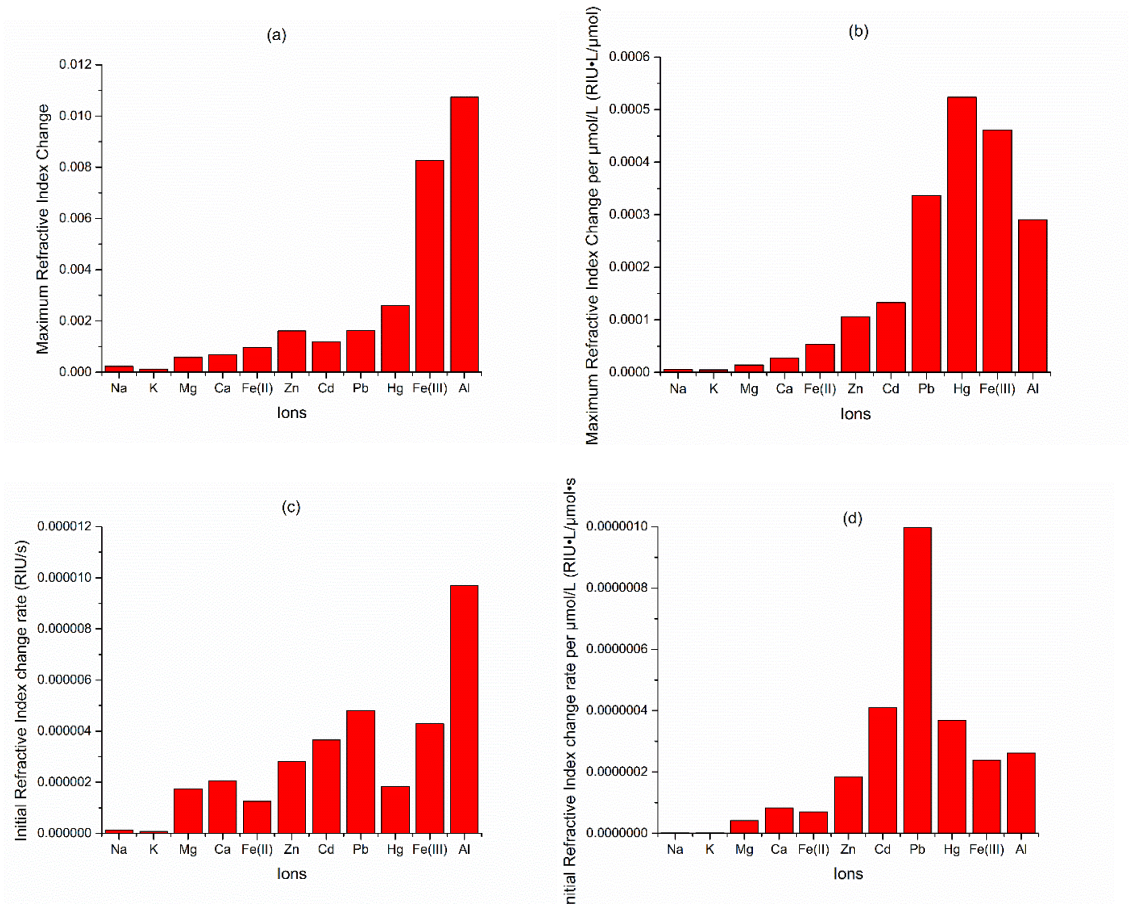

Figure 6-15 *Column graphs comparison between different ion adsorption on S_4-PMS film. (a) Maximum refractive index changes for each ion. (b) Maximum refractive index changes for each ion per µmol/L. (c) Initial refractive index change rates during adsorption process for each ion (d) Initial refractive index change rates during adsorption process for each ion per µmol/L*

Table 6-17 Data sets for column graphs comparison between different ion adsorption on S_4-PMS film(above).

	$q_{e,X}$ (RIU)	$\tau_{a,X}$ (s)	$q_{e,Y}$ (RIU)	$\tau_{a,Y}$ (s)	$q_{e,X} + q_{e,Y}$ (RIU)	Initial Refractive Change Rate (RIU/s)	$(q_{e,X} + q_{e,Y})$ /Conc. (RIU•L/μmol)	Initial Refractive Change Rate /Conc. (RIU•L/μmol•s)
Na(I)	0.000228	1775	---	---	0.000228	1.28×10^{-7}	0.000005	2.96×10^{-9}
K(I)	0.000127	1644	---	---	0.000127	7.71×10^{-8}	0.000005	3.01×10^{-9}
Mg(II)	0.000572	330	---	---	0.000572	1.73×10^{-6}	0.000014	4.21×10^{-8}
Ca(II)	0.000693	339	---	---	0.000693	2.05×10^{-6}	0.000028	8.21×10^{-8}
Fe(II)	0.000764	616	0.000195	19422	0.000959	1.25×10^{-6}	0.000054	6.99×10^{-8}
Zn(II)	0.001169	421	0.000445	14867	0.001614	2.81×10^{-6}	0.000106	1.84×10^{-7}
Cd(II)	0.000967	267	0.000214	9176	0.001181	3.65×10^{-6}	0.000133	4.10×10^{-7}
Pb(II)	0.001434	301	0.000189	4652	0.001624	4.81×10^{-6}	0.000336	9.96×10^{-7}
Hg(II)	0.001595	958	0.001016	5960	0.002610	1.84×10^{-6}	0.000524	3.68×10^{-7}
Fe(III)	0.003164	826	0.005099	11163	0.008263	4.29×10^{-6}	0.000461	2.39×10^{-7}
Al(III)	0.005542	631	0.005193	5637	0.010735	9.71×10^{-6}	0.000290	2.62×10^{-7}

In Figure 6-16 and Table 6-18, we showed the maximum refractive index change (q_e) and initial refractive index change for six metal ions (Na(I), K(I), Ca(II), Fe(II), Pb(II), and Fe(III)) solutions. All solutions had the same concentration of 4.826 mmol/L. Like the data from the S_4-PMS film, the light, singly charged ions gave only tiny shifts, while doubly and triply charged ions gave large and quick shifts. The difference was probably due to high affinity to the silanol groups, for their polarizabilities were not particularly high.

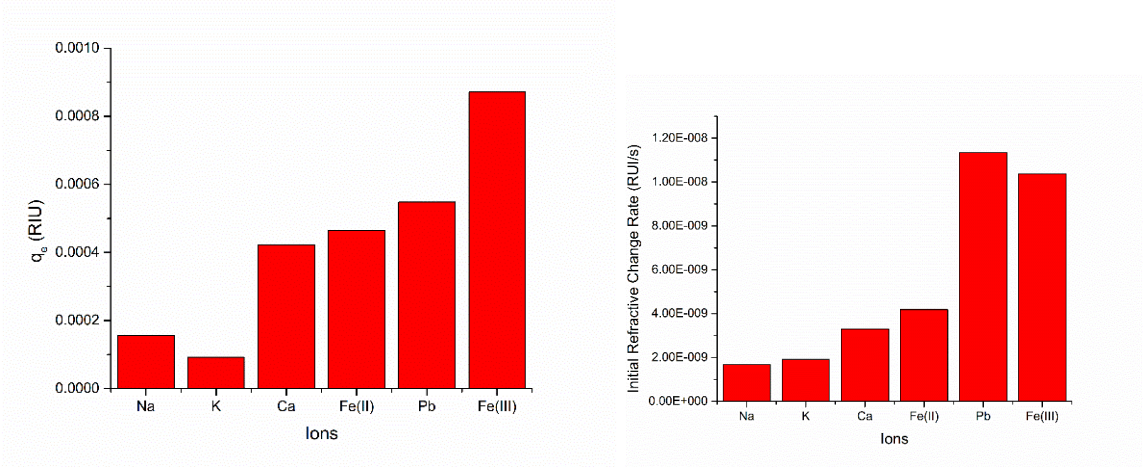

Figure 6-16 *Column graphs comparison between different ion adsorptions on PMS film. (Left) the asymptotic refractive index change, q_e, in the adsorption processes. (Right), the initial refractive index change in the adsorption processes.*

Table 6-18 Data sets for column graphs comparison between different ion adsorption on PMS film(Figure 6-16).

Metal ions	q_e (RIU)	τ_a (s)	Initial Refractive Change Rate (RIU/s)
Na(I)	0.000157 (1)	2690(60)	$5.8(2)\times10^{-8}$
K(I)	0.000092 (9)	2430(70)	$3.8(2)\times10^{-8}$
Ca(II)	0.000422 (2)	1930(20)	$2.19(3)\times10^{-7}$
Fe(II)	0.000464 (3)	1890(20)	$4.18(4)\times10^{-7}$
Pb(II)	0.000548(3)	687(6)	$7.8(1)\times10^{-7}$
Fe(III)	0.000871 (2)	2340(60)	$3.7(1)\times10^{-7}$

Chapter 7

Conclusion

This chapter includes a summary of the results on the chemical sensing platform, as well as a proposal for the future work.

7.1 Summary

Previously there has been an extensive study on a bis[3-(triethoxysilyl)propyl]tetrasulfide (BTESPTS) functionalized mesoporous silica (MPS) film, which has been shown to have an affinity for heavy metal ions, such as Pb(II). [34] The aim of this research was to develop a prototype heavy metal sensor based on SOI tandem ring resonators coated with S_4-PMS film. I characterized the sensor's response to Pb(II) ions and Hg(II) ions, as well as several ions that are frequently present as interferences. XPS data also confirmed that the S_4-PMS film could adsorb Pb(II) and Hg(II).

To fully remove the metal ion from the film, 1 ppm Na_2EDTA solution (pH = 7 for most ions, pH = 5 for strongly bound ions like Hg(II), Fe(III), and Al(III)) was used to remove all the metal ions from the film. Strong acid solution (0.1 M HNO_3) also worked, but it eroded the film substantially. All MPS films in this research were removable from the coated SOI chips by immersing the chips in 0.1 M NaOH solution for an hour without destroying the delicate waveguides on the chips. While the MPS films would dissolve in basic solution, and to a lesser extent in strong acids, the films were stable in DI water and can endure hundreds of adsorption and desorption tests. However, the film degraded faster in tap water and much faster in seawater. The erosion rate in tap water and sea water were 5 times and 91 times faster than that in DI water. ($-6.62(1)\times10^{-8}$ RIU/s in tap water, $-1.359(7)\times10^{-8}$ RIU/s in DI water, and $-1.233(4)\times10^{-6}$RIU/s in seawater) The mechanism for these erosion processes is currently not well understood.

In this work, a functionalized ring resonator system was developed as the measurement platform, a scanning laser diode was used to continuously interrogate the sensor head, and a microfluidics device was developed as the liquid sample delivery system to make sure the liquid sample flow was steady and air

bubble free. Solution samples of Pb(II) and Hg(II), as well as other common ions in ground water, including Na(I), K(I), Mg(II), Ca(II), Fe(II), Zn(II), Cd(II), Fe(III), and Al(III), were flowed over the coating ring resonator so that the metal ions adsorbed into the film, changed the film refractive indices, and shifted the ring resonator resonance peaks to higher wavelength. Data analysis procedures and protocol based on Igor Pro™ were developed to extract the peak shifting information. The adsorption and desorption curves were recorded and analyzed. Similar curves were recorded on PMS coated ring resonator as control data sets.

These research results suggest that the tetraethyl orthosilicate mesoporous silica (PMS) films had one binding site to bind with all the metal ions tested, presumably the deprotonated silanol groups. The strength of the binding was closely related to the ions' charge states, showing weak binding effects to single charged ions, like Na(I) and K(I), and strong binding effects to triply charged ions, like Fe(III) and Al(III). Other doubly charged ions fell in between. By comparison, the tetrasulfide-functionalized mesoporous silica (S_4-PMS) films, which were made by co-condensation between BTESPTS and TEOS, had an additional binding site that did not bind Na(I), K(I), Mg(II), Ca(II), Fe(II), and Zn(II), but preferentially bound to Cd(II), Pb(II), Hg(II), Fe(III), and Al(III). The trend was reflected approximately by the solubility of the corresponding metal sulfides. As a result, the selectivity of the S_4-PMS film was limited to those heavy metal ions and other metal ions that form insoluble sulfides. The distinction between those ions, e.g. Pb(II), Hg(II), Cd(II), but also Fe(III) and Al(III), is currently not possible unless the water sample is pretreated to remove all ions that interfere.

In addition to heavy metal sensing, this platform can be used to study ion or molecule adsorption, desorption, and diffusion processes on thin films, as long as the processes cause coating refractive index changes.

7.2 Future work

The sensing platform has been proven to be a useful and robust testing platform. The platform can be improved on several aspects, including coating optimization, data processing method, optical design, testing parameter optimization, etc.

7.2.1 Coating Optimization

The S_4-PMS coating used in this research lacked selectivity for a single species. Its sensitivity for Pb(II) and Hg(II) was not as low as is required to quantify the heavy metal concentration in drinking water by the Canadian drinking water standard, 10 ppb and 1 ppb, respectively. [55]. The coating can be optimized by increasing the ratio of BTESPTS to TEOS precursors, or by increasing the surface area, i.e. its porosity. Also, trimethylethoxysilane (TMES) can be used to cap silanol groups and make the tetrasulfide groups the only interaction sites with metal ions. Of course, the coating can contain other more selective functionalization groups to bind with heavy metal ions, such as crown thioethers, DNA, RNA, or proteins.

7.2.2 Data Processing Method

The data analysis method can be improved by moving from off-line analysis to online data analysis. Better data gathering and analysis system would show the coating refractive index in real time. In this way, researchers can see the refractive index change while the sample is flowing. A lot of time can be saved if researchers can know whether the adsorption or desorption process is complete, or whether the chip is properly cleaned before performing the test.

7.2.3 Optical Design

The current light coupling method is the “edge-on coupling” method. In this method, it is not only hard to align the fibre delivering the laser light with the silicon waveguide in the first place, but the method is also subject to vibration and alignment stage drifting, which means that the stages need to be adjusted manually every 5 - 20 minutes. During the alignment process, the light polarization has to be re-optimized to get the best ring resonator spectra. The platform would be easier to work with if the fibres were fused with the waveguide end on the edge of the chip. This would remove the alignment, vibration, and polarization issue. Ideally, the SOI chip can be packaged into a probe, like the commercial probe shown in Figure 7-1.

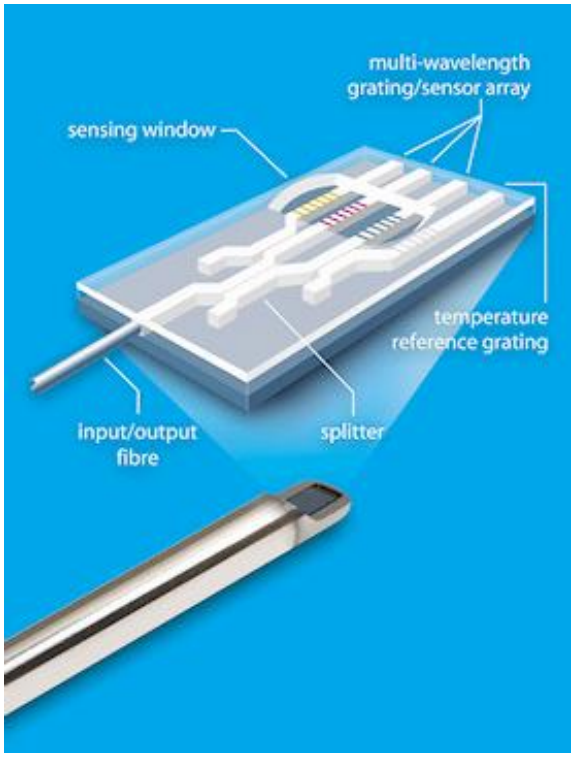

Figure 7-1 *An example of Stratophase micro optical sensor packaging. From [56]*

The current set up can only couple light in and out of one waveguide and probe one pair of tandem ring resonators at a time, although the chip has dozens of other ring resonators. If two or more tandem resonator systems - coated with different coatings - were interrogated simultaneously, this could further differentiate between analytes and increase the selectivity of the sensor. This design requires that either all tandem resonators are on the same bus waveguide and light is directed into a single photodetector, or that each tandem ring resonator is coupled to a different waveguide, and the transmitted light is detected by a multitude of photodetectors.

Currently, the lower limit of the scanning wavelength range is determined by the fact that the range must contain as least one sensing peak and one reference peak, with some "peak-free" region in between. A future design may employ shorter scan ranges that are separate for the sensing and reference peaks, i.e. the time spent scanning across the "peak-free" region of the spectrum could be reduced, and the sampling rate may be increased.

7.2.4 Testing Parameter Optimization

A systematic optimization study using different flow rates, different data acquisition rates, different testing times, and different Na_2EDTA concentrations would allow us determination of the best testing environment to save reagents and testing time.

References

1. Chen, W., *Chemical detection and sensing using optical interferometry*, in *The Department of Chemistry*. 2013, Queen's University: Master's Thesis.
2. Eftimov, T., *Applications of Fiber Gratings in Chemical and Biochemical Sensing*, in *Optical Guided-wave Chemical and Biosensors II*, M. Zourob and A. Lakhtakia, Editors. 2010, Springer Berlin Heidelberg: Berlin, Heidelberg. p. 151-176.
3. Spirin, V., et al., *Fiber Bragg grating sensor for petroleum hydrocarbon leak detection.* Optics and Lasers in Engineering, 1999. **32**(5): p. 497-503.
4. Cong, J., et al., *Fiber optic Bragg grating sensor based on hydrogels for measuring salinity.* Sensors and Actuators B: Chemical, 2002. **87**(3): p. 487-490.
5. Yeo, T., et al., *Characterisation of a polymer-coated fibre Bragg grating sensor for relative humidity sensing.* Sensors and Actuators B: Chemical, 2005. **110**(1): p. 148-156.
6. Sutapun, B., M. Tabib-Azar, and A. Kazemi, *Pd-coated elastooptic fiber optic Bragg grating sensors for multiplexed hydrogen sensing.* Sensors and Actuators B: Chemical, 1999. **60**(1): p. 27-34.
7. Chen, X., et al., *Optical chemsensor based on etched tilted Bragg grating structures in multimode fiber.* IEEE photonics technology letters, 2005. **17**(4): p. 864-866.
8. Miao, Y., et al., *Relative humidity sensor based on tilted fiber Bragg grating with polyvinyl alcohol coating.* IEEE Photonics technology letters, 2009. **21**(7): p. 441-443.
9. Lépinay, S., A. Ianoul, and J. Albert, *Molecular imprinted polymer-coated optical fiber sensor for the identification of low molecular weight molecules.* Talanta, 2014. **128**: p. 401-407.
10. Albert, J., L.Y. Shao, and C. Caucheteur, *Tilted fiber Bragg grating sensors.* Laser & Photonics Reviews, 2013. **7**(1): p. 83-108.
11. DeLisa, M.P., et al., *Evanescent wave long-period fiber Bragg grating as an immobilized antibody biosensor.* Analytical chemistry, 2000. **72**(13): p. 2895-2900.
12. Falciai, R., A. Mignani, and A. Vannini, *Long period gratings as solution concentration sensors.* Sensors and Actuators B: Chemical, 2001. **74**(1): p. 74-77.
13. Zhang, J., et al., *Zeolite thin film-coated long period fiber grating sensor for measuring trace organic vapors.* Sensors and Actuators B: Chemical, 2009. **135**(2): p. 420-425.
14. Tripathi, S.M., et al., *Long period grating based biosensor for the detection of Escherichia coli bacteria.* Biosensors and Bioelectronics, 2012. **35**(1): p. 308-312.
15. Du, J., et al., *Periodic Mesoporous Organosilica Films: Key Components of Fiber‐Optic‐Based Heavy‐Metal Sensors.* Small, 2010. **6**(11): p. 1168-1172.
16. Janz, S., et al., *Silicon Microphotonic Waveguide Technology for Sensing, Spectroscopy and Communications.* ECS Transactions, 2006. **3**(11): p. 61-78.
17. Saunders, J., *Refractometry Studies of the Optical Properties of Polymer Films and the Development of Polymer Coated Refractive Index Sensors*, in *The Department of Chemistry*. 2016, Queen's University: Doctoral Thesis.
18. Zhu, H., J.D. Suter, and X. Fan, *Label-free optical ring resonator bio/chemical sensors*, in *Optical Guided-wave Chemical and Biosensors II*. 2010, Springer. p. 259-279.
19. Mackey, G., *Synthesis, Modification, and Application of Siloxane Materials for Environmental Sensing*, in *The Department of Chemistry*. 2016, Queen's University: Doctoral Thesis.
20. Research International, I. *RAPTOR: Portable, Multianalyte Bioassay Detection System*. 2017; Available from: http://www.resrchintl.com/RAPTOR_Bioassay_System.html.
21. Mbio. *MBio Array System*. 2017; Available from: http://mbiodx.com/products/.
22. Sensors, C. *Creoptix WAVEchips*. 2017; Available from: http://www.creoptix.com/products/sensors.
23. Ostendum. *Ostendum antibody optical sensors*. 2017; Available from: http://www.ostendum.com/index.html.

24. Genalyte. *Multiplex Photonic Ring Immunoassay*. 2017; Available from: http://www.genalyte.com/resources/.
25. Sciences, G.L. *Biacore SPR systems*. 2017; Available from: https://proteins.gelifesciences.com/knowledge-library/surface-plasmon-resonance/surface-plasmon-resonance/.
26. Ozalp, V.C., et al., *Pathogen detection in complex samples by quartz crystal microbalance sensor coupled to aptamer functionalized core–shell type magnetic separation.* Analytica chimica acta, 2015. **853**: p. 533-540.
27. Wei, Q., et al., *Detection and spatial mapping of mercury contamination in water samples using a smart-phone.* ACS nano, 2014. **8**(2): p. 1121-1129.
28. Li, X., et al., *A simple highly sensitive and selective aptamer-based colorimetric sensor for environmental toxins microcystin-LR in water samples.* Journal of hazardous materials, 2016. **304**: p. 474-480.
29. Tawil, N., et al., *Bacteriophages: biosensing tools for multi-drug resistant pathogens.* Analyst, 2014. **139**(6): p. 1224-1236.
30. Vikesland, P.J. and K.R. Wigginton, *Nanomaterial enabled biosensors for pathogen monitoring-a review.* Environmental science & technology, 2010. **44**(10): p. 3656-3669.
31. Irshad, M., et al., *Molecularly imprinted nanomaterials for sensor applications.* Nanomaterials, 2013. **3**(4): p. 615-637.
32. Du Ziwei, L.X. and Z. Xiaodong, *Preparation of TNT Molecularly Imprinted Polymer Microspheres via Precipitation Polymerization [J]*. Chemistry, 2009. **11**: p. 017.
33. Haupt, K., et al., *Molecularly imprinted polymers*, in *Molecular imprinting*. 2011, Springer. p. 1-28.
34. Du, J., *Synthesis and Applications of Nanostructured Mesoporous Organosilica Films and Monoliths*, in *The Department of Chemistry*. 2011, Queen's University: Doctoral Thesis.
35. Yeh, J.M., et al., *Organic‐acid‐catalyzed sol‐gel route for preparing poly (methyl methacrylate)‐silica hybrid materials.* Journal of applied polymer science, 2008. **110**(4): p. 2108-2114.
36. Soler-Illia, G.J.d.A., et al., *Chemical strategies to design textured materials: from microporous and mesoporous oxides to nanonetworks and hierarchical structures.* Chemical reviews, 2002. **102**(11): p. 4093-4138.
37. Hoffmann, F., et al., *Silica‐based mesoporous organic‐inorganic hybrid materials.* Angewandte Chemie International Edition, 2006. **45**(20): p. 3216-3251.
38. Dioum, A. and S. Hamoudi, *Mono-and quaternary-ammonium functionalized mesoporous silica materials for nitrate adsorptive removal from water and wastewaters.* Journal of Porous Materials, 2014. **21**(5): p. 685-690.
39. Jutidamrongphan, W., et al., *High removal of phosphate from wastewater using silica sulfate.* Environmental chemistry letters, 2012. **10**(1): p. 21-28.
40. Hanumegowda, N.M., I.M. White, and X. Fan, *Aqueous mercuric ion detection with microsphere optical ring resonator sensors.* Sensors and Actuators B: Chemical, 2006. **120**(1): p. 207-212.
41. Atkins, P. and J. De Paula, *Physical Chemistry - Eighth Edition*. Oxford University Press, Oxford. 2006. 1053.
42. Gupta, G., G. Prasad, and V. Singh, *Removal of chrome dye from aqueous solutions by mixed adsorbents: fly ash and coal.* Water Research, 1990. **24**(1): p. 45-50.
43. Saunders, J.E., et al., *Quantitative diffusion and swelling kinetic measurements using large-angle interferometric refractometry.* Soft matter, 2015. **11**(45): p. 8746-8757.
44. Dimitrov, V. and S. Sakka, *Electronic oxide polarizability and optical basicity of simple oxides. I.* Journal of Applied Physics, 1996. **79**(3): p. 1736-1740.

45. Thierfelder, C., et al., *Relativistic and electron correlation effects in static dipole polarizabilities for the group-14 elements from carbon to element Z= 114: Theory and experiment.* Physical Review A, 2008. **78**(5): p. 052506.
46. Hanni, M., et al., *Polarizabilities of Pb^{2+} and Pb^{4+} and ionization energies of Pb^{+} and Pb^{3+} from spectroscopy of high-L Rydberg states of Pb^{+} and Pb^{3+}*. Physical Review A, 2010. **81**(4): p. 042512.
47. Mon, K., N. Ashcroft, and G. Chester, *Core polarization and the structure of simple metals.* Physical Review B, 1979. **19**(10): p. 5103.
48. Washburn, E.W. and C.J. West, *International critical tables of numerical data, physics, chemistry and technology*. Vol. 4. 1928: National Academies.
49. Xu, D.-X., et al., *Real-time cancellation of temperature induced resonance shifts in SOI wire waveguide ring resonator label-free biosensor arrays.* Optics express, 2010. **18**(22): p. 22867-22879.
50. Schmitt, K. and C. Hoffmann, *High-refractive-index waveguide platforms for chemical and biosensing*, in *Optical Guided-wave Chemical and Biosensors I*. 2010, Springer. p. 21-54.
51. Loock, H.-P. and P.D. Wentzell, *Detection limits of chemical sensors: Applications and misapplications.* Sensors and Actuators B: Chemical, 2012. **173**: p. 157-163.
52. Plant, K.K.S.W.T., *2015 Annual Report On Drinking Water Quality*. 2015.
53. Arjumand, R., *Proline-Based Chiral Stationary Phases: Insights Into The Mechanism Of Chiral Selectivity*, in *The Department of Chemistry*. 2016, Queen's University: Doctoral Thesis.
54. Metals, S.L. *Solubility Products of Selected Compounds*. 2017; Available from: http://www.saltlakemetals.com/SolubilityProducts.htm.
55. Canada, H., *Guidelines for Canadian Drinking Water Quality Summary Table*. 2008, Government of Canada Ottawa.
56. Campbell, B. *Stratophase micro optical sensor*. 2017; Available from: http://www.sensorsmag.com/sensors-mag/sensor-technology-automates-feeding-control-single-use-13329.